

**ELECTRODEPOSITION AND
CHARACTERISATION OF NICKEL-NIOBIUM-BASED
DIFFUSION BARRIER METALLISATIONS FOR HIGH
TEMPERATURE ELECTRONICS INTERCONNECTIONS**

By
Jing Wang

A DOCTORAL THESIS
SUBMITTED IN PARTIAL FULFILMENT OF THE REQUIREMENTS
FOR THE AWARD OF
DOCTOR OF PHILOSOPHY OF LOUGHBOROUGH UNIVERSITY

September 2015

© Jing Wang (2015)

ABSTRACT

The control of interfacial microstructural stability is of utmost importance to the reliability of liquid solder interconnects in high temperature electronic assemblies. This is primarily due to excessive intermetallic compounds (IMCs) that can form and continuously grow during high temperature operation, which practically renders conventional barrier metallisations inadequate. In this study, electrically conducting, NbO_x containing Ni coatings were developed using electrodeposition. Their suitability as a solder diffusion barrier layer was assessed in terms of the electrical conductivity and barrier property.

The present work explores a novel electrochemical route to produce Ni- NbO_x composite coatings of good uniformity, compactness and purity, from non-aqueous glycol-based electrolytes consisting of NiCl_2 and NbCl_5 as metal precursors. The effects of cathodic current density and NaBH_4 concentrations on the surface morphology, composition and thickness of the coatings were examined. A combined study of Scanning Transmission Electron Microscopy (STEM) and Electrochemical Quartz Crystal Microbalance (EQCM) was conducted to understand the fundamental aspects of this novel electrodeposition process. The composite coatings generally exhibited good electrical conductivity. The reaction behaviour between a liquid 52In-48Sn solder and Ni- NbO_x , with Nb contents up to 6 at.%, were studied at 200°C. The results indicate that, Ni- NbO_x with sufficient layer thickness and higher Nb content, offered longer service lifetime. Nb enrichment was generally observed at or close to the reaction front after high temperature storage, which suggests evident effectiveness of the enhanced diffusion barrier characteristics.

Keywords: Electrodeposition, liquid solders, In-Sn, diffusion barrier metallisations, Ni- NbO_x , composites, deep eutectic solvents, Type IV Deep Eutectic Solvents, STEM, XPS, EQCM, GCIB.

Dedicated to Roger

ACKNOWLEDGEMENTS

Firstly, I would like to thank my supervisors, Geoffrey D. Wilcox, Roger J. Mortimer, Changqing Liu and Mark A. Ashworth, for their continuous support and illuminating guidance during the last four years. It is a great credit to Geoff and Mark, that they have created a lab environment where good science can flourish without having to compromise the work-life balance. The level of trust they have put in the competence of people who work for them is inspiring and uplifting. Special thanks go to Roger for being such a wonderful mentor and friend, as well as to Changqing for introducing me to electronics manufacture.

Secondly, I would like to thank my colleagues, Han Jiang and Chris Stuttle, for their advice and discussion on the project. I am indebted to Zhaoxia Zhou, Keith Yendall and Scott Doak for their assistance and discussion on materials characterisations. Thanks also go to Leicester Ionic Liquid Group for their technical help and hospitality during my visit to University of Leicester.

I am grateful to my family for their great love and deep understanding. Last but not the least, I must thank my wife, Yingzi, for the last four years. It has been a rollercoaster ride, but remarkably rewarding and enjoyable. I could not think of a better companion. Thank you for all the sacrifices you made to take such good care of me during this time.

Table of Contents

Abstract	I
Acknowledgements	IV
Table of Contents.....	V
List of Figures	IX
List of Tables	XVII
Glossary of Abbreviations	XVIII
Context of Research	XX
Chapter 1 High Temperature Electronics Packaging	1
1.1 Introduction to Electronics Packaging	1
1.2 Electronics Packaging Hierarchy	2
1.3 Introduction to High Temperature Electronics Packaging	3
1.3.1 Implications of High Temperatures at Semiconductor Device Level	4
1.3.2 Implications of High Temperatures for First-level Packaging	5
1.3.2.1 Wire Bonds	5
1.3.2.2 Die Attach	7
1.3.2.3 Plastic Encapsulants	8
1.3.2.4 Leads and Lead frames	10
1.3.3 Implications of High Temperatures for Second-level Packaging	10
1.3.3.1 Electrically Conductive Adhesives	11
1.3.3.2 High Temperature Solders	12
1.4 Summary	13
1.5 References	15
Chapter 2 Liquid Solder Interconnections & Diffusion Barrier Metallisations...17	
2.1 Introduction	17
2.2 Liquid Solder Interconnections	18
2.3 Interfacial Reactions between Liquid Solders and Metallisations	20
2.3.1 Liquid In-Sn with Cu	21
2.3.2 Liquid In-Sn with Pure Ni	22
2.3.3 Liquid In-Sn with Ni-based Variants	24
2.3.4 Liquid In-Sn with Pure Nb	26
2.4 Summary	28
2.5 References	29
Chapter 3 Niobium Electrodeposition	31

3.1 Introduction to Niobium Metal and Oxides	31
3.2 General Principles of Electrodeposition	33
3.2.1 Cathodic Current Efficiency	36
3.2.2 Cathodic Overpotential	37
3.3 Electrodeposition Electrolytes	38
3.3.1 Aqueous electrolytes	39
3.3.2 High Temperature Molten Salts	40
3.3.3 Ionic Liquids	41
3.3.3.1 Introduction	41
3.3.3.2 Classifications	42
3.3.3.3 Potential windows	43
3.3.3.4 Nb electrodeposition in ionic liquids	45
3.4 Induced Co-deposition	48
3.5 Summary	49
3.6 References	49
Chapter 4 Experimental Techniques	53
4.1 Electrochemical Analysis and Electrodeposition	53
4.1.1 Electrodeposition cell and Electrode Pretreatment	53
4.1.2 Electrolytes	54
4.1.3 Electrical Conductivity Assessment of Electrolytes	55
4.1.4 pH Measurements	56
4.1.5 Cyclic Voltammetry.....	56
4.1.6 Electrodeposition	57
4.1.7 Quartz Crystal Microbalance	57
4.2 Soldering and Thermal Transients	59
4.3 Electron Microscopy	59
4.3.1 Scanning Electron Microscopy	60
4.3.1.1 Sample preparation	60
4.3.1.2 Instrumentation	60
4.3.2 Transmission Electron Microscopy	60
4.3.2.1 Sample preparation	60
4.3.2.2 Instrumentation	62
4.4 X-ray Photoelectron Spectroscopy	62
4.5 Electrical Conductivity Attainment of Thin Film Specimens	63
4.6 Solderability Measurements of Thin film Specimens	64
4.7 References	65
Chapter 5 Nb Electrochemistry in Type III and Type IV Eutectic Solvents and Derivatives	66
5.1 Introduction of Niobium Metal Precursors	66
5.1.1 Niobium (V) Chloride	67

5.1.2 Anodic Dissolution of Niobium Metal	67
5.2 Electrochemical Behaviour of Type III Deep Eutectic Solvents Dissolved with NbCl ₅	69
5.3 Electrochemical Behaviour of Type III Deep Eutectic Solvents Containing Anodically Dissolved Niobium Metal	76
5.4 Electrochemical Behaviour of Type IV Deep Eutectic Solvents Containing Dissolved NbCl ₅	77
5.5 New Paradigm for Electroplating Cell Design	79
5.5.1 Instability of Platinised Titanium Anode & Its Replacement	79
5.5.2 Instability of Silver Wire Reference Electrode & Its Replacement	81
5.6 Ni-Nb Co-deposition	82
5.7 Summary	85
5.8 References	85
Chapter 6 Electrodeposition of Ni-Nb from Type IV Eutectic Solvent Derivatives	87
6.1 Effect of Major Electrolyte Constituent	87
6.1.1 Ethylene Glycol-based Solutions	88
6.1.2 Propylene Glycol-based Solutions	92
6.2 Threshold Deposit Thickness	97
6.3 Effect of Metal Ion Concentrations in Solutions	101
6.4 Effect of Sodium Borohydride	104
6.5 Summary	109
6.6 References	110
Chapter 7 Characterisations of Ni-NbO _x Composite Electrodeposits	112
7.1 Microstructural Characterisations of Ni-NbO _x Electrodeposits	112
7.2 Spectroscopic Characterisations of Ni-NbO _x Electrodeposits	118
7.2.1 Depth Profiling Using Argon Monomer Ion Beam	118
7.2.2 Depth Profiling Using Argon Gas Cluster Ion Beam	124
7.3 Microbalance Study of Ni-Nb Electrodeposition	130
7.4 Mechanism for Ni-Nb Electrodeposition	132
7.5 Summary	134
7.6 References	135
Chapter 8 Diffusion Barrier Characterisations of Ni-NbO _x For Liquid In-Sn Solders	137
8.1 Electrical Conductivity Measurements of Ni-NbO _x Electrodeposits	137
8.2 Solderability Assessment	138
8.3 Liquid Solder Diffusion Test	140
8.4 STEM Characterisations of Reacted, In-Sn/Ni-NbO _x Diffusion Couples	150

8.5 Summary	158
8.6 References	159
 Chapter 9 Conclusions	 160
9.1 Conclusions	160
9.2 Recommendations for Future Work	163
 Appendix I – List of Publications	 165

List of Figures

Figure 1.1 A schematic diagram illustrating the electronics packaging hierarchy comprising of at least four packaging levels [1.4]	3
Figure 1.2 A schematic diagram illustrating the cross section of a representative, first level, integrated circuit package	6
Figure 2.1 A schematic diagram illustrating an electronics assembly configuration utilising liquid solder interconnections [2.1]	19
Figure 2.2 SEM images showing the representative morphology of IMCs at eutectic In-Sn(l)/Cu(s) interface after soldering reactions at various temperatures for 120 min: a) 200°C and b) 300°C [2.7]	22
Figure 2.3 SEM images showing the representative morphology of IMCs at eutectic In-Sn(l)/Ni(s) interface after soldering reactions at various temperatures for 240 min: 250°C and b) 400°C [2.4]	23
Figure 2.4 Ni-In phase diagram from Ref. [2.12]	24
Figure 2.5 Ni-Sn phase diagram from Ref. [2.13]	24
Figure 2.6 SEM images showing the representative morphology of IMCs at eutectic In-Sn(l)/Nb(s) interface after soldering reactions at 192°C for 5 months: a) cross-sectional view and b) top view [2.18]	27
Figure 2.7 A plot presenting the variation of IMC growth thickness with time for In-Sn(l)/Nb(s) reaction couple at 192°C [2.18]	28
Figure 3.1 A schematic diagram illustrating a representative electroplating cell set-up	35
Figure 4.1 Schematic diagram illustrating a typical, three-electrode electrodeposition cell configuration applied in this work	53

Figure 4.2 Schematic diagram illustrating a three-electrode cell configuration utilised for EQCM measurements	58
Figure 4.3 Schematic diagram illustrating micro-machining process by SEM/FIB for TEM sample preparation: a) Pt layer deposited on top of an area of interest; b) preparation of two trenches at both sides of the Pt deposit; c) 'U'-cut of the thin film sample for lift-out; d) thin film sample attached to Omniprobe and lifted out and e) thin film attached to copper grid ready for further thinning	61
Figure 4.4 SEM image showing a TEM thin foil sample prepared using focused ion beam milling where the leftmost end is the area of interest	62
Figure 4.5 Schematic diagram illustrating the four-point probe configuration for thin film resistance measurements	64
Figure 4.6 A representative optical micrograph presenting a 95.8Ni-4.2Nb coated sample surface after soldering with eutectic 52In-48Sn solder from a side-view (blue lines set to facilitate contact angle (CA) measurement whilst the yellow angle denotes the CA)	65
Figure 5.1 Potentiostatic curve showing a typical anodic dissolution of Nb metal (ca. 0.2g) in reline at + 7V (vs. Nb) and 120°C	68
Figure 5.2 Photographs showing the appearance of the Nb metal sheet after anodic dissolution at a) +3 V and b) + 7 V (vs. Nb wire) for 60 min	69
Figure 5.3 Cyclic voltammograms of a glassy carbon electrode immersed in ChCl:2Urea DES containing 0.2 M NbCl ₅ at a range of temperature from 25°C to 125°C and a scan rate of 100 mV/s	70
Figure 5.4 An enlarged scale (from -2 to -1 V) of cyclic voltammograms (shown in Figure 5.3) of a glassy carbon electrode immersed in ChCl:2Urea DES containing 0.2 M NbCl ₅ at a range of temperatures from 25 to 125°C and a scan rate of 100 mV/s.....	71
Figure 5.5 Cyclic voltammograms of a glassy carbon electrode immersed in ChCl:2Urea DES at a range of temperature from 80 to 125°C and a scan rate of 100 mV/s	71
Figure 5.6 Cyclic voltammograms of a glassy carbon electrode immersed in a ChCl:2Urea DES in the presence (solid line) and absence (dashed line) of 0.2 M NbCl ₅ at 125°C and a scan rate of 100 mV/s	72
Figure 5.7 Cyclic voltammograms of a Cu substrate (Surface area: 1 cm ²) immersed	

- in reline in the presence (solid line) and absence (dashed line) of 0.2 M NbCl_5 at 125°C and a scan rate of 100 mV/s (initiating from the OCP) 73
- Figure 5.8 A cyclic voltammogram of a Cu substrate (Surface area: 1 cm²) immersed in reline dissolved with 0.2 M NbCl_5 at 125°C and a scan rate of 100 mV/s initiating from the OCP, the insets show the initial 60 seconds of potentiostatic trials carried out at a) -1.50 V (along with its counterpart in the absence of NbCl_5); b) -1.25 V & c) -0.60 V (vs a silver quasi reference electrode) and isothermally at 125°C 74
- Figure 5.9 Secondary electron images showing the surface morphology of electropolished Cu: a) as-prepared and immersed in reline system dissolved with 0.2 M NbCl_5 following potentiostatic trials for 60 min b) at -0.6 V, c) at -1.25 V and d) at -1.5 V (vs. Ag wire) at 125°C 75
- Figure 5.10 Cyclic voltammograms of an electropolished Cu substrate (surface area: 1 cm²) immersed in Reline solution containing anodically dissolved Nb (6 g/L or 64.5 mM) or 0.2 M NbCl_5 at 125°C. Scan rate of 20 mV/s initiating from the OCP 77
- Figure 5.11 Cyclic voltammogram of an electropolished Cu substrate (surface area: 1 cm²) immersed in a mixture of 3ethylene glycol-1 NbCl_5 at 100°C at a scan rate of 20 mV/s initiating from the OCP 78
- Figure 5.12 Secondary electron images and in-lens image showing the surface of electropolished Cu immersed in reline a) without and b) with 0.2 M NbCl_5 following a potentiostatic trials at -1.5 V vs. Ag at 110°C for 1 hr and corresponding enlarged X-ray spectrum c) showing co-deposited Pt content 80
- Figure 5.13 Photograph showing more viscous and dark-coloured Reline solution resulted by the 'poisoning' of loosely structured graphite CE 81
- Figure 5.14 a) BSD and b) In-lens images of a Cu substrate surface following the electrolysis in Reline dissolved with 5g/L Nb dissolved at -1.8 V (vs. Nb wire) and at 200°C for 2 hrs suggesting polyhedral voiding imposed by graphite counter electrode 81
- Figure 5.15 In-lens images at different magnifications showing the surface morphology of Ag-rich deposits following electrolysis in Nb dissolved in $\text{ChCl}_2\text{:2Urea}$ IL at 150°C for 1 hr 82
- Figure 5.16 A cyclic voltammogram of an electropolished Cu substrate (surface area: 1 cm²) immersed in a reline solution anodically dissolved with 6 g/L Nb at 180°C and a scan rate of 20 mV/s initiating from the OCP 83
- Figure 5.17 Initial 15 seconds of a potentiostatic trial carried out at -1.80 V (vs. a Nb

wire reference electrode) at 110°C from the solution giving the voltammetric response shown in Figure 5.16	84
Figure 5.18 Secondary electron images showing the surface morphology of Ni-Nb deposits obtained following the electrolysis in Reline anodically dissolved with 6 g/L Nb (with an uncertain amount of Ni ions accidentally introduced) at 180°C for 1 hr ..	84
Figure 5.19 Area-scan X-ray spectrum showing the composition of Ni-Nb alloy deposit on an electropolished Cu substrate from Figure 5.18 (b)	84
Figure 6.1 In-lens SEM images depicting the representative surface morphology of Ni-Nb coatings deposited from Bath 1 at 100°C & 60 rpm for 10 min at a current density of a) 100, b) 300 and c) 400 mA/cm ² with the EDX composition noted (at.%)	91
Figure 6.2 In-lens SEM images showing the representative surface morphology of Ni-Nb electrodeposited from Bath 2 at 100°C & 240 rpm at a current density of a) 30, b) 50, c) 100, d) 150, e) 300 and f) 400 mA/cm ² with an equivalent charge passage of 360 C per cm ² with the EDX composition noted (at.%)	94
Figure 6.3 High magnification in-lens SEM images illustrating the representative surface morphology of a) the centre of the Ni-Nb coating shown in Fig. 6.2 (c), and the b) centre and c) edge of the Ni-Nb coating shown in Fig. 6.2 (d), electrodeposited from Bath 2 at a) 100 and b-c) 150 mA/cm ²	95
Figure 6.4 Secondary electron image a) illustrating the representative surface morphology of 94.3Ni-5.7Nb deposited from Bath 2 at 100°C & 240 rpm at 80 mA/cm ² for 10 min, with the corresponding X-ray maps of b) Cu K α , c) Ni K α and d) Nb L α ...	96
Figure 6.5 Secondary electron images presenting the central cross-section of Ni-Nb deposited from Bath 2 at 240 rpm and 100°C at a) 30, b) 50, c) 100, d) 150, e) 300 and f) 400 mA/cm ² with an equivalent charge of 360 C per cm ² passed	98
Figure 6.6 Secondary electron images illustrating the representative surface morphology of Ni-Nb deposited from a PG-based solution at 100°C and 200 mA/cm ² for a-b) 10 min, c-d) 20 min and e-f) 30 min (parallel ridges probably due to rolling lines present on the underlying copper substrate)	100
Figure 6.7 Secondary electron images and the corresponding X-ray maps illustrating the representative cross-sections of Ni-Nb deposited from a PG-based solution at 100°C and 200 mA/cm ² for a) 10 min, b) 20 min and c) 30 min	101
Figure 6.8 In-lens SEM images showing the typical surface morphology of Ni-Nb electrodeposited from Bath 3 at 240 rpm & 100°C at a) 50, b) 100, c) 150, d) 300 and	

e) 400 mA/cm² with an equivalent charge passage of 360 C per cm² with the atomic composition noted (at.%) 103

Figure 6.9 Secondary electron images illustrating the central cross-section of Ni-Nb deposited from Bath 3 at 240 rpm and 100°C & at a) 50, b) 100, c) 150, d) 300 and e) 400 mA/cm² with equivalent charge passage of 360 C per cm² 104

Figure 6.10 Secondary electron images illustrating the representative surface morphology of Ni-Nb deposited on Cu substrate at 100°C & 240 rpm from Bath 5 (a-d) and Bath 6 (e-h) at 30 (a, e), 50 (b, f), 100 (c, g) and 150 mA/cm² (d, h) with equivalent charge passage of 360 C per cm² 107

Figure 6.11 Bar charts illustrating the variations in the a) relative metal percentage of Nb (at.%) in the Ni-Nb electrodeposits and in b) average central coating thickness with cathodic current density and NaBH₄ concentrations in the electrolyte (suggested from metallographic cross sectioning) 109

Figure 7.1 Cross sectional STEM images of a Ni-Nb coating electrodeposited from Bath 2 at 100°C & 240 r.p.m. at a current density of 80 mA/cm² for 60 min acquired at × 40,000 magnification: a) BF and b) HAADF and at × 57,000: c) BF and d) HAADF, and e) selected area diffraction pattern from the circled zone noted in a) 113

Figure 7.2 Simplified schematic diagram showing the grain structure formation mechanism of Ni-Nb electrodeposition in the present study 115

Figure 7.3 STEM cross-sectional image a) of a Ni-Nb electrodeposited from Bath 2 at 100°C & 240 rpm at 80 mA/cm² for 60 min with the elemental maps of b) Ni Kα, c) Nb Lα, d) O Kα and e) Cu Kα and f) a plot presenting the EDX composition analysis results indicated in a) 117

Figure 7.4 XPS Compositional depth profiling of a Ni-Nb electrodeposited from Bath 2 at 100°C & 240 r.p.m. and at a cathodic current density of 100 mA/cm² for 45 min...119

Figure 7.5 XPS Ni 2p_{3/2} narrow spectra of a Ni-Nb coating electrodeposited from Bath 2 at 100°C & 240 rpm at 100 mA/cm² for 45 min after the brief sputter 120

Figure 7.6 Deconvoluted XPS Nb 3d narrow spectra of a Ni-Nb coating electrodeposited from Bath 2 at 100°C & 240 rpm at 100 mA/cm² as a function of Ar⁺ ion beam (500 eV) sputtering time: a) 0 s, b) 240 s and c) 3800 s and d) of both a pure Nb₂O₅ and a pure Nb metal sample (after sputtering off the surface native oxides).121

Figure 7.7 Relative atomic percentage depth profiling of three niobium chemical states as a function of Ar⁺ ion monomer beam sputtering time based on deconvoluted XPS spectra of a Ni-Nb deposited sample from Bath 2 at 100°C & 240 rpm at 100

mA/cm ² for 45 min	123
Figure 7.8 XPS Nb 3d narrow spectra of a pure Nb ₂ O ₅ powder specimen as a function of Ar ⁺ ion monomer beam etching time using an ion energy of either a) 200 eV or b) 500 Ev	124
Figure 7.9 XPS Ni 2p _{3/2} narrow spectra of a Ni-Nb coating electrodeposited from Bath 2 at 100°C & 240 rpm at 100 mA/cm ² (and ambient stored for 30 days) as a function of Ar ⁺ GCIB beam sputtering time: a) 60 s and b) 900 s	126
Figure 7.10 XPS Nb 3d narrow spectra of a Ni-Nb coating electrodeposited from Bath 2 at 100°C & 240 rpm at 100 mA/cm ² (and ambient stored for 30 days) as a function of Ar ⁺ GCIB beam sputtering time: a) 60 s, b) 900 s and c) 4920 s	128
Figure 7.11 XPS Nb 3d narrow spectra of a pure Nb ₂ O ₅ control sample as a function of Ar ⁺ GCIB beam sputtering time	129
Figure 7.12 Galvanostatic and EQCM plots showing the variations in the deposition potential (vs. Nb wire) and mass on the cathode with time for Ni-Nb electrodeposition from Bath 2 at 100°C & 240 rpm at 100 mA/cm ²	131
Figure 7.13 Two sections of EQCM plots showing the variations in the deposition potential (vs. Nb wire) and mass on the cathode with time for Ni-Nb electrodeposition from Bath 2 at 100°C & 240 rpm at 100 mA/cm ²	131
Figure 7.14 A schematic diagram showing the Ni deposition mechanism in the present study	132
Figure 7.15 A schematic diagram showing one possible co-deposition mechanism for NbO _x in the present study	133
Figure 7.16 A subsection of galvanostatic plot showing the variations in the deposition potential (vs. Nb wire) with time for Ni-Nb electrodeposition from Bath 2 at 100°C & 240 rpm at 100 mA/cm ²	134
Figure 8.1 Graph presenting the average sheet resistance of untreated Cu sheet and Ni-based, deposited specimens measured using the four point probe method	138
Figure 8.2 SEM images showing the representative interfacial microstructure of pure Ni and Ni-NbO _x deposited samples after reaction with molten 52In-48Sn: a) 7 μm thick, pure Ni for 72 hours and b) 7 μm thick, 99.4Ni-0.6Nb for 72 hours, c) 7 μm thick, 96.8Ni-3.2Nb for 216 hours and d) 2 μm thick, 94.0Ni-6.0Nb for 9 hours	142
Figure 8.3 SEM images showing the representative surface morphology of a 2 μm	

thick 94.0Ni-6.0NbO _x deposited sample that reacted with molten Sn-In solder at 200°C for 5 hours after chemical stripping away the solder	143
Figure 8.4 a) SEM image showing the representative interfacial microstructure of a 99.4Ni-0.6Nb deposited samples after reaction with molten Sn-In solder at 200°C for 72 hours and b) a plot showing the EDX point analysis results indicated in a), (I) to (V) represent zones observed across the interfaces	145
Figure 8.5 a) SEM image showing the interfacial microstructure of a 96.8Ni-3.2Nb deposited samples after reaction with molten Sn-In solder at 200°C for 192 hours and b) a plot showing the EDX point analysis results indicated in a), (I) to (V) represent zones observed across the interfaces	147
Figure 8.6 a) SEM image showing the interfacial microstructure of a 96.8Ni-3.2Nb deposited samples after reaction with molten Sn-In solder at 200°C for 192 hours and the corresponding X-ray maps showing b) Sn L α , c) In L α , d) Ni K α , e), Nb L α , and f) Cu K α	148
Figure 8.7 a) SEM image showing the interfacial microstructure of a 94.0Ni-6.0Nb deposited samples after reaction with molten Sn-In solder at 200°C for 9 hours and b) a plot showing the EDX point analysis results indicated in a), (I) to (III) represent zones observed across the interfaces	150
Figure 8.8 a) STEM bright field image showing the interfacial microstructure of a 96.8Ni-3.2Nb deposited sample after reaction with molten Sn-In solder at 200°C for 192 hours, b) a magnified image of a) showing the EDX line scan and c) a plot showing the EDX line scan analysis results indicated in b), (I) to (V) represent zones observed across the interfaces	152
Figure 8.9 TEM bright field image of the IMCs growing into the solder from 96.8Ni-3.2NbO _x deposited sample after reaction with liquid In-Sn solder at 200°C for 192 hours	153
Figure 8.10 a-b) STEM bright field images of the consumed barrier layer (upper region, Zone II) from 96.8Ni-3.2NbO _x deposited sample after reaction with liquid In-Sn solder at 200°C for 192 hours and c) the selected area electron diffraction pattern taken from the circled area in b)	154
Figure 8.11 a) STEM bright field image of the barrier layer region from 96.8Ni-3.2NbO _x deposited sample after reaction with liquid In-Sn solder at 200°C for 192 hours and b) the corresponding elemental map of Nb L α	155
Figure 8.12 a) STEM bright field image of the consumed barrier layer (lower region, Zone III) from 96.8Ni-3.2NbO _x deposited sample after reaction with liquid In-Sn solder	

at 200°C for 192 hours and b) the selected area electron diffraction pattern taken from the circled area in a) 156

Figure 8.13 Schematic diagrams of the microstructure evolution of Ni-NbO_x barrier layer after interaction with liquid 52In-48Sn solder at 200°C.....158

List of Tables

Table 1.1 A summary of typical packaging hierarchy for electronics assemblies [1.4]..2	
Table 1.2 A comparison of various wire bonding metallurgy system for high temperature electronics applications	7
Table 1.3 An overview of various high temperature die attach materials	9
Table 1.4 An overview of the reliability concerns with various leadframe materials in combination with surface metallisations or die at high temperatures	11
Table 1.5 An overview of representative promising solder strategies for high temperature electronics packaging	14
Table 3.1 Important physical properties of niobium [3.1]	32
Table 6.1 Formulations of Ni-Nb electrodeposition electrolytes (g/L (M))	90.
Table 7.1 A summary of XPS depth profiling and XPS analysis parameters for Ar monomer ion beam and GCIB sources	125
Table 8.1 A summary of contact angle measurements of soldered Ni-Nb electrodeposited specimens	139
Table 8.2 Summary of the barrier lifetimes of pure Ni and Ni-NbO _x layers in contact with molten 52In-48Sn solder at 200°C	141
Table 8.3 Atomic compositions of the five zones identified across the interfaces from 96.8Ni-3.2NbO _x deposited sample after reaction with liquid In-Sn solder at 200°C for 192 hours	153
Table 8.4 Atomic compositions and crystal structure of the three reacted zones identified across the interfaces from 96.8Ni-3.2NbO _x deposited sample after reaction with liquid In-Sn solder at 200°C for 192 hour.....	157

Glossary of Abbreviations

AES	Auger Electron Spectroscopy
at. %	Atomic Percent
BCC	Body Centred Cubic
BF	Bright Field
CA	Contact Angle
CCE	Cathodic Current Efficiency
CE	Counter Electrode
ChCl	Choline Chloride
CN	Cyanide
CTE	Coefficient of Thermal Expansion
CV	Cyclic Voltammetry
DES	Deep Eutectic Solvent
ECA	Electrically Conductive Adhesive
EDX	Energy Dispersive X-ray Spectroscopy
EG	Ethylene Glycol
EHT	Extra High Tension Voltage
EQCM	Electrochemical Quartz Crystal Microbalance
FAP	Tris(perfluoroalkyl) Trifluorophosphate
FCC	Face-centred Cubic
FE	Faradic Efficiency
FIB	Focused Ion Beam
GC	Glassy Carbon
GCIB	Gas Cluster Ion Beam
HAADF	High Angle Annular Dark Field
HBD	Hydrogen Bond Donor
IC	Integrated Circuit
IL	Ionic Liquid
IMC	Intermetallic Compound
LSV	Linear Sweep Voltammetry

NHE	Normal Hydrogen Electrode
OCP	Open Circuit Potential
PCD	Primary Current Distribution
PDF	Powder Diffraction File
PG	Propylene Glycol
PVD	Physical Vapour Deposition
PWB	Printed Wiring Board
r.p.m.	Revolutions Per Minute
SADP	Selected Area Diffraction Pattern
SCD	Secondary Current Distribution
SCE	Saturated Calomel Electrode
SEM	Scanning Electron Microscopy
S.G.	Specific Gravity
SMSI	Strong Metal-Support Interaction
STEM	Scanning Transmission Electron Microscopy
TEM	Transmission Electron Microscopy
TFSA	Bis(trifluoromethylsulfonyl) Amide
WE	Working Electrode
wt.%	Weight Percent
XPS	X-ray Photoelectron Spectroscopy
XRD	X-ray Diffraction
Z	Atomic Number

Context of Research

High temperature electronics assemblies operate at temperatures often above the conventional design limit (125°C). The harsh conditions demand control over the interfacial microstructural stability of the solder joints at the electronics packaging level. This is primarily due to excessive intermetallic compounds (IMCs) that can form and continuously grow during high temperature operation, which practically renders conventional solder barrier metallisations inadequate.

Niobium (Nb) has been suggested as a promising high temperature diffusion barrier candidate, but it is thermodynamically impossible to be electroplated from conventional aqueous systems. The recent introduction of non-aqueous room temperature ionic liquids (especially deep eutectic solvents (DESs)) has resurrected the interests into Nb electrodeposition due to their chemical robustness and large potential windows.

Research Objectives

The present work explores a novel electrochemical route to deposit Nb-based coatings from non-aqueous ionic liquid-based electrolytes. With a chronologically developed understanding of Nb electrochemistry, a task specific electrolyte based on DESs has been prepared to electrodeposit Nb-based metal coatings. The structure and property of the resulted coatings has been optimised through electrolyte formulation and process control, for high temperature diffusion barrier applications. Their suitability as a solder diffusion barrier layer to prevent interdiffusion and intermetallic formation in liquid solder interconnections was examined.

Contributions to the Body of Knowledge

1. An off-eutectic Type IV DES electrolytic system based on glycols has been developed, which allows for effective electrodeposition of Ni-NbO_x metal coatings;
2. A novel Ni-NbO_x composite coating material has been developed, the composition and microstructure of which is tunable through the adjustment of electrolyte chemistry and electrodeposition parameters;
3. The diffusion barrier performance of the coatings has been evaluated with respect to thin film sheet resistance, solderability and solder diffusion barrier efficacy, which have shown the possibility of applying the current treatment to high temperature electronics packaging;
4. The underlying mechanism of NbO_x as a Ni diffusion barrier enhancer has been accounted for.

Structure of Thesis

Chapter 1 briefly introduces high temperature electronics packaging with a central focus on the interconnection materials. Chapter 2 contains a review of the liquid solder interconnections and associated contact metallisations, which have been a promising solder joint strategy for high temperature electronics packaging. Chapter 3 is concerned with the possibility of electrodeposition to produce Nb-based metal finishes. Chapter 4 describes experimental techniques for preparation of Nb-based electrodeposits, the subsequent microstructural characterisations and diffusion barrier performance assessment. Chapter 5 enquires about Nb electrochemistry in Type III and Type IV eutectic solvents and derivatives and introduces an alternative approach to co-deposit Nb-based metal coatings, i.e. Ni-Nb co-deposition. Chapter 6 presents the evolution of the electrodeposition process through

control over bath formulation and electrodeposition parameters. Chapter 7 describes the results obtained from the electrochemical, microstructural and spectroscopic characterisations of the resulted electrodeposits. Chapter 8 presents the results acquired from the diffusion barrier performance assessment of the electrodeposited samples, which include the measurements of the thin film electrical conductivity and solderability, as well as the solder diffusion tests. The dissertation ends with conclusions and future work presented in Chapter 9.

Chapter 1

High Temperature Electronics Packaging

This chapter is devoted to introducing high temperature electronic packaging with a central focus on the interconnection materials. It begins with a general overview on the development and hierarchy of electronics packaging. Following this, the implications of harsh conditions to the properties and reliability of materials at various packaging levels are collated, whilst some fundamental material-related limitations and areas worthy of further development are identified.

1.1 Introduction to Electronics Packaging

Since the replacement of cumbersome vacuum tubes with the first-generation solid state devices [1.1], the past half-century has witnessed the unprecedented prosperity of the microelectronics industry. This can be primarily ascribed to two factors: first is the revolutionary invention [1.2] of planar integrated circuits (IC) which mount the solid state devices onto a single semiconductor wafer, initialising a trend of ever-increasing scale integration and hence steadily improved electronic functionality; second is that the continuous miniaturisation, which has downsized the transistor from 10 μm to ca. 30 nm [1.3], greatly reduces the cost and elevates the performance and power of electronics products.

Electronics packaging is a major technology of electronics engineering, which is set, firstly, to provide protection to the IC chip; and furthermore, to establish the interconnection between IC chips and other electronic components such

as printed wiring boards (PWBs), transformers and connectors for the purpose of electrical conduction, thermal dissipation and, in some cases (e.g. surface mount technology), mechanical support [1.4].

1.2. Electronics Packaging Hierarchy

Electronics assemblies are generally packaged at a number of levels, collectively known as a packaging hierarchy, as is summarised in **Table 1.1**. The electronic packaging generally begins at the IC chip or wafer level (see **Figure 1.1**), involving IC chip fabrication (i.e. semiconductor device level), the interconnection of the IC chip to leadframe or substrate via either wire bonding, tape-automated bonding or flip chip bonding yielding an IC microelectronic carrier (i.e. first level packaging), followed by the interconnection of the IC chip packages to either printed wiring boards (PWBs) or substrate through e.g. surface mount technology (i.e. second level packaging). Finally, the PWBs are assembled to motherboard or backplane (i.e. third level packaging) ready for external housing.

Packaging level	Interconnecting units	Interconnection approach
First level	Between the IC chip & modules	- Wire bond
		- Tape-automated bond
		- Flip chip bond
Second level	Connecting the module & other components (capacitors and resistors) to printed wiring board (PWB)	- Pin-through-hole technology - Surface mount technology
Third level	Motherboard or backplane	-

Table 1.1 A summary of typical packaging hierarchy for electronics assemblies [1.4]

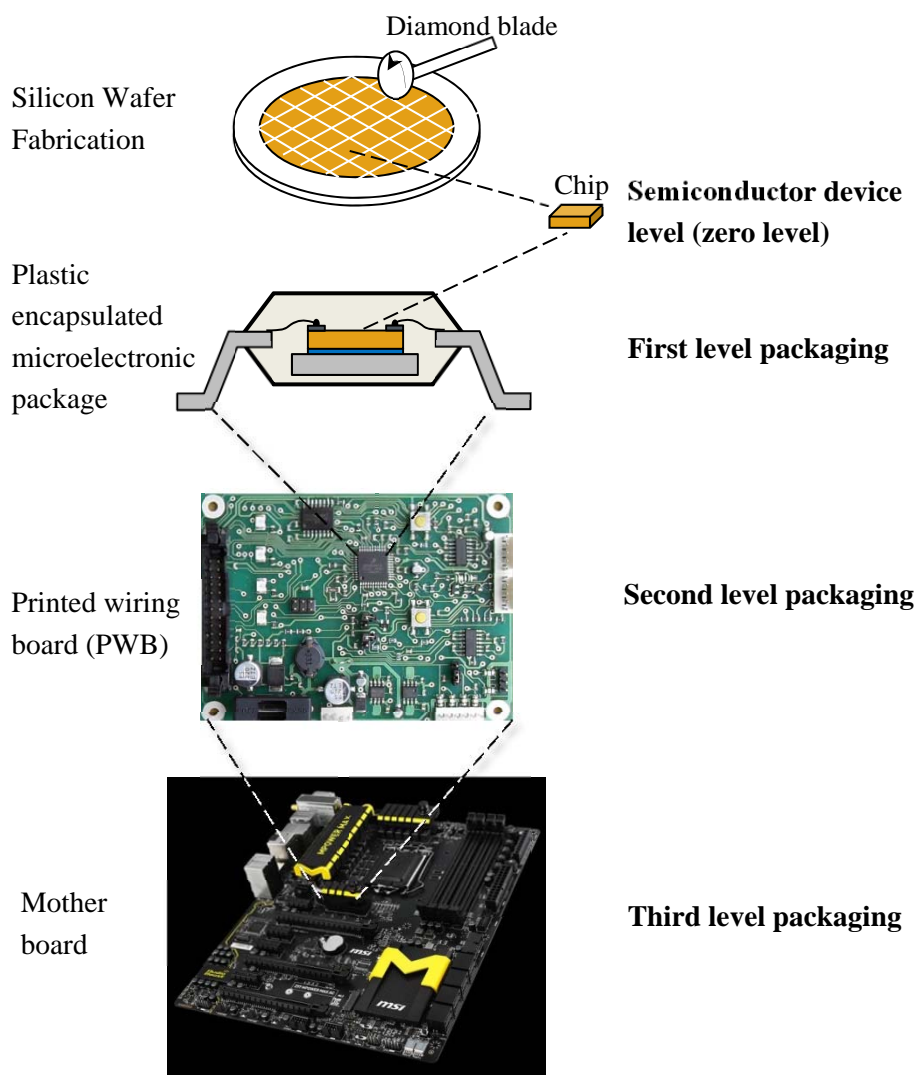


Figure 1.1 A schematic diagram illustrating the electronics packaging hierarchy comprising of at least four packaging levels [1.4]

1.3 Introduction to High Temperature Electronics Packaging

As an expanding extension of the consumer electronics sector, high temperature electronics industry targets the development of electronics systems operating under harsh conditions, which normally involve elevated temperatures far exceeding the conventional design limit (125°C) [1.5], often together with other hostile factors such as humidity, mechanical vibrations and thermal cycles (thermomechanical fatigue). This is even complexed by the ever-shrinking geometry of microelectronics, where higher heat flux is

encountered due to increasing electrical power density. Typical high temperature applications include, but are not limited to, heat engines in air and ground vehicles, deep wells for mineral and petroleum exploitation, as well as chemical processing. With such a service condition boundary stretched and a direct transition or modification from conventional electronics paradigm unwarranted, considerable amounts of technology challenges do exist with respect to both electronic components and the associated packaging. In terms of packaging, the temperature concerns generally lie in the sourcing and development of interconnection materials with desired mechanical, thermomechanical, electrical and thermal conduction properties, as well as enhanced safety and reliability when exposed to hostile environments. In the following, the implications of elevated temperatures to electronics package units at various packaging levels are reviewed, from semiconductor device, through first level to second level interconnections. The variations of their properties with temperature and the associated impacts on the interconnection stability and reliability will be considered, and the current material-related limitations and future developments are identified.

1.3.1 Implications of High Temperatures at Semiconductor Device Level

The integrated circuit (IC) chips, or semiconductor devices, are the basic elements and principal functioning units in an electronics assembly. Electric charge passage of semiconductor materials proceeds through the motion of free electrons and holes, collectively known as charge carriers. Additions of dopants (i.e. impurity atoms) into a semiconductor greatly elevate its charge carrier concentration. The p-type dopants increase the free hole density whilst the n-type ones rise the free electron density. A semiconductor may contain regions predominantly with either free holes or free electrons, with the former described as p-type regions, the latter named the n-type. It is the interphases between the two regions, p-n junctions, that dictate the useful electronic behaviour of the semiconductor.

Generally, silicon-based devices operate satisfactorily at temperatures up to 200°C [1.6]. At temperatures above 250°C, semiconductor materials with comparatively wide bandgaps¹ (e.g. gallium nitride (GaN: 3.4 eV) and silicon carbide (SiC: 2.9 eV) (cf. Si: 1.1 eV), all at 25°C) are more suitable to use due to their relative insensitivity to heat [1.7]. This is mainly because, intrinsic carrier concentration increases with elevating temperature, which elevates the leakage current, causing current blockage at the junction. Semiconductors with larger bandgaps exhibit lower concentrations of intrinsic carriers and hence lower leakage current, which, in turn, increases their maximum operating temperatures. The applicability of high bandgap materials like SiC for high temperature semiconductor devices has been widely researched, with a focus on the development of reliable contact metallisation systems from a packaging perspective.

1.3.2 Implications of High Temperatures for First-level Packaging

First level packaging provides the chip to package (modules) interconnection. The interconnection methods fall into three categories, viz. wire bonding, automated tape bonding and flip chip bonding.

It is usually this microfabrication step that defines the upper limit for the operation temperature of electronic systems partially due to the relatively low heat tolerance of the package elements incorporated. At elevated temperatures, the reliability of the interconnection is generally affected by wire bonds, die attach, plastic encapsulants and leads frames. In the following, the temperature concerns for these package elements in the first level chip-to-module interconnection are addressed.

1.3.2.1 Wire Bonds

Wire bonding is the use of a fine metal wire (usually made of gold, aluminum or

¹ Bandgap: an energy range in a solid material where no electron states exist.

copper) to attach the input/output (I/O) pad on the chip (or die) to the associated package, as is illustrated in **Figure 1.2**. This point-to-point interconnection technology, pioneered by AT&T in the late 1940s, has seen industrial popularity (>85% market share in 2010 [1.8]) due to its high assembly flexibility, low production defect rates, low production costs and ease of wire replacement. However, with the ever-decreasing dimensions of electronics, the drawbacks of wire bonding have become increasingly pronounced, such as large chip-to-package lengths (which degrades the electrical performance), large footprint (small packaging density) and relatively low reliability.

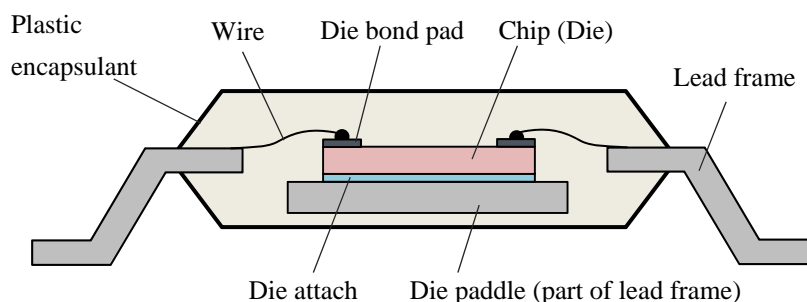


Figure 1.2 A schematic diagram illustrating the cross section of a representative, first level, integrated circuit package

The temperature concerns with wires and wire bonds lie largely in the formation of intermetallic phases at the bond-pad interface. The excessive growth of intermetallic compounds (IMCs) through solid state interdiffusion of metal elements between the wire and bond pad induces mechanical stress and Kirkendall voiding², which decreases the bond strength potentially causing brittle failure of the interconnection. The diffusion rate (or diffusion coefficient) of these IMC forming species rises greatly with temperature, leaving the IMC growth a major high temperature reliability risk. This is often combined with the effect of mechanical vibrations usually encountered in a harsh environment (e.g. automobile and geographic drilling), which may cause severe bending

² Kirkendall voiding: voids formed from interdiffusion, acting as stress concentrators and providing straightforward pathways for crack propagation and hence detrimental to interface bond strength.

and distortion of the wires instigating short circuiting [1.8]. A comparison of various wire bond metallurgy systems operating at elevated temperatures is summarised in **Table 1.2**. Even though the conventional Al-Au metallurgical system may not seem adequate at elevated temperatures, the possibility of alternatives like Cu-Al, Ni-Al and even monometallic systems has been developed.

Wire/pad system	Effect of high temperature on metallurgical system	Upper use limit
Au – Al	1) Weak mechanical bond due to Au-Al IMC formation & voiding; 2) Reduction in electrical conductivity also due to Kirkendall voiding [1.9].	175°C
Cu – Al	1) Suppressed Cu-Al IMC formation presumably due to atomic radius misfit between Cu and Al [1.10]; 2) Little voiding occurs; 3) Elevated maximum use temperature (cf. Au – Al).	200°C
Al – Ni	1) Ni acts as a diffusion barrier, leading to much slower Al-Ni IMC formation [1.11]; 2) Little Kirkendall voiding occurs.	300°C
Al – Al or Au-Au	1) Reliable monometallic wire bonding; 2) Stable interface due to the absence of IMC formation or any galvanic corrosion; 3) Fatigue failure at the neck/heel of wires due to wire annealing upon thermal ageing [1.12]	> 660°C

Table 1.2 A comparison of various wire bonding metallurgy system for high temperature electronics applications

1.3.2.2 Die Attach

Die attach materials furnish the interconnection between a die and a leadframe or substrate, as is illustrated in **Figure 1.2**. Generally these materials fall into five categories: eutectic die attach solder alloys, soft solders, silver glass, epoxy adhesives and alternative resins, amongst which the eutectic solder alloys and conductive epoxy see most widespread applications [1.13]. For high

temperature interconnection, the general property requirements for die attach materials are more stringent than those for room temperature applications, comprising of high solidus and liquidus temperatures, good electrical and thermal conductivity characteristics, compliant thermal expansion coefficient (CTE) mismatch between the die and substrate, as well as long-term mechanical and chemical stability across the die/attach/substrate interfaces. High Pb solder alloys have been extensively employed as reliable die attach materials. However, due to the recent legislation ban of Pb, considerable sourcing efforts have been made for Pb-free solder replacements. A summary of high temperature die attach materials with an overview on their applicability for harsh conditions, together with merits and drawbacks, is presented in **Table 1.3**.

1.3.2.3 Plastic Encapsulants

Plastic encapsulants are polymer-based materials used to encase integrated circuit (IC) chips that have undergone interconnection (e.g. wire-bonded and mounted to the substrate through die attaches) (See **Figure 1.2**). Moulding compounds such as epoxies and silicones exhibit sound mechanical properties and acceptable moulding temperatures and hence are the most common encapsulant materials.

The upper temperature limit for the use of moulding compounds is defined by their depolymerisation temperatures (190-230°C for epoxies and 260-280°C for silicones), at which the polymer turns into a viscous mixture of low molecular weight monomers and oligomers, losing its mechanical integrity. Below the depolymerisation temperatures, thermal stress arising from thermal mismatch may also lead to fatigue and fracture of the plastic encapsulants. For the aforementioned reasons, the use of epoxies is not recommended above 180°C and silicone gels not above 260°C.

Die Attach material	Advantages	Major concerns
Ag filled adhesives [1.13]	Lower processing temperatures, low cost and impact low thermal stress to die.	<ul style="list-style-type: none"> - Maximum temperature up to 200°C; - Electrical conductivity constrained by dispersion of Ag fillers; - Outgassing at elevated temperatures.
Pb-Sn solders	High ductility and fair thermal conductivity	<ul style="list-style-type: none"> - Phased out due to toxicity of Pb content
Au based system: e.g. Au-Sn solders	Low processing temperatures, good thermal and electrical conductivity, good solderability and excellent creep resistance [1.14]	<ul style="list-style-type: none"> - Concerns over ‘gold embrittlement’, formation of hard, vast Sn-Au IMCs platelets, causing brittle fracture.
Zn based system: e.g. Zn-Sn solders	Low cost, excellent thermal conductivity, electrical property and good mechanical stability when diffusion barriers (e.g. Au/TiN) are applied	<ul style="list-style-type: none"> - Susceptibility of Zn to oxidation and hence to rusting; - Excessive solid-liquid transformation causing destructive expansion during reflow (250°C) [1.15]
Bi based system: e.g. Bi-Ag solders	Addition of Ag hugely improves its ductility [1.16]	Relatively inferior electrical and thermal conductivity and poor workability
Ag glass	Fair thermal and electrical conductivity;	<ul style="list-style-type: none"> - High processing & firing temperatures; - Lengthy pre-drying step before firing.
Ag-based nanoparticle systems	Lower sintering pressure and lower temperatures due to large surface area of nanoparticles.	<ul style="list-style-type: none"> - Lower electrical and thermal conductivity than bulk Ag.

Table 1.3 An overview of various high temperature die attach materials

1.3.2.4 Leads and Lead frames

A lead frame is usually an electrical conducting metal framework (e.g. copper alloys, iron-nickel alloys (Alloy 42)) consisting of leads and a paddle to which the die (i.e. IC chip) is mounted via die attach materials (See **Figure 1.2**). Leads are separated after plastic encapsulation by cutting the outside-package part of the lead frame. The lead frame is normally deposited with silver, tin-based solders or nickel-palladium for improved solderability, corrosion resistance and oxidation resistance.

Lead frames and leads generally do not undergo significant degradation at temperatures below 200°C [1.7]. However, the electroplated layers on the lead frames may pose reliability risks under harsh conditions. The reliability concerns for lead frame metallisations operating at high temperatures are reviewed in **Table 1.4**. It can be recognised that, stress, introduced either by thermal mismatch or accelerated interdiffusion and reaction at elevated temperatures, is normally the origin for the degradation of the package element properties and reliability.

1.3.3 Implications of High Temperatures for Second-level Packaging

The second level packaging consists of the interconnection between the micro-chip carriers and a printed wiring board (PWB). It must furnish mechanical support, electrical and thermal conduction to the chip carriers. Practically it is realised by either through-hole or surface mount technology, with the former largely replaced with the latter due to the continuous miniaturisation of the electronics assemblies. The joining materials employed in this packaging level generally fall into two categories: electrically conductive adhesives and solders, which are considered with respect to their property variations and reliability concerns under hostile conditions.

Leadframe Substrates	Surface Metallisations (or Die)	High Temperature Concerns	Mitigation Strategies or Alternatives
Cu metal	Electrodeposited Au	Penetration of Cu through Au layer <i>via</i> accelerated diffusion	Insertion of a Ni diffusion barrier layer
Cu plated with Ni	Electrodeposited hard Au	Diffusion of hardening agents (Ni, Fe or Co) to Au surface above 125°C [1.7]	Use of thick, soft Au plating
Cu metal and alloys	Electrodeposited Sn	- Accelerated Sn-Cu IMC formation & hence interface instability above 100°C; - Sn whisker formation induced by Sn-Cu IMC growth and thermal stress.	- Use of Ni diffusion barrier to prevent IMC growth; - Pre-annealing and use of conformal coatings to retard whisker formation
Copper alloys	Silicon die and die attach	Thermal mismatch between Cu (16 ppm/K) and silicon die (2.3 ppm/K), inducing thermal stress upon heating [1.7]	- Use of leadframe materials with closer thermal expansion match (e.g. Alloy 42: 4.5 ppm/K)

Table 1.4 An overview of the reliability concerns with various leadframe materials in combination with surface metallisations or die at high temperatures

1.3.3.1 Electrically Conductive Adhesives

Electrically conductive adhesives (ECAs) are normally polymer-based composites consisting of a dielectric, curable polymer matrix reinforced with electrically conducting metal particles. A common ECA system is an epoxy thermoset reinforced with Ag flakes. The adhesion is achieved by chemical bonding formed upon polymer curing, where the metallic particles dispersed within constitute an electrical conduction path spanning the entire interconnection thickness. The mechanical and electrical properties of the ECAs, however, are susceptible to degradation at temperatures above 85°C. The adhesion can hardly be retained at the interfaces, not only between the

polymer and the metal particles which disrupt the electrical conduction, but also between the polymer and the underlying metallised substrate thereby undermining the joint strength. This basically restrained the application of ECAs as a second level packaging material for high temperature electronics.

1.3.3.2 High Temperature Solders

High temperature solders such as high lead solders (e.g. 95.5Pb-2Sn-2.5Ag) have been the predominant joint materials at the component-to-board attachment level under harsh conditions. This solder class generally exhibits excellent ductility and high melting points (above 300°C), with the latter preventing the solder joint from melting for most high temperature applications. However, such high melting points also raise the processing temperatures, enforcing all other component and joining materials at the second packaging level to be redesigned to accommodate the soldering process. As mentioned in the die attach materials (**Section 1.3.2.2**), the Pb content is legislatively banned by the RoHS (Restriction of Hazardous Substances) directive and WEEE (Waste Electrical and Electronic Equipment) directive, both by the EU. Therefore, interests have been resurrected in the search for Pb-free solder alternatives with similar property attributes to the Pb-containing ones.

Promising solder candidates are desired to have:

- 1) Relatively high homologous solidus temperature (the temperature below which an alloy is completely solid) to retain mechanical strength at elevated temperatures;
- 2) Excellent interfacial microstructural stability, achievable by suppressing the IMC formation and growth between the solders and the underlying metalised substrate and also by limiting electromigration in between;
- 3) Excellent thermomechanical fatigue resistance reflected in limited

microstructural evolution in the solder and in the limited time-dependent deformation (creep) of the solder in response to strains at elevated temperatures [1.7].

A summary of some promising lead-free solder alternatives is presented in **Table 1.5**, with their key attributes compared to those of the Pb-containing solders. Generally the control of microstructure stability at the interface between the solder joint and substrate is of great importance to the interconnection reliability. Unfortunately one predominant class of leadframe and substrate materials is copper metal and its alloys, which normally exhibit a high chemical affinity with major solder constituent elements such as Sn and Zn, giving excessive IMCs formation leading to brittle failure of the solder joints. The IMC formation is exacerbated at elevated temperatures, therefore, diffusion barrier metallisations are often required to retard the interdiffusion between these IMC forming species. The contact metallisations for high temperature electronics packaging are the focus of this work, which merits further discussion in **Chapter 2**.

1.4 Summary

In this chapter, high temperature electronics packaging is reviewed with a major emphasis on the interconnection materials employed at various packaging levels. At semiconductor device level, materials with wider bandgap such as SiC present a clear advantage over conventional Si on account of much reduced sensitivities to heat. For the first level packaging, the high temperature performance and reliability of common wire bond metallurgy systems, die attach materials, plastic encapsulants, as well as leads and leadframes are collated, where candidates promising for hostile environments or areas worthy of further investigations are recognised. At the second level interconnection, electrically conductive adhesives and high temperature, lead-free solders are compared with respect to the conventional high lead

materials. The applicability of lead-free solders for high temperature electronics packaging is clarified, with one of the promising solutions, liquid solder interconnection, to be further discussed in details in **Chapter 2**.

Solders	Advantages	Major concerns
95.5Pb-2Sn-2.5Ag	High melting points, high ductility and fair thermal conductivity	- Legislative banning due to toxicity of Pb content; - Poor wettability; - Poor thermomechanical fatigue resistance.
96.5Sn-3Ag-0.5Cu	Grain refinement strengthening giving high creep resistance at room temperature, good solderability	- Poor fatigue resistance at high strain levels and high mean temperatures.
95Sn-5Sb	Relatively high solidus temperature (234°C), good solderability, high tensile and shear strengths maintainable at elevated temperatures	- Slower response to time-dependent deformation; - Prone to brittle fracture when in tension [1.7].
20Sn-80Au	High melting point (280°C), good corrosion resistance, good creep behaviour [1.17]	- Expensive Au content; - Stiff solder not exhibiting much strain absorption [1.7]
Liquid solders: e.g. In-Sn solders	- Use of low melting point solder that regularly melt during service, eliminating strain hardening [1.18]	- Accelerated IMC formation with Cu degrading joint stability; - Diffusion barrier required to alleviate IMC growth.
95Zn-5Al	Low cost, good thermal and electrical conductivity [1.19].	- Excessive IMC formation with Cu leading to brittle fracture; - Zn content prone to corrosion and oxidation.

Table 1.5 An overview of representative promising solder strategies for high temperature electronics packaging

1.5 References

- [1.1] J. Bardeen, and W. H. Brattain, *Phys. Rev.*, **75**, 1208 (1949).
- [1.2] J. S. Kilby, *IEEE Trans. Electron. Devices*, **23**, 648 (1976).
- [1.3] S. E. Thompson, and S. Parthasarathy, *Mater. Today*, **9** (6), 20 (2006).
- [1.4] H. M. Tong, *Mater. Chem. & Phys.*, **40** (3), 147 (1995).
- [1.5] R. W. Johnson, J. L. Evans, P. Jacobsen, J. R. Thompson and M. Christopher, *IEEE Trans. Electron. Pack. Manuf.*, **27** (3), 164 (2004).
- [1.6] P. L. Dreike, D. M. Fleetwood, D. B. King, D. C. Sprauer and T. E. Zipperian, *IEEE Trans. Compon. Pack. Manuf. Technol. Part A*, **17** (4), 594 (1994).
- [1.7] F. P. McCluskey, T. Podlesak, and R. Grzybowski, *High Temperature Electronics*, CRC Press, 11 (1996).
- [1.8] M. Mirgkizoudi, C. Liu, P. P. Conway and S. Riches, *Microelectron. Reliab.* (In press) (2015).
- [1.9] G.G. Harman, *Wire Bonding in Microelectronics*, McGraw-Hill, New York, (1989).
- [1.10] S. Murali, N. Srikanth and C. J. Vath, *Mater. Res. Bull.*, **38** (4), 637 (2003).
- [1.11] F. P. McCluskey, R. R. Grybowski, L. Condra, D. Das, J. Fink, J. Jordan, and T. Torri, In *High-Temperature Electronic Materials, Devices and Sensors Conference*, 199 (1998).
- [1.12] R. C. Weast, *CRC Handbook of Chemistry and Physics*, 60th ed., CRC Press, Boca Raton, FL, (1979).
- [1.13] V. R. Manikam and K. Y. Cheong, *IEEE Compon. Pack. Manuf. Technol.*, **1**(4), 457 (2011).
- [1.14] G. Zeng, S. McDonald, K. Nogita, *Microelectron. Reliab.*, **52**, 1306 (2012).
- [1.15] K. Sukanuma, S. J. Kim and K. S. Kim, *JOM J. Miner. Met. Mater. Soc.*, **61**, 64 (2009).
- [1.16] J. M. Song, H. Y. Chuang and T. X. Wen, *Metal. Mater. Trans. A.*, **38**,

1371 (2007).

[1.17] D. G. Ivey, *Micron*, **29** (4), 281 (1998).

[1.18] S. H. Mannan and M. P. Clode, *IEEE Trans. Adv. Pack.*, **27** (3), 508 (2004).

[1.19] L. Liu, M. Mirgizoudi, P. Zhang, L. Zhou, and C. Liu, In *Electronics System-Integration Technology Conference (ESTC)*, 1 (2014).

Chapter 2

Liquid Solder Interconnections & Diffusion Barrier Metallisations

This chapter contains a review of the liquid solder interconnections and the associated contact metallisations. The microstructural evolution characteristics of the intermetallics compounds (IMCs) formed between the liquid solder and substrate is discussed. The impact of the excessive IMC formation on the microstructural stability and joint reliability of the liquid solder interconnection is addressed. Finally, prevailing and advanced diffusion barrier metallisations are considered, with an overview on their IMC growth retarding efficacy.

2.1 Introduction

In the first chapter, the impact of harsh conditions on the interconnection reliability of electronics devices has been highlighted. A general trend for the development of solder joint materials is, therefore, to upgrade their high temperature properties and stability. For example, the melting point of the solder is elevated to retain mechanical strength at high temperatures. An alternative strategy has also been put forward, which utilises solder materials with a melting point below the typical operation temperatures of high temperature electronics. A salient advantage is that the regular solder re-melting during high temperature excursions can eliminate the damage accumulated during the solid state and hence any strain hardening or thermo-mechanical fatigue is unlikely. Moreover, large thermal expansion mismatch normally experienced in the multi-layer interconnection package can also be easily accommodated due to the liquid nature of solder joint not transferring any thermal residual stress [2.1]. However, for practical

implantation, there are several technical issues to be overcome, which include the selection of robust encapsulation materials, potential intermittent failures due to poor contact [2.2], and *inter alia*, the control over the excessive IMC formation between the molten Sn-based solder and the metallised substrate surface. The latter point places stringent requirements on a diffusion barrier layer at the solder-substrate interface, as the excessive growth of the hard and brittle IMCs can lead to brittle fracture of the solder joint.

The present work aims to develop a novel diffusion barrier material, by electrodepositing a Ni-Nb based coating on top of the Cu substrate, which not only prevents the overwhelming Sn-Cu IMC formation, but ensures good joint adhesion by permitting more controlled Ni-based IMC growth. Nb species are introduced into the Ni metal matrix, in an attempt to enhance the IMC-retarding efficacy. It is important that the Ni-Nb-based layer developed can meet the established benchmarks defined by prevailing barrier metallisations such as pure Ni and Ni-P. This chapter is, therefore, devoted to an overview of the liquid solder interconnections as well as the associated diffusion barrier metallisations. Two liquid solder systems are considered: Sn-In and Sn-Bi. The eutectic 52In-48Sn solder is employed in this study which merits discussion in detail; whilst the Sn-Bi is also incorporated in some cases for comparison. Only liquid-solid interfacial reaction is examined with respect to several prevailing and advanced barrier metallisations such as electrolytic pure Ni, electroless Ni-P and PVD³-sputtered Nb.

2.2 Liquid Solder Interconnections

Liquid solid interconnections refer to a specific electronic packaging paradigm for high temperature electronics, where the chip or chip carrier is attached to the printed wiring board (PWB) by means of liquid phase solder. As is illustrated in **Figure 2.1**, the mechanical integrity of the liquid solder is realised

³ PVD: Physical vapour deposition.

via thermally robust plastic underfill. The interfaces of the solder joint in contact with the chip and PWB are finished with diffusion barrier layers, respectively.

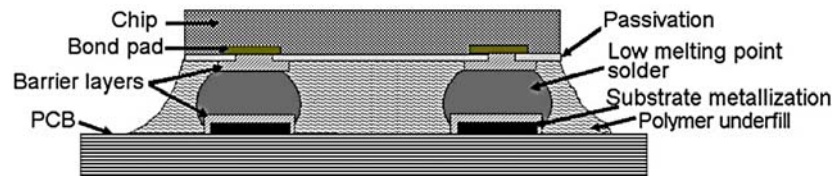


Figure 2.1 A schematic diagram illustrating an electronics assembly configuration utilising liquid solder interconnections [2.1]

Liquid solder candidates are normally at their eutectic compositions and hence possess a relatively low melting point, such as eutectic 52In-48Sn (T_m : 118°C) and eutectic 58Bi-42Sn (T_m : 138°C).

- Eutectic 52In-48Sn

Eutectic 52In-48Sn solder is evaluated for liquid solder interconnections, due to its low melting point (118°C), acceptable malleability, the ability of Sn to form bonds during solder reflow and good thermal-mechanical fatigue resistance [2.3]. In addition, the low solubility of Au in In-Sn solders can avoid the failures associated with gold embrittlement, suggesting good compatibility with Au-based metallisations [2.4]. The drawbacks, however, have been the high cost of the indium content.

- Eutectic 58Bi-42Sn

58Bi-42Sn solder, with a melting point of 138°C, is a more cost effective alternative to the In-Sn system. The volume change of the solder is negative upon melting, which may cause intermittent failures during mechanical vibrations. However, it has been demonstrated that the solder volume shrinkage could be circumvented by utilising off-eutectic compositions [2.1].

2.3 Interfacial Reactions between Liquid Solders and Metallisations

In electronic devices, the prevailing base materials (e.g. leadframes), coatings, and metallisations such as Cu, Ni, Ag and Au, tend to form IMCs with Sn, which is the major constituent of lead-free solders. It is key that a continuous and thin IMC layer can form at the interface, which gives rise to good metallurgical bonding. However, owing to their intrinsic brittle nature and susceptibility to create structural defects, too excessive an IMC layer tends to act as a strain concentrator and crack propagation pathway [2.5], taking a toll on the solder joint reliability. Therefore, knowledge and precise control of the specific interfacial reactions between various solder/substrate couples are crucial for establishing electronics reliability. This is particularly true for high temperature electronics, as elevated temperatures accelerate the interfacial IMC evolution, which are even exacerbated by temperature cycling and mechanical vibrations instigating creep and thermal mechanical fatigue, leading to premature joint failures.

The reaction between a liquid phase solder and its underlying metal substrate normally occurs during the initial solder reflow process, where the joint adhesion is established through the interfacial IMC formation. It is a paramount transient which defines the overall interconnection reliability, after which only a much slower solid-state reaction takes place. However, in the case of liquid solder joints, this liquid-solid reaction proceeds at times during high temperature excursions throughout the service life, which obviously complicates the interfacial microstructural evolution. There are two predominant strategies to limit the interfacial IMC growth: first, is to adjust the solder composition, by alloying with additional elements so as to affect the interfacial microstructural evolution; secondly, is to apply a diffusion barrier layer for prevention of direct inter-diffusion between those specific IMC-forming species across the interface. The former approach is exemplified by the addition of 1 wt.% Zn into eutectic 58Bi-42Sn liquid solder, giving rise to an

effective barrier of γ -Cu₅Zn₈ IMCs [2.1]; whilst the latter is evidenced by PVD-sputtered Nb metal layer which exhibits very slow and limited IMC growth with eutectic 52In-48Sn liquid solder [2.6].

The IMC growth for a common solid-solid interfacial reaction (between Sn-based solders and contact metallisations like Cu and Ni-P) is normally limited by bulk diffusion, yielding a parabolic kinetics profile. However, in the case of liquid-solid solder reaction, a reactive diffusion may simultaneously involve more than one interface process, such as solid dissolution, phase nucleation and growth, grain boundary and/or lattice diffusion in the IMCs. In the following, the liquid-solid interfacial reactions of several binary reaction couples are investigated based on the concept of microstructural and local equilibrium knowledge.

2.3.1 Liquid In-Sn with Cu

For liquid eutectic In-Sn solder reacting with pure Cu substrate at 200 and 300°C [2.7], the IMC formed at the Cu side (See **Figure 2.2**) exhibited an atomic composition of 75Cu-12In-13Sn, corresponding to ϵ -Cu₃(In_{0.48}Sn_{0.52}) phase, wherein Sn is partially substituted with In. The IMCs growing into the solder manifested themselves in irregular wedge-shaped geometry, possessing an approximate atomic composition of 56Cu-20In-24Sn, which is assignable to η -Cu₆(In_{0.46}Sn_{0.54})₅. Such a multi-layer structure resembles the characteristic IMCs consisting of a planar Cu₃Sn layer and scallop-shaped Cu₆Sn₅, as experienced in most Sn-based solder(l)/Cu(s) diffusion couples (e.g. Sn/Cu [2.8], Sn-Pb/Cu [2.9], Sn-Bi/Cu [2.10] and Sn-Ag/Cu [2.11]). Based on thermodynamic-kinetics approach, the activation energy for the scallop-shaped, η -intermetallic growth is calculated as ca. 30 kJ/mol., comparable to that for the diffusion of Cu in liquid solder (19.5 kJ/mol.). This implies that the η -intermetallic growth is diffusion-controlled. The activation energy for the development of planar, ϵ -intermetallic is calculated to be 186

kJ/mol. , consistent with the lattice diffusion of either Sn or In in Cu [2.7]. These suggest that the ϵ -intermetallic growth is controlled by the diffusion of Sn and In in the IMC structure.

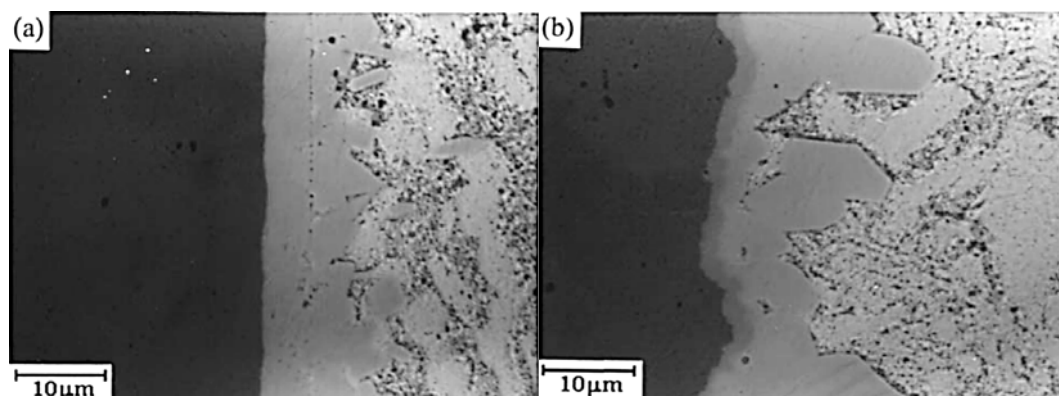


Figure 2.2 SEM images showing the representative morphology of IMCs at eutectic In-Sn(l)/Cu(s) interface after soldering reactions at various temperatures for 120 min: a) 200°C and b) 300°C [2.7].

2.3.2 Liquid In-Sn with Pure Ni

For the eutectic In-Sn(l)/Ni reaction couple, the representative morphology of the IMCs formed at 250 and 400°C (See **Figure 2.3** [2.4]) comprises a continuous intermetallic layer at the Ni side and irregular, polyhedral and discrete IMCs growing into the solder. It is noteworthy that some of the latter IMCs have detached from the substrate/solder interface and migrated into the bulk solder. Upon interdiffusion and IMC growth, the rearward movement of the original Ni substrate surface takes place simultaneously with the onward growth of polyhedral IMCs. It is interesting to note that, despite different formation mechanisms and geometries, these two types of IMCs seem to share a similar atomic composition at 33Ni-20In-47Sn. Wang, Tseng and Chuang [2.4] preliminarily precluded the possibility of a binary $\text{Ni}(\text{In}_{0.3}\text{Sn}_{0.7})_2$ phase, as neither NiIn_2 nor NiSn_2 exists in the respective Ni-In (**Figure 2.4**) [2.12] and Ni-Sn (**Figure 2.5**) [2.13] binary equilibrium phase diagrams. These authors further postulated, based on X-ray diffraction (XRD) crystallographic data, that 33Ni-20In-47Sn is possibly a less-known ternary phase, which

showed a distinct XRD pattern compared to several suspected candidates with comparable compositions such as Ni_2In_3 and $\text{Ni}_{28}\text{In}_{72}$. The growth kinetics of the ternary IMCs gave a parabolic relation, signifying that the reaction was diffusion-controlled. The activation energy for the IMC growth is calculated to be 56.57 kJ/mol., which is almost a doubling of that for the scallop-shaped η -intermetallic formed in the aforementioned In-Sn(l)/Cu reaction couple. That explains why pure Ni demonstrated appreciably slower growth kinetics for IMCs into the liquid eutectic In-Sn solder as compared to pure Cu.

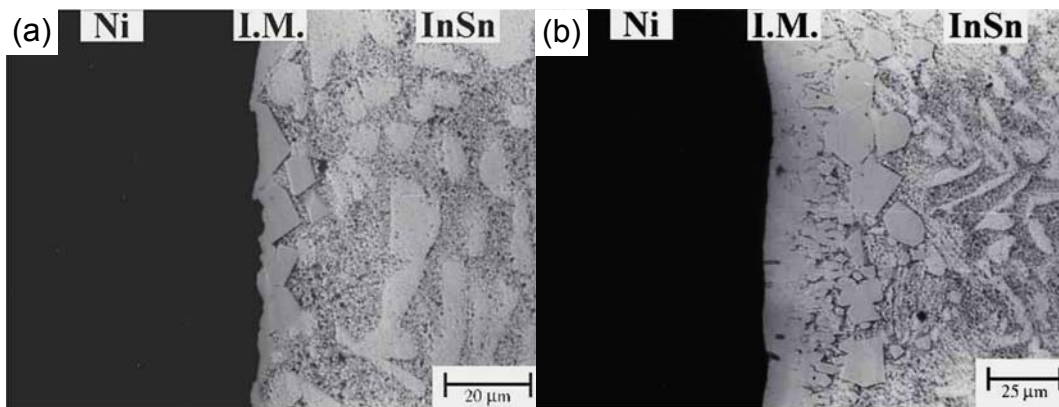


Figure 2.3 SEM images showing the representative morphology of IMCs at eutectic In-Sn(l)/Ni(s) interface after soldering reactions at various temperatures for 240 min: a) 250°C and b) 400°C [2.4].

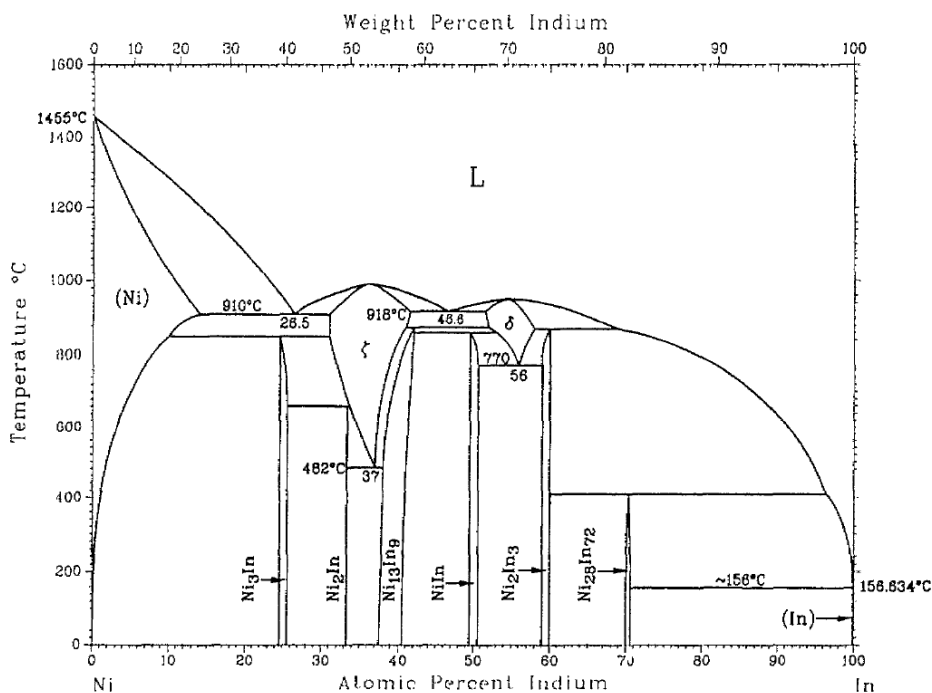


Figure 2.4 Ni-In phase diagram from Ref. [2.12].

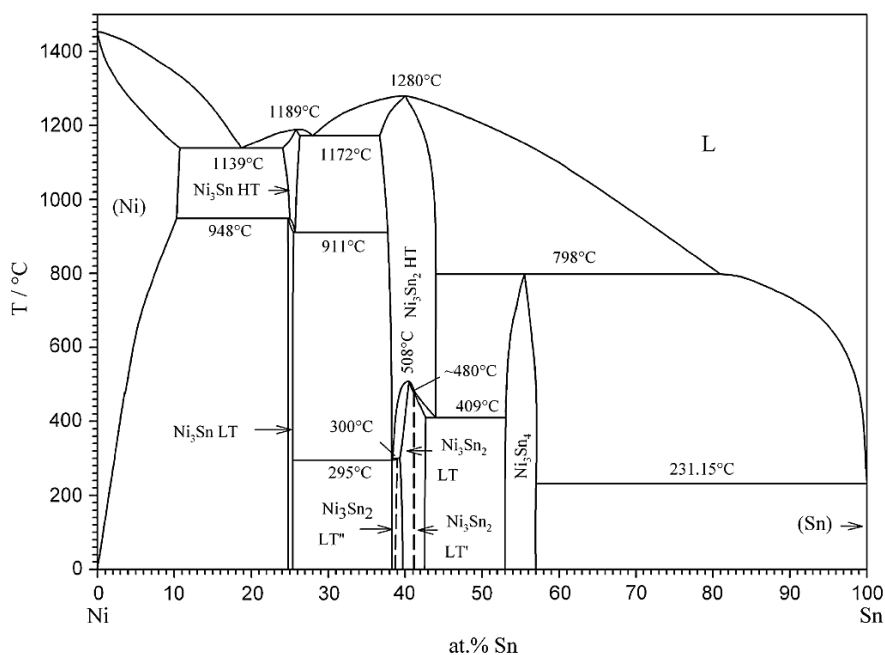


Figure 2.5 Ni-Sn phase diagram from Ref. [2.13].

2.3.3 Liquid In-Sn with Ni-based Variants

As mentioned above, the pure Ni metallisation did exhibit some efficacy in retarding the In-Sn-based IMC growth. It is, therefore, of great interest to look into the applicability of those Ni-based variants as a diffusion barrier material against the liquid solder. Unfortunately, only a limited number of the Ni-based

metallisations has been explored thus far. Here two cases are discussed: electroless Ni-Cu-P and electroless Ni-W-P.

- *Electroless Ni-Cu-P*

Electroless Ni deposition is a well-established process for depositing Ni-based thin films. The deposition relies on a reducing agent (e.g. hydrated sodium hypophosphite ($\text{NaPO}_2\text{H}_2\cdot\text{H}_2\text{O}$)), to chemically reduce Ni(II) ions into the metallic form. A certain fraction of P content is also co-deposited, which arises from the reducing agent. Electroless Ni deposition has the advantages of good selectivity, excellent throwing power and the ability to deposit onto electrical non-conductors with appropriate pre-treatment. As an emerging derivative of the electroless Ni-P coatings, Ni-Cu-P has exhibited excellent wetting property and proved an effective barrier for solder bump application [2.14]. Its applicability to the liquid solder interconnection has been, therefore, investigated by Chen and Lin [2.15]. These authors reported that, the IMCs formed between amorphous 67.2Ni-29.4Cu-3.4P (wt.%) deposits and both 52In-48Sn and 20In-80Sn solders at 250 - 300°C took the appearance of cuboids, which were then assigned to In_3Ni_2 and $\text{Ni}_{28}\text{In}_{72}$ phases in light of XRD measurements. Also, the partial substitution between In and Sn was also true in these IMCs according to Auger electron spectroscopy (AES) analysis. For 20In-80Sn, a small fraction of Ni_3Sn_4 compound was also present, which was not found in the eutectic counterpart. This is consistent with a general fact that, indium, when available, tends to be the predominant species to form IMCs with Ni in preference to Sn. It is interesting to note that, 29.4 wt.% of the Cu content in the electroless coating did not seem to form any significant IMC phase with Sn based on XRD analysis. This points to the possible presence of a Cu-depleted zone at the solder/deposit interface. Unfortunately, a detailed cross-sectional compositional profiling of the interfacial region was not provided by the authors, nor was an analysis on the IMC growth kinetics.

- *Electroless Ni-W-P*

Both electroless Ni-P [2.16] and Ni-W-P [2.17] have been investigated as diffusion barrier materials for liquid solder joint assemblies, although the liquid solder of interest was eutectic 42Sn-58Bi instead of the In-Sn system. Ni-P barrier has proven inadequate [2.16] against liquid Bi-Sn solder ingress during high temperature storage experiments. This could be partially attributed to the presence of highly scattered micro-cracks spanning the Ni-P deposits, which act as a straightforward pathway for the migration of liquid solder. These micro-cracks are believed to originate from the residual tensile stress generated from the electroless deposition process. In an attempt to improve the performance of Ni-P-based barrier coating, tungsten (W) has been co-deposited [2.17]. Generally, Ni-W-P with sufficient thickness ($> 5 \mu\text{m}$) has been found to possess enhanced barrier lifetime compared to the normal Ni-P counterpart. The IMC products resulted from interfacial reaction between eutectic Bi-Sn solder and amorphous 80Ni-12W-8P (wt.%) at 200°C consisted of planar $(\text{Ni,W})_3\text{P}$ phase formed at the barrier layer side and discrete, wedge-shaped Ni_3Sn_4 crystals growing into the solder. W content was generally found to be enriched in the $(\text{Ni,W})_3\text{P}$ phase, which is thought to be responsible for the enhanced barrier performance of the Ni-W-P deposits.

2.3.4 Liquid In-Sn with Pure Nb

Mannan and his co-workers [2.6] have evaluated a range of substrate metallisations in terms of their potentials to furnish good adhesion strength and stability against molten In-Sn solder ingress. These barrier candidates are Ni, Cr, Ti, Pt, V, Nb, Ta and W, amongst which only Nb and Ta exhibited slow and limited IMC growth in the presence of liquid-phase solder. Amongst the two refractory elements, only PVD-sputtered Nb exhibited strong adhesion with the solder and hence was deemed as a promising barrier metallisation candidate for high temperature liquid interconnects. It should be noted that, Nb metal cannot be electrodeposited alone from aqueous solutions, which significantly

limited the application of Nb barrier layers in electronics packaging industry. It is of great interest to use an alternative approach, for example, electrodeposition, to reproduce Nb-based thin films, which is more cost effective and more compatible with other micro-fabrication steps.

The interfacial reaction between the molten In-Sn solder and pure Nb layer proceeds in an unusually controlled and self-limiting fashion [2.6, 2.18, 2.19]. The predominant IMC species is NbSn_2 , in the form of thin, hexagonal platelets (See **Figure 2.6**), whilst indium plays a passive role in the IMC formation. The crystal size of the NbSn_2 IMCs has been measured over a temperature range from 192 to 260°C for various periods. It was observed that there is an incubation period for the IMC nucleation. The temperature dependence of the incubation is noteworthy; with elevating temperature, a reduction of two orders of magnitude is observed, from 500 hours at 192°C to merely 5 hours at 260°C. A typical kinetics profile of the IMC growth is described in **Figure 2.7**. It begins with a rapid and short growth stage, which thereafter declines to a much lower rate. It is believed that such a self-limiting IMC formation is presumably due to a slow diffusion of Nb atoms through the molten solder as well as through the NbSn_2 crystal platelets.

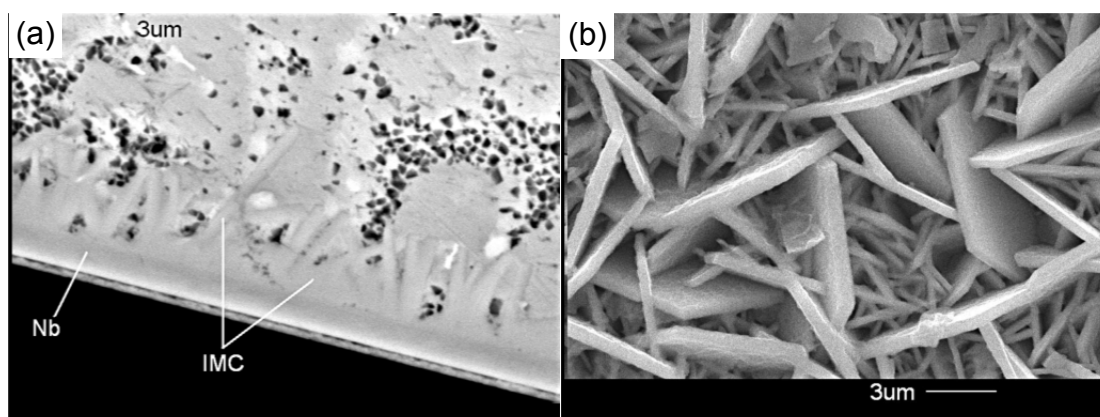


Figure 2.6 SEM images showing the representative morphology of IMCs at eutectic In-Sn(l)/Nb(s) interface after soldering reactions at 192 °C for 5 months: a) cross-sectional view and b) top view [2.18].

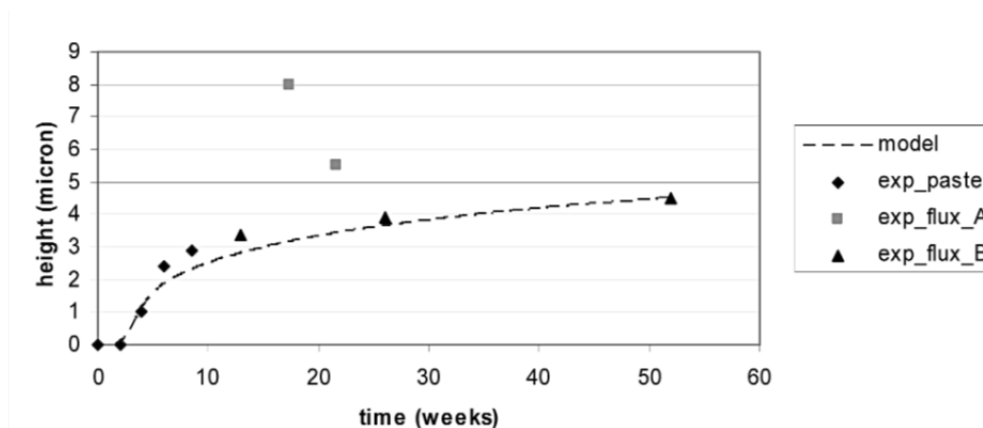


Figure 2.7 A plot presenting the variation of IMC growth thickness with time for In-Sn(l)/Nb(s) reaction couple at 192 °C [2.18]

2.4 Summary

In this chapter, the materials and process for implementing high temperature liquid interconnects are introduced. Stringent requirements on an adequate diffusion barrier layer for the prevention of excessive IMC evolution at the liquid solder/solid substrate interface have been addressed. Prevailing and advanced contact metallisations, such as pure Cu, pure Ni, electroless Ni-P and derivatives, as well as pure Nb, are reviewed with respect to liquid In-Sn solders and, in some cases, liquid Bi-Sn solders. The long-term, interfacial microstructural evolution characteristics of these metallisations in contact with the molten solder are described. Amongst them, PVD sputtered pure Nb metal layer has proved adequate as a barrier materials which exhibits slow and limited IMC growth and also permits good joint adhesion. There is a continued interest to reproduce Nb-based metal layer using alternative methods (e.g. electrodeposition), which is more cost effective and compatible with other micro-fabrication steps.

2.5 References

- [2.1] J. F. Li, S. H. Mannan, M. P. Clode, D. C. Whalley and D. A. Hutt, *Acta Mater.*, **54** (11), 2907 (2006).
- [2.2] F. P. McCluskey, M. Dash, Z. Wang and D. Huff, *Microelectron. Reliab.*, **46** (9), 1910 (2006).
- [2.3] I. Shohji, S. Fujiwara, S. Kiyono, and K. F. Kobayashi, *Script. Mater.*, **40** (7), 815 (1999).
- [2.4] S. S. Wang, Y. H. Tseng and T. H. Chuang, *J. Electron. Mater.*, **35** (1), 165 (2006).
- [2.5] T. Laurila, V. Vuorinen and J. K. Kivilahti, *Mater. Sci. Eng. R: Reports*, **49** (1), 1 (2005).
- [2.6] S. H. Mannan and M. P. Clode, *IEEE Trans. Adv. Pack.*, **27** (3), 508 (2004).
- [2.7] T. H. Chuang, C. L. Yu, S. Y. Chang and S. S. Wang, *J. Electron. Mater.*, **31** (6), 640 (2002).
- [2.8] K. N. Tu and R. D. Thompson, *Acta Metall.*, **30**, 947 (1982).
- [2.9] C. Y. Liu, K. N. Tu, T. T. Sheng, C. H. Tung, D. R. Frear and P. Elenius, *J. Appl. Phys.*, **87**, 750 (2000).
- [2.10] P. T. Vianco, A. C. Kilgo and R. Grant, *J. Electron. Mater.*, **24**, 1493 (1995).
- [2.11] W. Yang and R. W. Messler, *J. Electron. Mater.*, **23**, 765, (1994).
- [2.12] T. B. Massalski, *Binary Alloys Phase Diagram*, 2nd edition, ASM International, Ohio, **3**, 2267 (1990).
- [2.13] C. Schmetterer, H. Flandorfer, K. W. Richter, U. Saeed, M. Kauffman, P. Roussel, and H. Ipser, *Intermetallics*, **15** (7), 869 (2007).
- [2.14] C. Y. Lee and K. L. Lin, *Thin Solid Films*, **239** (1), 93 (1994).
- [2.15] C. J. Chen, and K. L. Lin, *IEEE Trans. Compon. Pack. Manuf. Technol. Part B: Adv. Pack.*, **20** (3), 211 (1997).
- [2.16] J. F. Li, S. H. Mannan, M. P. Clode, C. Liu, K. Chen, D. C. Whalley and P. P. Conway, *IEEE Trans. Compon. Pack. Technol.*, **31** (3), 574 (2008).

[2.17] K. Chen, C. Liu, D. C. Whalley, D. A. Hutt, J. F. Li and S. H. Mannan, In *IEEE Electronics System Integration Technology Conference*, 1st, **1**, 421 (2006).

[2.18] S. H. Mannan, M. P. Clode and M. Dagher, *J. Electron. Mater.*, **34** (2), 125 (2005).

[2.19] J. F. Li, S. H. Mannan, M. P. Clode, C. Johnston and A. Crossley, *Acta Materialia*, **55** (15), 5057 (2007).

Chapter 3

Niobium Electrodeposition

The previous chapter highlights a need to produce Nb metal coatings utilising an approach that is cost effective and also compatible with other microfabrication steps. The present chapter is concerned with a promising solution, electrodeposition. It begins with an introduction to the properties of Nb metal and the related oxides. This is followed by a general description of the principles of electrodeposition, where the electrochemistry of refractory elements like Nb and a variety of electrolyte candidates are reviewed. Finally, the challenges associated with the electrochemical reduction of Nb species are discussed, whereby possible deposition promoting strategies such as induced co-deposition are addressed.

3.1 Introduction to Niobium Metal and Oxides

Niobium (Nb), or by its original given name, columbium, is a Group V transition metal element with an atomic number of 41. It belongs to the family of refractory metals, which generally exhibit excellent resistance to heat, wear and corrosion. The exceptional thermal stability of Nb is attributed to its high melting point, 2468°C [3.1], below which it retains a simple body centred cubic structure without any allotropes. The excellent corrosion resistance arises from the formation of a tenacious oxide layer (Nb_2O_5) on the metal surface [3.2]. Some important physical properties of Nb are summarised in **Table 3.1**. Nb has found major consumption in the steel sector, where it is added in small amounts into stainless steels to improve their welding behaviour and heat resistance [3.1]. It falls in the category of metals of strategic importance, as Nb has been employed as a constituent in superalloys for gas turbines and rocket

sub-assemblies. Other applications of Nb include in catalysts, super conduction and electronics, to name a few. Due to the cost and high impurity level when produced using conventional thermometallurgical approaches, Nb is normally utilised not in the bulk state but as metal finishes, where coatings with thickness of tens of microns [3.2] on common substrates like stainless steel possess surface properties similar to those of the bulk material. The negative deposition potential of Nb, however, precludes the possibility of electrodeposition from conventional aqueous systems. Limited success has been achieved utilising alternative electrolytes such as high temperature molten salts [3.3], and less commonly, molecular organic solvents [3.4], which require either extremely high temperatures ($> 500^{\circ}\text{C}$) or handling of explosive vapours. These render the established methods not applicable to metal finishing for electronics packaging. Nevertheless, the recent introduction of ionic liquid electrolytes combining both non-aqueous features and low operational temperatures has led to a resumption in the interest of Nb electrodeposition.

Atomic number	41
Atomic weight (AMU)	92.926
Atomic radius (nm)	0.147
Crystal structure	Body centred cubic (BCC)
Lattice constant at 0°C (nm)	0.33004
Density at 20°C (g/cm^3)	8.57
Melting point ($^{\circ}\text{C}$)	2468
Boiling point ($^{\circ}\text{C}$)	4927
Thermal conductivity at 0°C (W/mK)	52.3
Electrical conductivity at 18°C (%IACS by volume)	13.2

Table 3.1 Important physical properties of niobium [3.1]

A variety of Nb oxides also merit discussions in the context of Nb electrodeposition. This is due to the tendency of Nb to form oxides when being electrochemically reduced [3.3]. The electronic configuration of Nb is $[\text{Kr}] 4d^4 5s^1$. The distribution of 5 electrons in two outer incomplete shells dictates that the most stable valence is + 5. Therefore, niobium pentoxide (Nb_2O_5) is the most stable niobium oxide compound. Other stable oxides are also known, such as NbO (+2) and NbO_2 (+4). It is the high affinity of Nb towards O and the existence of various stable niobium sub-oxides that complicate the electrochemical reduction routes of Nb species. The reduction products are often associated with O and hence are in adherent and not compact [3.3]. Nb_2O_5 exhibits high relative permittivity, making it an attractive dielectric material for high capacity solid electrolyte capacitors [3.5]. It also shows good selectivity, stability and catalytic activity: a combination of Ni metal and Nb_2O_5 gives rise to a strong metal-support interaction (SMSI) [3.6, 3.7]. With decreasing oxidation number, the niobium oxides exhibit increasing metallic characteristics. NbO_2 behaves as a semiconductor whilst NbO shows metallic conducting behaviour [3.8].

3.2 General Principles of Electrodeposition

Electrodeposition has been practiced for more than 150 years. Indeed for many years, most of the progress made in the field has come from empirical and ingenious trial-and-error approaches, with the underlying scientific aspects not always understood. This, however, has changed due to the increased awareness that a profound knowledge of electrochemistry is vital to the advancement of electrodeposition as a modern manufacturing approach [3.9, 3.10].

With the continuous trend towards miniaturisation, integration and cost competitiveness in the electronics industry, the predominance of the electrodeposition method has ever increased. It can be readily appreciated by,

for example, the overwhelming replacement of vacuum deposited Al with electroplated Cu for chip metallisation in 1997 [3.11]. Electrodeposition conveys a number of advantages, which include:

- Relatively low processing temperatures;
- Precise control over appearance, thickness, composition and microstructure of the deposits can be achieved [3.10];
- Good throwing power (cf. PVD);
- Good deposition selectivity so that complex geometry can be achieved;
- Cost effectiveness.

These attributes allow the microelectronic devices made to be more sophisticated in geometry, smaller in dimensions and at reduced cost.

Electrodeposition may be defined as an electrochemical process of producing films or coatings upon a conductive surface through the application of electric current [3.12]. At least four major components are necessitated to realise an electroplating cell, which are cathode, anode, electrolyte and external electric circuit. A representative cell configuration is illustrated in **Figure 3.1**. For metal electrodeposition, the substrate onto which metal is deposited, viz. cathode, is immersed in the electrolyte opposite to a counter electrode (anode) where the oxidation reaction takes place. The electrode reactions are driven by an external electric current supplied by a power source. At the cathodic side, the metal ions (M^{n+}) in the electrolyte are electrochemically reduced into the metallic form following reaction represented by **Equation 3-1**. The mass transport of metal ions within the electrolyte is realised, normally by the simultaneous effect of diffusion, electrolyte convection and electro-migration [3.10]. At the anodic side, for the simple case of an insoluble anode, the oxidation reactions proceed to balance the current flow, represented by **Equations 3-2 & 3-3**, which stand for acidic and alkaline solutions,

respectively. It is noteworthy that for non-aqueous electrodeposition where the electrochemistry is not limited by water decomposition, the anodic process may manifest itself either in decomposition of the electrolyte components or in anodic dissolution of the anode material.

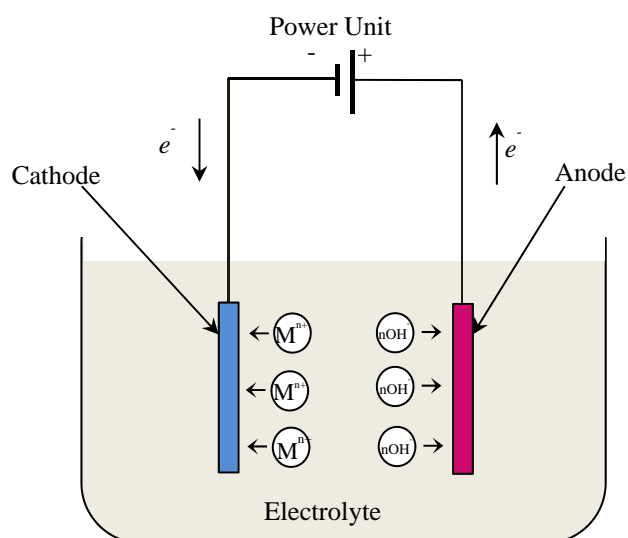
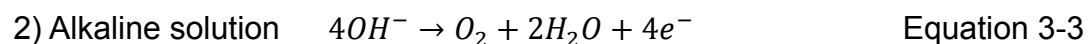
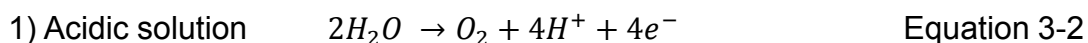


Figure 3.1 A schematic diagram illustrating a representative electroplating cell set-up

Cathodic reaction:



Anodic reaction:



There are several issues in need of emphasis when describing an electrodeposition process. These are cathodic current efficiency and overpotentials, which will be briefly introduced in the following.

3.2.1 Cathodic Current Efficiency

Based on Faraday's 1st Law of Electrolysis [3.13], the change in the mass of an electrode is directly proportional to the quantity of the electrical charge passed at the electrode. The theoretical mass-charge ratio of an electrodeposition process can be described as in **Equation 3.4**.

$$\text{Theo } \frac{\delta m}{\delta Q} = \frac{M}{nF} \quad \text{Equation 3-4}$$

Where $\text{Theo } \frac{\delta m}{\delta Q}$ denotes the theoretical mass-charge ratio, M is the relative molecular mass, n is the number of electrons transferred in the electrochemical reaction and F represents Faraday's constant. The cathodic current efficiency (CCE), also termed the Faradic efficiency (FE), is the fraction of the total electric charge passage at the cathode to deposit metal(s), which can be described as in **Equation 3.5**.

$$\text{Cathodic current efficiency} = \frac{\text{Exp } \frac{\delta m}{\delta Q}}{\text{Theo } \frac{\delta m}{\delta Q}} \times 100\% \quad \text{Equation 3-5}$$

Where $\text{Exp } \frac{\delta m}{\delta Q}$ represents the experimental mass-charge ratio. In fact for most electrodeposition of practical interest, the CCE can hardly reach 100% owing to the presence of side cathodic processes. Taking hard chromium electroplating as an example where acidic baths (e.g. pH=0) are typically employed, hydrogen evolution takes place competing with chromium deposition, following reactions simplified by **Equation 3-6**.



This reaction not only decelerates the deposition kinetics and increases energy consumption, but also may result in hydrogen embrittlement, where the incorporation of the adsorbed hydrogen atoms into the growing electrodeposit

or even into the substrate materials (e.g. high alloy steels) induces reduced ductility and non-ductile fracture mode [3.14]. To partially mitigate hydrogen evolution for aqueous systems, one can adjust the bath acidity by adding base (e.g. NaOH or NH_4OH) into the solution. In cases where hydrogen evolution is totally undesirable, alkaline electrolytes can be utilised, e.g. alkaline zincate solutions are employed for the galvanising of steel components to circumvent the hydrogen embrittlement.

3.2.2 Cathodic Overpotential

For electrodeposition, cathodic overpotential describes a phenomenon when the energy (or voltage) required to drive the electrodeposition exceeds that is expected by the thermodynamic equilibrium. An increase in the cathodic overpotential obviously leads to a reduction in the deposition kinetics. However, it is often desirable for metal electrodeposition, since elevated cathodic overpotential generally encourages grain nucleation rather than growing existing grains, forming fine-grained structures and hence giving rise to deposits with enhanced brightness, smoothness and uniformity.

There are three major overpotentials, which are ohmic resistance overpotential, charge transfer overpotential and concentration overpotential [3.15].

- Ohmic resistance overpotential

The ohmic resistance overpotential is directly related to the specific resistivity of the electrolyte and the configuration of cathode and anode. When it is the dominant overpotential, e.g. in non-aqueous organic solvents which exhibit low electrical conductivities, the deposition is deemed to proceed under conditions of primary current distribution (PCD). However, the PCD often leads to non-uniform current distribution upon the cathode, resulting in non-uniform deposit thickness and, for alloy and composite deposition, compositional non-uniformity as well.

- Charge transfer overpotential

Charge transfer overpotential, also called activation overpotential, is determined by the Faradaic reaction taking place at the electrode. When it is the dominant overpotential, the reaction is said to be activation controlled and governed by the secondary current distribution (SCD). SCD generally leads to macroscopically uniform deposits. An effective strategy to increase charge transfer overpotential, is to introduce a complexing agent, where relatively simple metal ions are complexed with bulky groups such as cyanide (-CN), and organic poly-acid (such as citrates and oxalates) ligands, whereby the metal species become more difficult to be electrochemically reduced.

- Concentration overpotential

The third factor affecting the electrodeposition is mass transport, or diffusion. The concentration overpotential results from the depletion of electrochemically active species in the diffusion layer⁴ at the cathode surface. The concentration overpotential can be reduced by increasing convection of the electrolyte (i.e. by applying solution agitation) [3.15].

To summarise, for production of uniform and smooth deposits, it is often necessary to convert the PCD to SCD (and/or to increase charge transfer overpotential), e.g. by reducing the electrolyte resistivity, providing effective cathode-anode configuration, furnishing adequate electrolyte agitation and also by introducing a complexing agent when possible.

3.3 Electrodeposition Electrolytes

The electrodeposition of reactive refractive elements like niobium (Nb) cannot be achieved from conventional aqueous solutions due to the relatively negative deposition potentials. High temperature molten salts are historically

⁴ Diffusion layer: When electrode process occurs, there is a zone close to the electrode surface where the concentrations of electrochemically active species differ from that of the bulk solution. The zone is called diffusion layer.

exploited to circumvent this problem since they are aprotic ionic media, precluding any competing hydrogen evolution process such as hydrogen embrittlement and limited current efficiency, however, the high operating temperature, frequently over 800 °C, is notoriously problematic in terms of safety issues due to the flammability and volatility and possible thermal damage (*inter alia*, corrosion) to the substrate [3.16]. Ionic liquids, as an alternative, have been investigated in the hope of resembling the electrolyte characteristics that molten inorganic salts exhibit for the electrodeposition of refractory elements. However, a high temperature (usually 200-300°C) is still generally a prerequisite, which is due either to a high melting point of the ionic liquid or to a kinetic hindrance in the formation of the metal element at relatively low temperature [3.17, 3.18].

3.3.1 Aqueous electrolytes

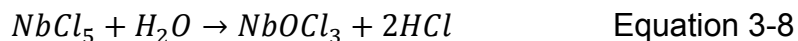
Despite the inability of aqueous electrolytes to deposit metallic Nb, numerous attempts have been made to understand the electrochemical reduction behaviour of Nb species within them. The electrolytes have mostly been based on strong inorganic acids, such as H₂SO₄ [3.19], HNO₃ [3.20] and concentrated HCl [3.21]. It was widely realised that, Nb(V) cannot be reduced to Nb(0). Instead, the reduction usually terminates at Nb(IV) (-0.455 V vs. SCE⁵ [3.21]) or Nb(III) (-0.83 V vs. SCE [3.20]). The reduction routes have been reiterated to be complex and stepwise, where a reversible disproportionation reaction is often noted (See **Equation 3-7**).



This reaction is thought to prevent Nb(IV) species from further reduction to Nb(II). However, it was observed that the complexing of Nb(IV) with ethylene glycol merits the possibility of reduction to Nb(II) [3.21]. In addition, the hydrolysis of Nb halide precursors (See **Equation 3-8**) plays an important role

⁵ SCE: Saturated calomel electrode.

in the reduction mechanisms, which will be treated in details in the following sections.



3.3.2 High Temperature Molten Salts

High temperature molten salts, specifically alkali metal fluorides, have historically been an enabling electrolyte category for the electrodeposition of reactive metal elements due to their large electrochemical windows. The electrodeposition process of refractory metals using such electrolytes is generally governed by mass transport, which renders the electrochemical crystal growth more susceptible to dendritic development and thus lowered the effective current efficiency. Moreover, the excessively high temperature conditions [3.3] often instigate the simultaneous dissolution of metal being deposited and caused thermal corrosion problems.

The electrodeposition of coherent coatings of refractory metals from fused salt solution has been pioneered by Senderoff and Mellors [3.3, 3.22 & 3.23], who developed a general process applicable to a wide range of refractory elements including Nb, Ta, Zr, Hf, V, Mo, Cr and W. The bath formulation consists of a eutectic mixture of alkali metal fluorides (e.g. ternary KF-LiF-NaF and binary KF-NaF or KF-LiF) as the solution and potassium fluo-metallates (e.g. K_2NbF_7 for Nb) as the metallic cation source. In the case of Nb, a treatment suggested and generally accepted by their successors, was to electrochemically reduce Nb (V) to Nb (IV) prior to electrodeposition and as such to increase the current efficiency of Nb reduction from 0% to 100% [3.3]. A possible explanation is that the presence of Nb (V) species, which are strong oxidising agents *per se*, would reoxidise the subvalent Nb reduction intermediates, thereby negating further reduction [3.3, 3.25].

The choice of current density was reported to be critical, where its lower limit is governed by the need to minimise co-deposition of noble impurity present in the solution, the upper limit generally increases with Nb content in the bath and operational temperature and is restricted by the diffusion (above the upper limit alkali metal would be poorly co-deposited) [3.3]. The coherence of the resultant Nb deposits was proven to arise from the formation of true electroplates instead of diffusion alloys (i.e. Nb reacts with the metal of the substrate to give an intermetallic compound and results in good coherence). These authors also pointed out that the quality of the Nb deposits can be significantly degraded by the presence of chlorides, oxy-salts and hydroxides in electrolytes. These phenomena have been generally attributed to the formation of chloride or oxofluoride complexes which perturb the normal Nb reduction.

Nb electrodeposition from alkali metal halide baths was found to be limited by diffusion of the electrolyte, the formation of a dendritic or spongy structure is not surprising. As dendritic formation is usually attributed to the depletion of metal ions at the cathode surface arising from prolonged concentration polarisation, one can periodically interrupt the current (i.e. pulse current electrodeposition) so as to remove the completion of the polarisation.

3.3.3 Ionic Liquids

3.3.3.1 Introduction

Over the last five decades, ionic liquids (ILs), known as a group of molten salts with very low melting points (below 100°C), have been progressively developed [3.25, 3.26]. As one of the major driving forces, their application as media for metal electrodeposition has received a considerable amount of interest [3.25-3.34] owing to their wide electrochemical window (cf. conventional aqueous electrolyte), negligible vapour pressure and inflammability (cf. molecular organic solvents) and low operational temperature

(cf. high temperature inorganic molten salts).

Ionic liquids are composed of cations and anions and hence are electrically conductive. A huge number of cation and anion candidates exist that allow for the 'fine-tuning' of ionic liquid's physicochemical, electrochemical and toxicological properties. Perhaps one of the most important characteristics of ionic liquids, that is of significant relevance to metal electrodeposition, is their large potential window (sometimes > 7V) which gives the possibility of depositing reactive metals such as refractory elements which are impossible to electrodeposit from aqueous electrolytes. Ionic liquids based on a wide range of transition and main group metals have been formulated, some of which have been successfully applied to metal electrodeposition (e.g. Al, Sn, Ni, Cu and Ag [3.27-3.34]), although quite a few have come to practical application due mainly to economic factors [3.26]. The previous research has been extended to the collection of physical and electrochemical data of ILs (e.g. viscosity, conductivity and potential windows), to the study of mass transport mechanisms during electrodeposition and their implications on the microstructure of electrodeposits, and to explore the possibility for electrodeposition of novel metals (i.e. reactive elements such as Al, Ti and Ta). It has been clearly established that, there is a paradigm change in the metal speciation and mass transport mechanisms in ILs when compared to conventional aqueous systems.

3.3.3.2 Classifications

Ionic liquids can be divided into two types based on the choice of anions, i.e. those with complexed anions and those with discrete anions. The reduction in the melting point which makes an ionic liquid so useful is attributed to a charge delocalisation mechanism, either by anionic complexation or by the shielding of bulky side groups. The first complexed anion IL that has been extensively studied [3.25] is based on chloroaluminate $[AlCl_4]^-$, which is a binary mixture of

a halide (either organic or inorganic) and AlCl_3 . AlCl_3 is a Lewis acid which accepts Cl ions to form the negatively charged Al complex $[\text{AlCl}_4]^-$. It has been said [3.29] that the Lewis acidity of this type of IL can be tuned by varying the eutectic composition, whereby a wide range of metals and alloys were found to be electrodeposited from this IL within a certain Lewis acidity range, which include Nb-Al alloys [3.35]. The major drawback of these ionic liquids, arising from the extreme moisture sensitivity, restricts their practical fruition. Other chloro-metallate systems (based on Zn, Sn and Fe) have also been formulated, which, together with the $[\text{AlCl}_4]^-$ based, have been classified as the Eutectic Type I of complexed anion ILs. Based on this strategy, Eutectic Type II and III have also been developed, which essentially replace the anhydrous metal chloride for the Type I with hydrated metal chlorides (e.g. Cr, Cu, Ni and Co) and with a hydrogen bond donor (HBD) (e.g. urea and ethylene glycol), respectively.

The discrete anion IL is generally based on anions like $[\text{BF}_4]^-$, $[\text{PF}_6]^-$, and more hydrophobic ones like $[\text{TFSA}]^-$ and $[\text{FAP}]^-$. The properties of ionic liquids that are generally governed by anions are listed as follows,

- Chemical reactivity (water reactivity);
- Hydrophobicity;
- Stability;
- Conductivity and viscosity depending on cation-anion pair interaction;
- Coordination geometry (around the metal ion), potential window and hence reduction process.

The choice of cation is also essential to the properties of ILs, where imidazolium-based and pyrrolidinium-based ones are commonly used. During metal electrodeposition, cations would have to be adsorbed to the cathode surface with the opposite charge and hence the double layer structure would depend on the cation. It is actually the cation-anion pair interaction that

determines the physical properties of ILs such as conductivity, viscosity, polarity, the dissolving capability of metal salts and density.

3.3.3.3 Potential windows

The potential window of an electrolyte solution defines the potential range in which the electrolyte is electrochemically stable towards a particular working electrode, as is bounded by a cathodic limit below which the reductive decomposition of the electrolyte takes place as well as an anodic limit above which the oxidative breakdown occurs. Unlike common aqueous systems whose potential limits are governed by water decomposition (potential window: 2.06 V vs. normal hydrogen electrode (NHE)) [3.36], the ionic components of ILs are generally more chemically robust and hence give rise to larger potential windows (ca. 3.5 to 5 V). A large potential window for the electroplating bath, especially a notably negative cathodic limiting potential, is favourable from a viewpoint of metal electrodeposition.

The determination of the electrochemical window is usually achieved through linear sweep voltammetry (LSV) or cyclic voltammetry (CV), the former of which involves one single anodic or cathodic sweep where current density at the working electrode is measured as a function of the applied potential, whilst for the CV the applied potential is reversed as it ramps up to a set potential value. LSV measurement can always extract voltammetric information from freshly made solution but its reproducibility has to be individually examined. For the case of CV, it is more likely to provide a direct indication of reproducibility; however, due to its multi-cycle nature, the voltammograms of the reverse sweeps are susceptible to influences of the electrochemical reaction products stemming from the previous sweep(s).

The magnitude of the potential window is governed by a range of measurement conditions, which not only decisively include the chemical nature

of the test solution, but also involve electrode materials, potential scan rate, impurities and temperature. It is not easy to compare the data in the literature due to the lack of a unified testing methodology (which practically may not even be possible), and, in the context of ILs, that is further complicated by the use of various reference electrodes [3.37].

The correlation between reduction potentials and the coordination of anions to the metal has been preliminarily established [3.38]. In Eutectic Type II systems, metals with similar coordination chemistry, e.g. Zn(II) and Pb(II), may well maintain the difference in their redox potentials in the standard aqueous reduction potentials, whilst the redox potentials of metals with different coordination chemistry (e.g. Zn(II) and Ni (II)) are quite different.

In the case of complexed anion ILs where quaternary ammonium cations (e.g. choline chloride) are used, the cathodic limit of the potential window is governed by the decomposition of quaternary ammonium into alkanes, alkylamines and other products [3.39]. This, interestingly, results in similarity in the cathodic limit for different quaternary ammonium cations.

The anodic limit for complexed anion ILs has been generally correlated to chlorine evolution. However, it is noteworthy that, as electrodes, very few metals are chemically inert in high concentration halides, the anodic limit of which would be controlled by chlorine evolution. In most cases, the oxidative limit is actually governed by the oxidation of the electrode materials.

3.3.3.4 Nb electrodeposition in ionic liquids

Ionic liquid electrolytes can be broken into two categories, viz. those based on complexed anions (usually complexed halide salts) and those relying on closed shell discrete anions (such as BF_4^- , PF_6^- and $[\text{TFSA}]^-$). The two electrolyte types are respectively reviewed with regards to their

electrochemistry and application in Nb electrodeposition.

- Ionic liquids based on complexed anions

In the late 1980s, the ionic liquids based on halogenoaluminate (III) were first introduced in the electrochemical and spectroscopical investigation of a range of transition metal halide complexes [3.40]. The basic formula consists of a metal halide (MeX_a) and an organic halide salt (Cat^+X) (both mostly chloride). The freezing point depression which eventually makes this an 'ionic liquid' comes from a charge delocalisation mechanism due to anionic complexation. Their anhydrous and even aprotic nature (although some of them are hygroscopic) precludes any solvation and solvolysis pathways that are normally conveyed by molecular solvents, whereby the complexed metal species therein have been found somewhat stabilised [3.16]. Nevertheless, such stabilisation may be unwanted from a viewpoint of metal electrodeposition, as the electrochemical reduction of the metal complexes to the elemental state would become less straightforward. This is particularly troublesome for refractory elements, as pointed out by El Abedin who pioneered the work on Ta electrodeposition from IL electrolytes [3.41], since refractory elements generally exhibit rich cluster chemistry in ILs.

The chloride salts of metals like Al [3.16], Zn [3.42] and Fe [3.43] are classified as Lewis acids due to their ability to accept chloride ions. A $\text{MeCl}_x\text{-Cat}^+\text{Cl}$ ionic liquid with a molar proportion of MeCl_x in excess of 0.5 is deemed acidic whilst one less than 0.5 defines a basic nature. The Lewis acidity generally governs the complex equilibria of the system, i.e. in a basic chloride mixture, the free Cl^- anions are in excess for coordination with MeCl_x , favouring the formation of mononuclear anions (MeCl_{x+1}^-); whilst for an acidic chloride mixture (MeCl_x rich), most of the free Cl^- are sequestered as ligands and more likely to be shared by different metal nuclei, thereby favouring the formation of larger, polynuclear anions, this also theoretically increases the threshold potential for

a direct deposition of the metal when compared with the basic system. Such dependence of coordination chemistry on the Lewis acidity and hence on the mixture composition is generally applicable to Al, Zn, Fe and Sn and also true for refractory metals like Nb [3.16].

Only a few spectroscopic investigations exist in the open literature that focus on the coordination chemistry of Nb in a low temperature ionic fluid, i.e. MeCl_x-BMPCl. Conclusive remarks on the composition dependence of coordination chemistry for Nb can hardly be made due to the paucity of investigations, however, some general trends can be assumed as follows,

1) For the ionic liquid is basic or neutral, niobium pentachloride (NbCl₅) tends to form mononuclear metal clusters ([NbCl₆]⁻) with an octahedral structure in excess of free chloride ions.

2) For acidic ionic liquid, the metal complexation of Nb tends to adopt a more polynuclear structure due to the shortage of free chloride ions, wherein dimers are predominant ([Nb₂Cl₁₂]⁻), with a chloride ligand bridging in between.

3) The structure unit for the Nb complexes is octahedral, which is prevalent in metals in groups 3-8 (which include most of the refractory metals), as compared with the less complex linear or tetrahedral structure for metals in groups 11-15 (e.g. Cu, Zn, Sn and Al), and intermediately, the square planar or octahedral structure for metals in groups 9-10 (e.g. Co and Ni). The difficulty of refractory metal electrodeposition is directly related to the complexity of the metal complex structure.

- Ionic liquids based on discrete anions

[BMP][TFSA] is the first discrete anion ionic liquid applied for the electrodeposition of refractory metals [3.16]. Micron-thick, crystalline Ta

finishes have been obtained on Au and NiTi alloy substrates at 200°C, when TaF₅ was used as the metal source with LiF included [3.16]. These authors noted that, the Ta electrodeposits would not be metallic but XRD-amorphous chloride clusters with low oxidation state, when TaCl₅ was utilised in place of TaF₅. These imply that the chloride system seems to be more difficult for Ta reduction than that of fluoride. A maximum deposit thickness (ca. 1 µm) was noted. These authors also attempted to examine whether the same approach is applicable to Nb, and suggested that Nb appears to be more difficult to be completely reduced as compared to Ta.

3.4 Induced Co-deposition

It has become clear that the complete reduction of Nb(V) species from aqueous solutions is neither thermodynamically nor chemically possible. Even though room temperature ionic liquids furnish relatively high potential windows, the inherent low temperatures may cause kinetic hindrance of the Nb reduction. The stepwise and reversible features of reduction routes as well as susceptibility to form oxo-species have been suggested also true for room temperature ionic liquids. Therefore, the production of effective Nb metal coatings remains challenging. For diffusion barrier metallisations, an alternative strategy is to resort to induced co-deposition, where certain refractory elements can be co-deposited with an iron group element (e.g. Ni, Fe and Co) from aqueous solutions, forming an alloy [3.44].

Induced co-deposition is considered anomalous as it allows for deposition of elements that cannot be electrodeposited alone from aqueous systems. The alloy composition cannot be predicted from the electrochemical behaviours of individual constituents. The deposition mechanism is thought to lie in the formation of complexes containing both of the elements. An interesting phenomenon associated with induced co-deposition is the inverse effect of the two metals in electrolytes on the respective kinetics of deposition. Take an

example of Ni-W, increasing the Ni (II) concentration has been found to drastically elevate the partial current density of W deposition [3.45]. Therefore, a Ni-Nb system is of interest in the present study: on the one hand, this metal element pair has been rarely investigated in terms of electrochemistry; on the other hand, the possible combination of Ni (with basic barrier capability) and Nb (with enhanced diffusion barrier characteristics) may make a novel and promising diffusion barrier material.

3.5 Summary

In this chapter, the physical properties and practical applications of Nb metal and oxides have been introduced. The electrochemistry of Nb in various electrolytes including aqueous solutions, high temperature fused salts and room temperature ionic liquids, has been discussed. It has become unequivocal that complete reduction of Nb (V) species into the metallic state is neither thermodynamically nor chemically possible from water-based systems. Such an intrinsic difficulty may be overcome by using low temperature ionic liquids. However, the reversible and stepwise nature of Nb reduction as well as a susceptibility to form oxo-complexes is generally true for all electrolyte categories considered, which prevents formation of effective Nb deposits. Therefore, a possible alternative has been put forward which relies on an induced co-deposition effect. Both Ni and Nb exhibit polynuclear speciation, this in turn may enable the formation of Ni-Nb complexes, whereby Nb can be co-deposited with Ni giving rise to an effective electrodeposited layer promising for diffusion barrier metallisations.

3.6 References

- [3.1] C. K. Gupta and A. K. Suri, *Extractive Metallurgy of Niobium*, CRC Press, Chapter 1, 5 (1993).
- [3.2] F. Cardarelli, P. Taxil, A. Savall, C. Comninellis, G. Manoli and O. Leclerc, *J. Appl. Electrochem.*, **28**, 245 (1998).

- [3.3] G. W. Mellors and S. Senderoff, *J. Electrochem. Soc.*, **112** (3), 266 (1965).
- [3.4] N. S. Chong, J. L. Anderson and M. L. Norton, *J. Electrochem. Soc.*, **136** (4), 9 (1989).
- [3.5] H. Zillgen, M. Stenzel and W. Lohwasser, *Active Passive Electron. Compon.*, **25**, 147 (2002).
- [3.6] K. Tanabe, *Catalysis Today*, **8** (1), 1 (1990).
- [3.7] E. I. Ko, J. M. Hupp and N. J. Wagner, *J. Chem. Soc., Chem. Commun.*, **19**, 94 (1983).
- [3.8] D. Bach, H. Stormer, R. Schneider, D. Gerthsen and J. Verbeeck, *Microsc. Microanal.*, **12**, 416 (2006).
- [3.9] D. Landolt, *J. Electrochem. Soc.*, **149**, S9 (2002).
- [3.10] N. Kanani, *Electroplating: Basic Principles, Processes and Practice*, Elsevier, Oxford, (2004).
- [3.11] R. Rosenberg, D. C. Edelstein, C. K. Hu and K. P. Rodbell, *Annu. Rev. Mater. Sci.*, **30** (1), 229 (2000).
- [3.12] ASTM B 374 - 96, *Standard Terminology Relating to Electroplating*, American Society for Testing and Materials, Pennsylvania.
- [3.13] P. H. Rieger, *Electrochemistry*, 2nd Ed., Chapman & Hall, (1994).
- [3.14] N. Eliaz, A. Shachar, B. Tal and D. Eliezer, *Eng. Fail. Anal.*, **9**, 167 (2002).
- [3.15] C. Gabrielli, F. Huet and R. P. Nogueira, *Electrochimica Acta*, **50**, 3726 (2005).
- [3.16] F. Endres, D. MacFarlane and A. Abbott, (Eds.) *Electrodeposition from ionic liquids*, Wiley-VCH (2008).
- [3.17] S. Z. El Abedin, H. K. Farag, E. M. Moustafa, U. Welz-Biermann and F. Endres, *Phys. Chem. Chem. Phys.*, **7** (11), 2333 (2005).
- [3.18] O. B. Babushkina, S. Ekres and G. E. Nauer, *J. Phys. Chem. A*, **112** (36), 8288 (2008).
- [3.19] S. J. Kiehl and D. Hart, *J. Amer. Chem. Soc.*, **50**, 2337 (1928).

- [3.20] S. Zeltzer, *Coll. Czech. Chem. Commun.*, **4**, 319 (1932).
- [3.21] D. Cozzi and S. Vivarelli, *Ber. Bunsenges. Phys. Chem.*, **58**, 177 (1954).
- [3.22] S. Senderoff and G. W. Mellors, *Science* (New York, NY), 153 (3743), 1475 (1966).
- [3.23] S. Senderoff and G. W. Mellors, *J. Electrochem. Soc.*, **114** (6), 556 (1967).
- [3.24] P. Chamelot, B. Lafage and P. Taxil, *J. Electrochem. Soc.*, **143** (5), 1570 (1996).
- [3.25] F. Endres, *Chem. Phys. Chem.*, **3** (2), 144 (2002).
- [3.26] A. P. Abbott, and K. J. McKenzie, (2006). *Phys. Chem. Chem. Phys.*, **8** (37), 4265 (2006).
- [3.27] S. Z. El Abedin, A. Y. Saad, H. K. Farag, N. Borisenko, Q. X. Liu and F. Endres, *Electrochimica Acta*, **52** (8), 2746 (2007).
- [3.28] P. He, H. Liu, Z. Li, Y. Liu, X. Xu and J. Li, *Langmuir*, **20** (23), 10260 (2004).
- [3.29] A. P. Abbott, K. El Ttaib, K. S. Ryder and E. L. Smith, *Trans. Inst. Met. Finish.*, **86** (4), 234 (2008).
- [3.30] J. A. Mitchell, W. R. Pitner, C. L. Hussey and G. R. Stafford, *J. Electrochem. Soc.*, **143** (11), 3448 (1996).
- [3.31] A. P. Abbott, G. Capper, K. J. McKenzie and K. S. Ryder, *J. Electroanal. Chem.*, **599** (2), 288 (2007).
- [3.32] G. E. Gray, P. A. Kohl and J. Winnick, *J. Electrochem. Soc.*, 142 (11), 3636 (1995).
- [3.33] Y. Li, J. Yang, J. Wang, J. Xu and P. Wang, *Electrochemical and Solid-State Letters*, **8** (11), C166 (2005).
- [3.34] S. Zein El Abedin, E. M. Moustafa, R. Hempelmann, H. Natter and F. Endres, *Chem. Phys. Chem.*, **7** (7), 1535 (2006).
- [3.35] G. R. Stafford and G. M. Haarberg, *Plasmas & Ions*, **2** (1), 35 (1999).
- [3.36] A. J. Bard and L. R. Faulkner, *Electrochemical Methods: Fundamentals and Applications*, John Wiley & Sons, New York, p. 11 (2001).

- [3.37] H. Ohno, (Ed.) *Electrochemical aspects of ionic liquids*. Hoboken (NJ): Wiley (2005).
- [3.38] A. P. Abbott, G. Capper, D. L. Davies, R. K. Rasheed, and P. Shikotra, *Inorgan. Chem.*, **44** (19), 6497 (2005).
- [3.39] M. Galova, *Electrochem. Acta.*, **29**, 323 (1984).
- [3.40] C. L. Hussey, *Pure Appl. Chem.*, **60**, 1763 (1988).
- [3.41] S. Z. El Abedin, H. K. Farag, E. M. Moustafa, U. Welz-Biermann and F. Endres, *Phys. Chem. Chem. Phys.*, **7** (11), 2333 (2005).
- [3.42] S. I. Hsiu, J. F. Huang, I. W. Sun, C. H. Yuan and J. Shiea, *Electrochimica Acta*, **47** (27), 4367 (2002).
- [3.43] M. S. Sitze, E. R. Schreiter, E. V. Patterson and R. G. Freeman, *Inorg. Chem.*, **40**, 2298 (2001).
- [3.44] N. Eliaz and E. Gileadi, *Induced co-deposition of alloys of tungsten, molybdenum and rhenium with transition metals*, In *Modern Aspects of Electrochemistry*, Springer, New York, 191 (2008).
- [3.45] O. Younes, E. Gileadi, *J. Electrochem. Soc.*, **149**, C100 (2002).

Chapter 4

Experimental Techniques

This chapter describes the various techniques employed in the materials processing and subsequent characterisation of electrodeposited specimens.

4.1 Electrochemical Analysis and Electrodeposition

4.1.1 Electrodeposition Cell and Electrode Pretreatment

All the galvanostatic, potentiostatic and voltammetric investigations were performed in a 100 mL beaker. The electrodeposition cell was controlled by a potentiostat (Schlumberger SI 1286) or a TTi QPX 1200SP power supply together with a computer for the former. A three-electrode cell configuration (See **Figure 4.1**) was utilised unless in the case of galvanostatic trials where the reference electrode was absent. The heating unit was a hot plate together with a thermometre immersed in the electrolyte to monitor the temperature.

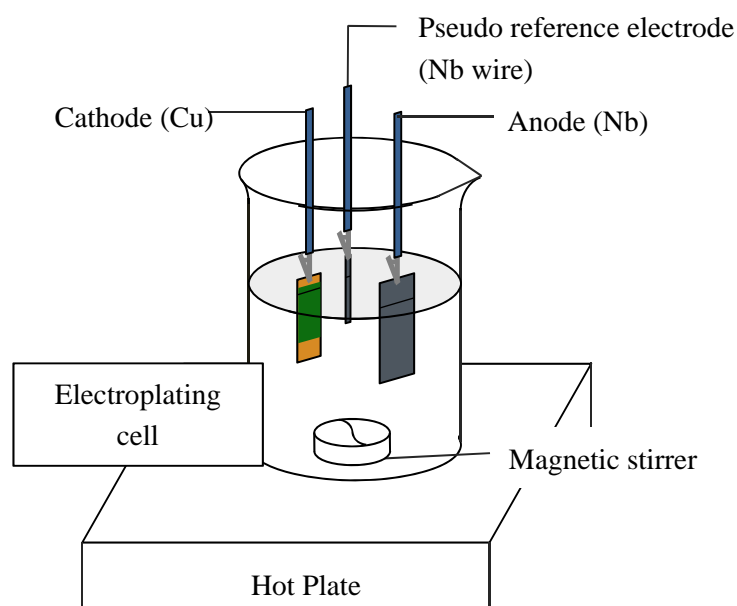


Figure 4.1 Schematic diagram illustrating a typical, three-electrode electrodeposition cell configuration applied in this work

Cu substrates with a thickness of 100 μm (Advent Research Materials, 99.9%) were utilised as cathodes unless otherwise stated. The electroplated area for each coupon was set as 1 cm \times 1 cm, defined by chemically inert tape (3M) masking. Attempts to utilise either platinised titanium mesh electrode or untreated graphite rod for the anode were unsuccessful, the former because of the detection of Pt in the deposits, indicating partial dissolution of the inert electrode, whilst dissolution of the graphite was signified by discolouration of the plating bath upon electrolysis. Therefore a Nb metal sheet ((99.9%, 500 μm thickness, Advent Research Materials) was chosen as the anode to prevent contamination. To assess the cathode potentials, a silver wire quasi-reference electrode was initially employed nevertheless problems arose due to dissolution of Ag into the electrolyte. Therefore, this reference electrode was replaced by Nb metal wire, positioned approximately 1.5 cm away from the Cu cathode.

The pretreatment for Cu coupons involved ultrasonic cleaning in acetone for 5 min, followed by acid pickling in 20 vol.% H_2SO_4 (S.G.: 1.83) for 45 s, subsequent thorough rinsing in deionised water and drying under compressed air. The niobium anode was ultrasonic cleaned in acetone for 5 min and then dried under compressed air before being immersed into the electrolyte.

4.1.2 Electrolytes

For initial investigations, Type III deep eutectic solvents (DESs) were utilised as electrolytes, with the niobium metal source introduced either by direct dissolution of halide salts or anodic dissolution of Nb metal. This electrolyte system was phased out later on due to its inability to produce effective Nb-based electrodeposits and low solubility of Nb metal source. The choice of DES was a mixture of choline chloride ($\text{HO-CH}_2\text{CH}_2\text{-N}(\text{CH}_3)_2\text{CH}_3\text{Cl}$) (Sigma Aldrich 99.5%) and either urea ($\text{CO}(\text{NH}_2)_2$) (Sigma Aldrich > 99%) or ethylene glycol ($\text{HO-CH}_2\text{CH}_2\text{-OH}$) (EG) (99.8%, Sigma Aldrich) in a molar ratio of 2:1.

The mixing of the components was carried out in an open beaker at 75°C until a colourless and homogeneous liquid formed.

The Type IV sub-class of DESs, i.e. a mixture of metal salt (or hydrate) and hydrogen bond donor [4.1] was also investigated, owing to its general improved fluidity and compatibility with Nb halide salts. Ni halide was introduced to make a Ni-Nb double salt system in an attempt to raise the possibility of Nb reduction potentially through an induced catalytic co-deposition mechanism. NbCl₅ (99.9%, Sigma Aldrich), NiCl₂ hexahydrate (NiCl₂ · 6H₂O) (99%, Fisher), NaBH₄ (99.99%, Sigma Aldrich), ethylene glycol and propylene glycol (HO–CH(CH₃)CH₂–OH) (PG) (99.5%, SAFC) were utilised as received. Yellowish NbCl₅ solid was quickly transferred to either EG or PG to prevent hydrolysis (white discoloration forming NbOCl₃) in air, giving an exothermic dissolution. The solution was thereafter heated to 75°C with magnetic stirring agitation at 60 r.p.m. until a homogenous and colourless liquid formed. This was followed by controlled, fractional additions of NaBH₄ in the fume cupboard for the purpose of reducing proton concentrations in the electrolyte [4.2] and hence increasing cathodic current efficiency during electrodeposition. It is noteworthy that NaBH₄, a conventional reducing agent for electroless Ni deposition, only acts to reduce H⁺ ions instead of Ni²⁺ ions in this system. Upon NaBH₄ additions, vigorous hydrogen evolution with the co-release of a white cloud (presumably HCl) occurred. The solution was then left agitated until an ivory hued liquid formed. Finally, NiCl₂ salt was added yielding a homogenous celadon-green solution.

4.1.3 Electrical Conductivity Assessment of Electrolytes

The electrical conductivity of electrolytes was measured using a Jenway 4200 Conductivity Meter with a platinised titanium probe. The data were recorded until the reading became stabilised. The probe in contact with solution was rinsed with deionised water and thoroughly dried under compressed air *before*

and *after* each measurement attempt.

4.1.4 pH Measurements

For non-aqueous electrolytes, the determination of the solution pH is normally handicapped by the conventional, all-aqueous pH electrode arrangement. This is due to the mixing of the aqueous reference-electrode-filling electrolyte and the non-aqueous electrodeposition solution through the junction leading to a continual, negative drift of the pH value. Nevertheless, it has been suggested, by allowing a short period of electrolyte contact, the changes in the apparent acidity could be approximated [4.3]. Therefore, the attainment of pH was made using a Hanna HI 8424 pH meter. The readings were approximated to the nearest tenth of a pH unit (± 0.2 pH).

4.1.5 Cyclic Voltammetry

Cyclic voltammetry (CV) is an electrochemical transient technique where the potential is swept at a constant rate between two potential values and that change in the current is measured with respect to the change in potential. CV enables the study of the redox behaviour of the electrochemically active species in electrolytes.

Cyclic voltammetric trials were performed within the three-electrode cell, which consisted of a 2 mm (diameter) glassy carbon (GC) disc working electrode, a platinised titanium counter electrode and silver pseudo reference electrode. Before each electrochemical analysis trial, the working electrode was polished utilising 0.05 μm alumina and rinsed utilising water and ethanol. Voltammetric trials were performed initiating from the open circuit potential (OCP, potential at which no electrochemical activity occurs) towards the cathodic end to obviate the introduction of Cu^{2+} ions into the plating bath (by anodic dissolution of the Cu cathode) at temperatures ranging from 20 to 200°C and at a scan rate ranging from 10 to 100 mV/s. In each case three independent curves were

acquired to examine the consistency and one representative was presented.

4.1.6 Electrodeposition

Direct current galvanostatic deposition trials were undertaken in a three-electrode cell consisting of a copper working electrode with its electrochemical active area defined by chemical resistant tape (3M), a niobium metal counter electrode and a niobium metal pseudo reference electrode. Deposition was conducted at temperatures up to 200°C with agitation at 240 r.p.m.. To investigate the effect of cathodic current density on the electrodeposition process (e.g. coating microstructure, composition and thickness), current densities ranging from 20 to 400 mA/cm² were employed, with equivalent electric charge passed unless otherwise noted.

4.1.7 Quartz Crystal Microbalance

A quartz crystal's resonance frequency varies when a small amount of mass changes occurs at its surface [4.4]. Taking advantage of this phenomenon, the electrochemical quartz crystal microbalance (EQCM) has been developed to monitor the deposition/dissolution kinetics at an electrode by *in-situ* tracking its changes in the oscillation frequency [4.5]. In the present study, the EQCM experiments were carried out on AT-cut 100 MHz quartz resonators in conjunction with Pt electrode (piezoelectric active area: 0.23 cm²). A three-electrode cell configuration was utilised (See **Figure 4.2**), with the QCM Pt as the working electrode, a niobium sheet counter electrode and a niobium wire quasi-reference electrode. The QCM-Pt was made facing down towards the counter electrode (a bent Nb metal sheet).

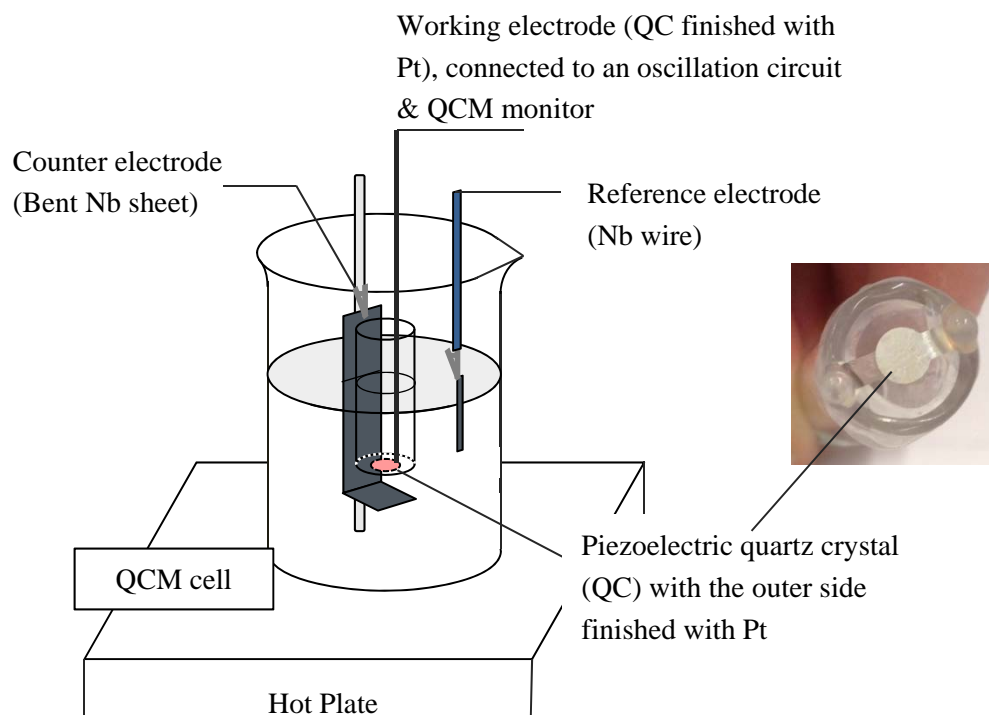


Figure 4.2 Schematic diagram illustrating a three-electrode cell configuration utilised for EQCM measurements

Prior to each experiment, the working electrode was rinsed using deionised water and ethanol. All the measurements were performed within a frequency range close to the crystal resonance frequency utilising a HP87512A network analyser in reflectance mode. A repetitive scan was carried out to continually acquire admittance spectrum of the quartz crystal. The mass change of the QCM was derived from the shift in the peak frequency using a Sauerbrey equation (**Equation 4-1**).

$$\Delta f = - \frac{2f_0^2}{Z_Q} \frac{\Delta m}{A} \quad (\text{Equation 4-1})$$

Where Δf denotes the frequency change, f_0 represents the frequency of the unloaded crystal, Z_Q is the mechanical impedance of the quartz crystal, Δm denotes the crystal's mass change and A is the piezoelectrically active crystal area.

4.2 Soldering and Thermal Transients

Prior to soldering, the electrodeposited samples were thoroughly rinsed using distilled water and dried under compressed air. Eutectic 52In-48Sn solder paste (Indalloy 1E, Indium Corporation, USA) incorporating a Ni-compatible flux NC-SMQ80 was manually deposited onto the specimen's surface through a syringe, with an average paste thickness of 2 mm. The melting point of the solder is 118°C, so a subsequent reflowing at 200°C in air on a hotplate for 60 s was sufficient to facilitate possible solder reaction. The specimens were then withdrawn and left air-cooled until room temperature and rinsed with distilled water and acetone before exposure to thermal transients in an ambient furnace at 200 °C for periods up to 14 days. During the thermal transients (diffusion tests), the solder remained molten and still in the central area of the deposited sample, constrained by 3M tape. Solder spreading, manifesting itself in an evident decrease in the contact angle with the underlying deposited sample surface, occurs when solder starts to penetrate through the diffusion barrier coating. This may be either due to cracking present in the Ni-Nb-based coating structure providing direct ingress pathways, or attributed to the interdiffusion across the solder-coating interface. Therefore, it became necessary to examine the compactness of the coatings after thermal transients through metallographic cross sectioning approaches, as any cracking across the coating structure may lead to premature failure of the diffusion barrier coating.

4.3 Electron Microscopy

Scanning electron microscopy (SEM), transmission electron microscopy (TEM) and scanning transmission electron microscopy (STEM) were employed to obtain morphological, microstructural, compositional and crystallographic information of samples both as-deposited and after solder reaction under thermal transients.

4.3.1 Scanning Electron Microscopy

4.3.1.1 Sample preparation

For SEM observations, the surface morphology of specimens can be examined directly, whereas enquiring into the microstructure, metallographic cross sectioning is required. In this study, cross-sections were prepared by mounting a sample in epoxy resin, grinding using silicon carbide papers (240, 400, 800 and 1200 grit, successively) and polishing using diamond suspensions (6 μm diamond with DP-Lubricant Blue and 3 μm diamond with DP-Lubricant Red), which were all provided by Struers (UK). The final polishing was performed with colloidal silica (0.04 μm). For soldered specimens, as a substrate-barrier layer-solder, multilayer structure entails preparation, the scratches on the underlying copper substrate (with higher hardness compared to the In-Sn solders) were tolerated. Before SEM investigations, the cross-sectioned samples were sputtered with Pt (instead of Au) for 1 min to enable good electrical conduction. The use of Au sputtering was impossible as Nb $L\alpha$ (2.16 KeV) overlaps with Au $M\alpha$ (2.12 KeV) in the energy-dispersive X-ray spectroscopy (EDX) spectrum, handicapping compositional quantification.

4.3.1.2 Instrumentation

Scanning electron microscopy (SEM) was conducted using a Leo 1530VP field emission gun SEM (FEGSEM), which was equipped with an energy dispersive X-Ray spectroscopy (EDX) analyser. The SEM typically operated at an extra high tension voltage (EHT) of 10 kV for imaging and at 20 kV for EDX analysis. The EDX data was handled by AztecEnergy software (Oxford Instruments).

4.3.2 Transmission Electron Microscopy

4.3.2.1 Sample preparation

For TEM characterisations, a specimen needs to be not exceeding ca. 300 nm thick to ensure electron transparency and hence high imaging quality. The thin

foil was extracted from the bulk sample with gallium ion milling using a FEI Nova 600 Nanolab Dual Beam Focused Ion Beam SEM (FIB/SEM). This was initiated with the chemical vapour deposition of a protective Pt over-layer onto sample surface (See **Figure 4.3(a)**). It was followed by preparation of rectangular trenches at the both sides of the Pt deposit. The thin film was then prepared by a 'U'-cut and attached to Omniprobe (**Figure 4.3(b)**). After that, it was mounted onto a TEM copper grid and subject to final thinning (an example is shown in **Figure 4.4**) to electron transparency.

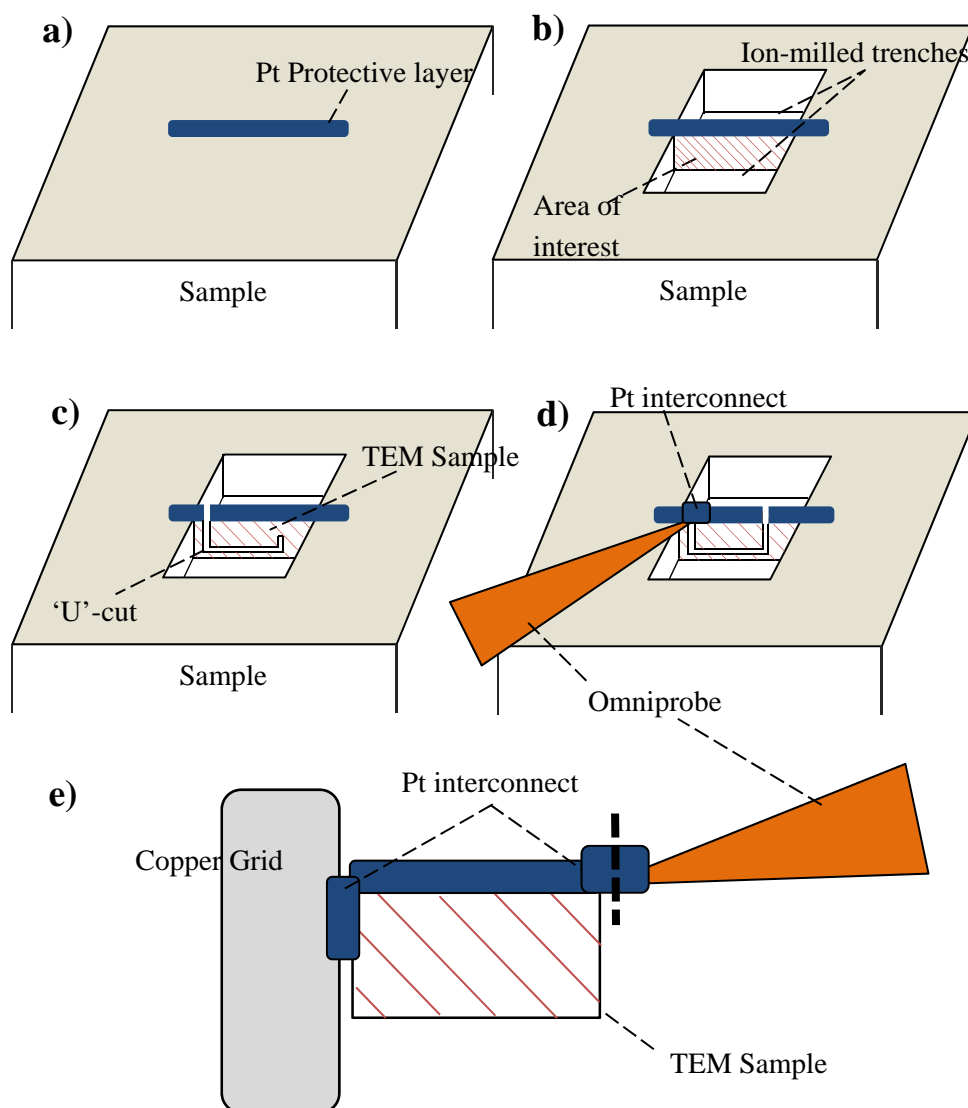


Figure 4.3 Schematic diagram illustrating micro-machining process by SEM/FIB for TEM sample preparation: a) Pt layer deposited on top of an area of interest; b) preparation of two trenches at both sides of the Pt deposit; c) 'U'-cut of the thin film sample for lift-out; d) thin film sample attached to Omniprobe and lifted out and e) thin film attached to copper grid ready for further thinning.

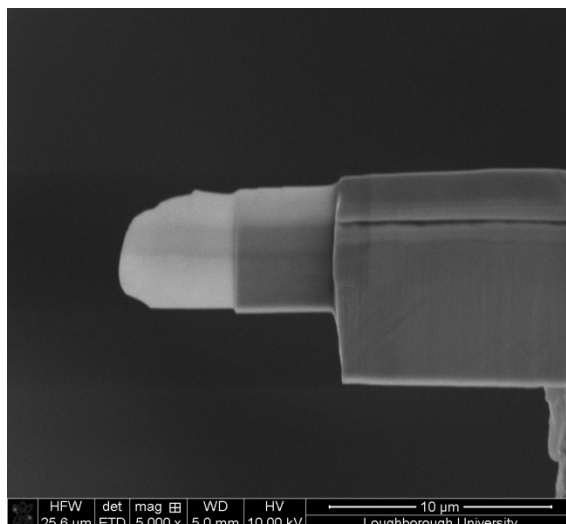


Figure 4.4 SEM image showing a TEM thin foil sample prepared using focused ion beam milling where the leftmost end is the area of interest

4.3.2.2 Instrumentation

Transmission electron microscopy (TEM) was performed using either a JEOL 2000FX TEM equipped with Oxford Instrument INCA EDX spectroscopy, or an FEI Tecnai F20 field emission gun TEM (FEGTEM) with Oxford Instrument INCA EDX system and 80 mm² X-Max silicon drift detector. The latter FEGTEM was equipped with a high angle annular dark field (HAADF) detector, which is able to collect electrons that are not Bragg scattered, whereby the imaging contrast comes mainly from differences in atomic number (Z) of the elements, in place of any diffraction effect. This enables the HAADF imaging mode to provide a direct indication of the compositional variation within the thin foil sample. Moreover, the EDX detector of the FEGTEM could provide X-ray compositional mapping due to the high count rates. Selected-area diffraction pattern (SADP), with an aperture (sampling) size of ca. 1.3 μm , was conducted to inspect the crystallographic information of sample area at a micron scale.

4.4 X-ray Photoelectron Spectroscopy

X-ray Photoelectron Spectroscopy (XPS) is developed based on the well-known photoelectric effect, where atoms emit photoelectrons excited by

X-ray beam irradiation [4.6]. The electrons emitted at various binding energies passed through an electron multiplier and are eventually collected by an analyser, yielding an electron spectrum representing quantity of electrons collected as a function of their binding energy (eV). Therefore each element leaves a characteristic set of peaks (a 'fingerprint' pattern) in electron spectrum and hence enabling element identification. By calculating the area under the peaks, the quantitative analysis of atomic composition could also be achieved.

In this project, XPS analysis was carried out to ascertain the chemical state of element species present on the electrodeposited sample surface, which helps understand the electrochemical reduction routes for each element being deposited. In conjunction with sputter profiling, the in-depth distribution of deposit composition and chemistry was also obtained. A Thermo Scientific K-Alpha X-ray Photoelectron Spectrometer with an aluminium source was utilised. Electron spectra were charge referenced to C1s at 284.8 eV due to adventitious carbon. Depth profiling was conducted using either argon monomer-ion beam at Loughborough University or argon cluster-ion beam source at National EPSRC XPS Users' Service (NEXUS, UK). The latter cluster ion beam source has the advantage of being free from any artificial chemical reduction experienced in some cases where the former monomer ion beam has been employed [4.7]. Each sputtering cycle proceeded with complete computer-centric rotation of the sample to facilitate equal material removal. Between etch cycles an electron spectrum was recorded as such to profile compositional and chemical information across the sample thickness. The choice of sputtering step size and total depth was subject to practical sputtering yields of the materials.

4.5 Electrical Conductivity Attainment of Thin Film Specimens

The electrical resistance of the electrodeposited specimens was assessed by four-point probe using a Keithley 2440 5A Source meter. The approach

comprises placing four equidistant probes (See **Figure 4.5**) that make contact alongside a line at the sample surface. A current is passed through the outer probe pair whilst the floating voltage across the inner pair is tracked. The resistivity is derived using **Equation 4-2** [4.8].

$$\rho_{\square} = \frac{\pi}{\ln 2} \frac{V}{I} \quad (\text{Equation 4-2})$$

Where ρ_{\square} refers to sheet resistance ($\text{m}\Omega/\square$ or $\text{m}\Omega/\text{square}$), V is the voltage (mV) across the inner probe pair, I is the electric current (A) imposed through the outer pair. The sheet resistance represents the resistivity for a uniform thickness so the common resistivity unit, $\Omega \cdot \text{m}$, is divided by the thickness, m , giving a final answer in Ω , or Ω/\square for differentiation.

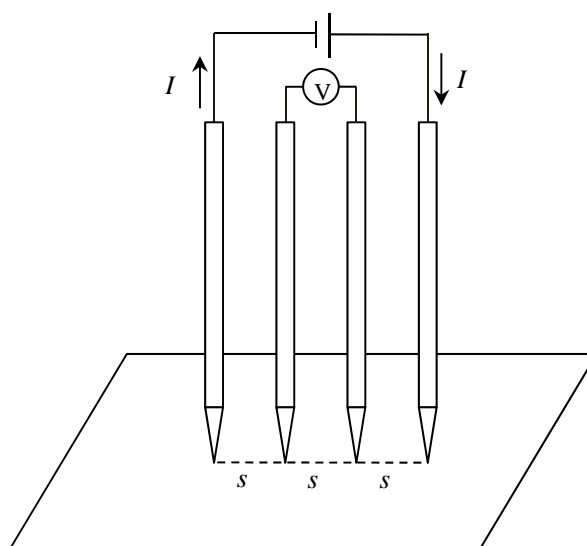


Figure 4.5 Schematic diagram illustrating the four-point probe configuration for thin film resistance measurements

4.6 Solderability Measurements of Thin film Specimens

Solderability measures how the substrate surface is wet by the molten solder materials during solder reflowing process. It is vital to the interfacial adhesion and hence mechanical integrity of the solder interconnections. The wettability of electrodeposited samples with eutectic 52In-48Sn solder, described by contact angle (CA) between solder and underlying coatings, was assessed

using a Data Physics SCA20 Contact Angle Analyser. A typical optical micrograph acquired for such measurements is given in **Figure 4.6**. Principally the lower the contact angle, the more wettable the specimen is.

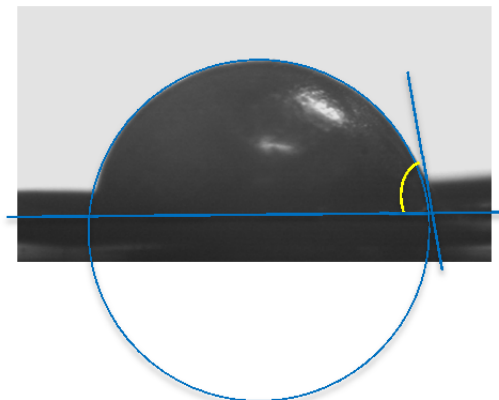


Figure 4.6 A representative optical micrograph presenting a 95.8Ni-4.2Nb coated sample surface after soldering with eutectic 52In-48Sn solder from a side-view (blue lines set to facilitate contact angle (CA) measurement whilst the yellow angle denotes the CA)

4.7 References

- [4.1] A. P. Abbott, J. C. Barron, K. S. Ryder and D. Wilson, *Chem. Eur. J.*, **13** (22), 6495 (2007).
- [4.2] H. I. Schlesinger, H. C. Brown, A. E. Finholt, J. R. Gilbreath, H. R. Hoekstra and E. K. Hyde, *J. Amer. Chem. Soc.*, **75** (1), 215-219 (1953).
- [4.3] S. P. Porras and E. Kenndler, *J. Chromatogr. A*, **1037**, 455 (2004).
- [4.4] G. Sauerbrey, *Z. Phys.*, **155**, 206 (1959).
- [4.5] A. P. Abbott, K. El Ttaib, G. Frisch, K. J. McKenzie and K. S. Ryder, *Phys. Chem. Chem. Phys.*, **11** (21), 4269 (2009).
- [4.6] S. Hofmann, in *Auger- and X-ray Photoelectron Spectroscopy in Materials Science: A User-oriented Guide*, Springer Series in Surface Sciences, p.7, Springer (2012).
- [4.7] T. Choudhury, S. O. Saied, J. L. Sullivan, and A. M. Abbot, *J. Phys. D: Appl. Phys.*, **22**, 1185 (1989).
- [4.8] F. M. Smits, *Bell Sys. Tech. J.*, **34**, 711 (1958).

Chapter 5

Nb Electrochemistry in Type III and Type IV Eutectic Solvents and Derivatives

The objectives of this chapter are to investigate the electrochemistry of Nb species in Type III and Type IV eutectic solvents and derivatives and thereby establishing an electrolyte for the effective deposition of Nb-based diffusion barrier metallisations. Various Nb metal precursors and their associated electrochemical behaviours in the eutectic solvents will be investigated, whilst the technical challenges with respect to electrolyte workability and electrode stability are examined. Finally, an alternative approach to producing Nb-based metal coatings is briefly introduced, i.e. Ni-Nb co-deposition.

5.1 Introduction of Niobium Metal Precursors

The nature and concentration of metal precursors in the electroplating solutions determine the speciation and hence the electrochemical reduction routes of metal ions. When it comes to the selection of Nb metal source, its solubility, chemical compatibility with the electrolyte component, the effect on the physical properties of the electrolyte (e.g. electrical conductivity and viscosity) and the electrochemical behaviours have to be considered. The present investigations were initially set out to employ non-aqueous, deep eutectic solvents as electrolyte baselines, which generally behave as ionic liquids with relatively wide electrochemical potential windows and are not susceptible to metal salt hydrolysis due to the absence of water. Furthermore, their robustness, e.g. reflected in the limited effect of water impurity therein on the electrochemical behaviour, allows for their operation in the ambient and hence good industrial applicability.

Two types of niobium metal sources have been investigated, which include niobium chlorides and anodic dissolution of Nb metal.

5.1.1 Niobium (V) Chloride

Niobium pentachloride (NbCl_5) is a volatile and hygroscopic powder which undergoes quick colouration from yellow into white in the ambient. The investigation initiated with NbCl_5 due to its wide availability. Its low solubility (< 1wt.%) in most ionic salts, however, prohibited high metal concentration investigations in choline chloride (ChCl) based eutectic solvents such as reline ($[\text{ChCl}] : [\text{urea}] = 1:2$) and ethaline ($[\text{ChCl}] : [\text{ethylene glycol}] = 1: 2$). At 200 mM NbCl_5 at 75°C, reline gave a turbid, colourless solution, suggesting it was beyond its saturation limit for NbCl_5 . The solubility did not appear to be significantly increased by elevating the temperature, even up to 140°C. In the case of Type IV deep eutectic solvents which are a mixture of a metal salt and an hydrogen bond donor, NbCl_5 did not form a eutectic mixture with urea upon heating, but can form mixtures with glycols such as ethylene glycol or propylene glycol. The high solubility of the Nb halide salt in Type IV eutectic solvents has made this electrolyte sub-class appear suitable for Nb electrodeposition from NbCl_5 .

5.1.2 Anodic Dissolution of Niobium Metal

Another approach to introduce a Nb metal source has been the anodic dissolution of Nb metal into the choline-based Type III deep eutectic solvents (i.e. reline). The strong passivation of refractory metals like Nb, however, has proved difficult for their anodic dissolution (or electropolishing) [5.1]. Potentiostatically anodic dissolution of Nb metal (supplied in sheets) has been achieved at a positive potential of + 7 V at 120°C in both reline and ethaline in a single-compartment cell with a graphite rod as counter electrode and a Nb wire quasi-reference electrode for preventing the contamination of impure metal cations. The amount of the Nb dissolved was estimated based on weight

loss measurement. It has been demonstrated that a Nb sheet with immersed dimensions of 0.0125 cm × 1 cm × 2 cm (corresponding to ca. 0.2g Nb) can be completely dissolved within 550s in both reline and ethaline at + 7 V vs. Nb and at 120°C. **Figure 5.1** shows the variation of current density with time, where an apparent diminishing of the current density is attributable to a reduction in the surface area of the Nb metal film as it was being dissolved. It was also observed that, by increasing temperature from 120°C to 180°C, any potentiostatic trial at a potential positive of + 2 V (vs. Nb) could enable accelerated dissolution of Nb metal. The high voltage required for a successful Nb anodic dissolution (i.e. + 7 V vs. Nb at 120°C) may be partly attributed to a significant ohmic potential drop when the current passes the tenacious Nb oxide layer on the Nb metal surface, which results in a lower overpotential on the electrode surface than the potential monitored by the potentiostat.

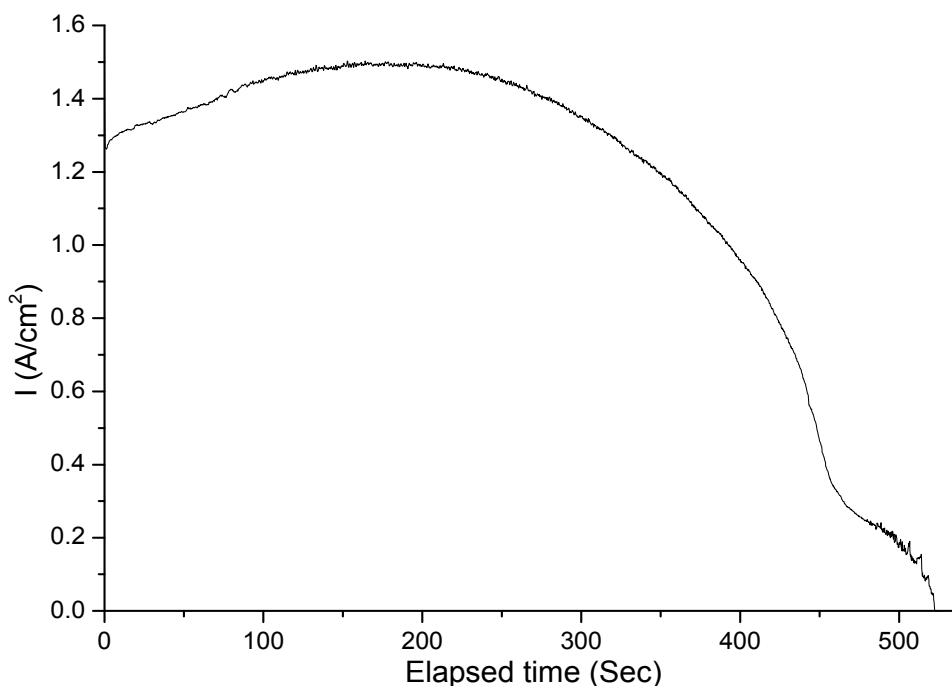


Figure 5.1 Potentiostatic curve showing a typical anodic dissolution of Nb metal (ca. 0.2g) in reline at + 7V (vs. Nb) and at 120°C

The actual solid-phase dissolution of Nb can occur when a critical potential is reached below which only surface passivation takes place and above which transpassive corrosion occurs. **Figures 5.2** presents the appearance of the Nb

metal sheet after anodic dissolution at + 3 V and + 7 V (vs. Nb wire) for 60 min, respectively, which show the two distinct anodic mechanisms: passivation forming bluish Nb_2O_5 layer in **Fig. 5.2 (a)** and transpassive corrosion (i.e. dissolution) in **Fig. 5.2 (b)**. The critical potential at which the transpassive corrosion occurs seems to become less noble with an increase in temperature. It is also worth noting during the anodic dissolution trials that, for reline, the bath was coloured in stages, from colourless through slightly greyish to brown grey, whilst the transparent ethaline was turned white and turbid, suggesting the decomposition of ethylene glycol.

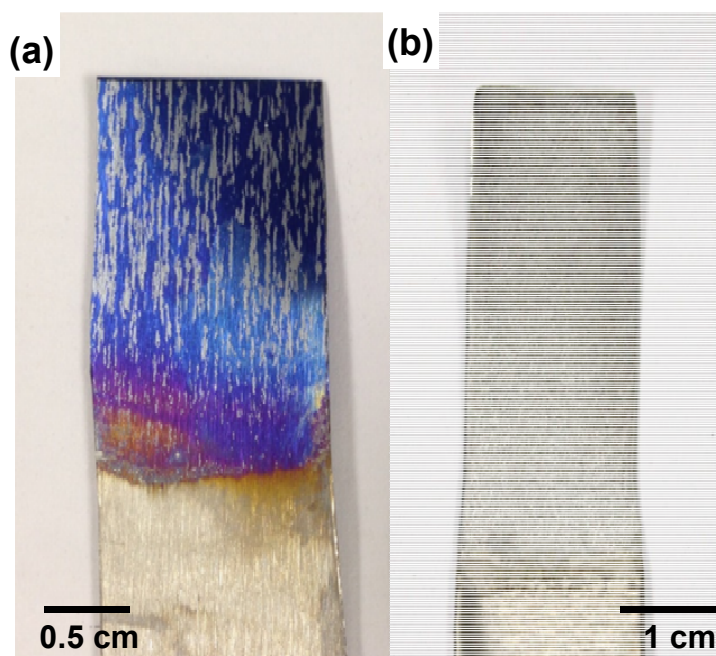


Figure 5.2 Photographs showing the appearance of the Nb metal sheet after anodic dissolution at a) +3 V and b) + 7 V (vs. Nb wire) for 60 min

5.2 Electrochemical Behaviour of Type III Deep Eutectic Solvents Dissolved with NbCl_5

The electrochemical reduction behaviour of reline in which NbCl_5 was dissolved exhibited a temperature dependence. Cyclic voltammograms as a function of temperature for the reline in the presence and absence of 0.2 M NbCl_5 are presented in **Figs. 5.3-5.6**. In the case of reline-0.2 M NbCl_5 (**Figs. 5.3 & 5.4**), an intensifying and irreversible reduction peak, along with a tendency to shift towards more positive potentials, was observed at about -1.8

V, as the temperature was increased. The peak shift can be attributed to an enhanced ionic activity with increasing temperature. Whilst in the absence of NbCl_5 , an irreversible reduction current with less intensity was evident at -2.0V . The effect of NbCl_5 upon cyclic voltammetric response at 125°C is depicted in **Fig. 5.6**. For both cases, no apparent change occurred to the glassy carbon microelectrode surface after potentiostatic deposition trials at the reduction potentials for up to 30 min. Therefore, the reduction current at -1.8 V (vs. Ag wire) in the NbCl_5 dissolved system may be ascribed to partial reduction of Nb (V) species, although not to the metallic state. The reduction current at -2.0 V (vs. Ag wire) in the neat reline is due to the partial decomposition of ChCl , possibly via a chain scission process yielding trimethylamine gas [5.2].

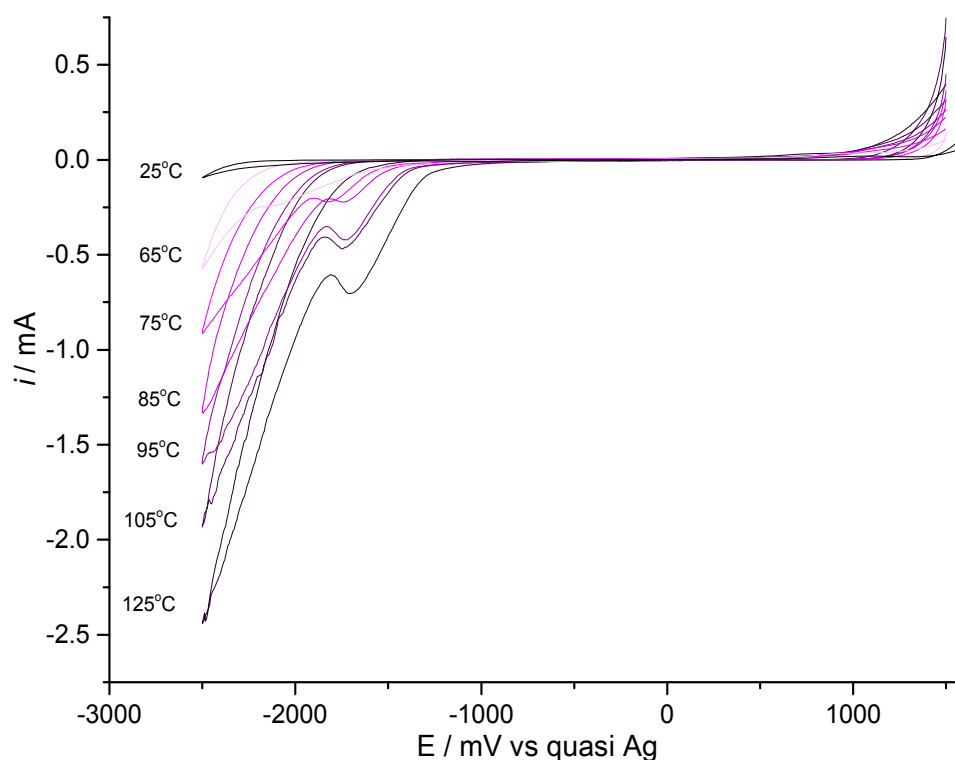


Figure 5.3 Cyclic voltammograms of a glassy carbon electrode immersed in ChCl:2Urea DES containing 0.2 M NbCl_5 at a range of temperature from 25 to 125°C and a scan rate of 100 mV/s

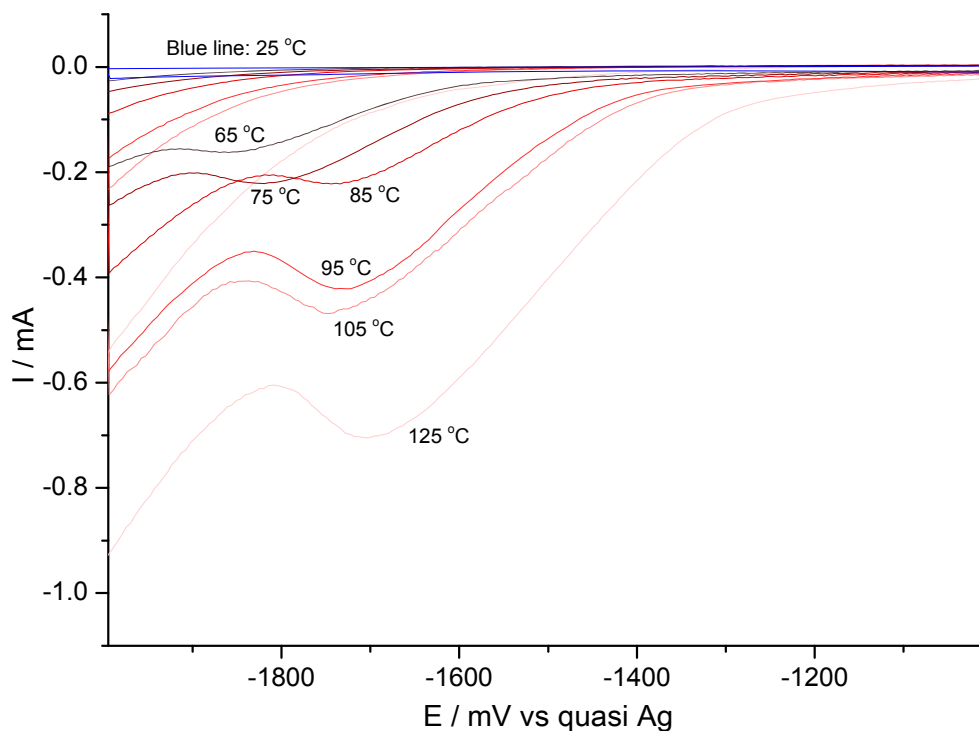


Figure 5.4 An enlarged scale (from -2 to -1 V) of cyclic voltammograms (shown in Figure 5.3) of a glassy carbon electrode immersed in ChCl:2Urea DES containing 0.2 M NbCl₅ at a range of temperatures from 25 to 125°C and a scan rate of 100 mV/s.

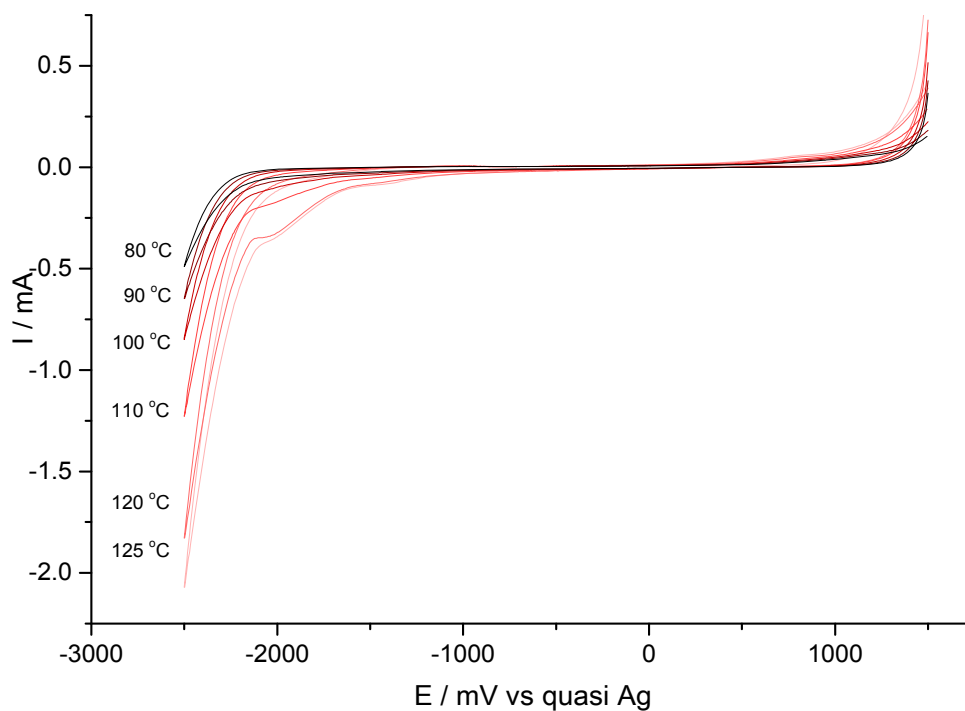


Figure 5.5 Cyclic voltammograms of a glassy carbon electrode immersed in ChCl:2Urea DES at a range of temperatures from 80 to 125°C and a scan rate of 100 mV/s

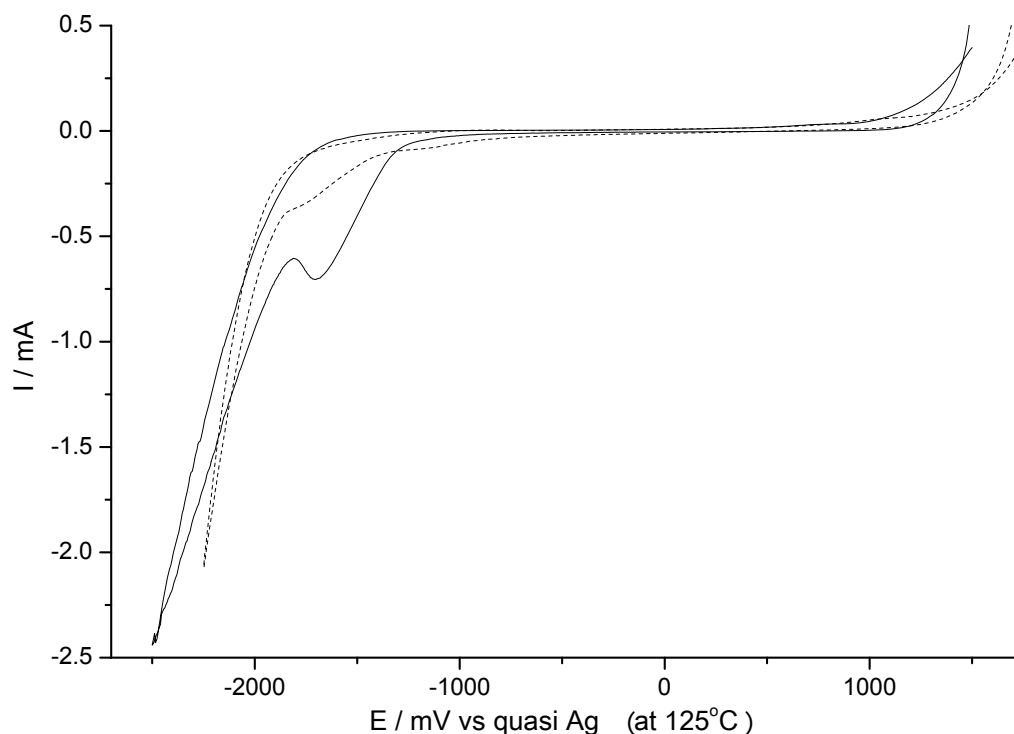


Figure 5.6 Cyclic voltammograms of a glassy carbon electrode immersed in a ChCl:2Urea DES in the presence (solid line) and absence (dashed line) of 0.2 M NbCl₅ at 125°C and a scan rate of 100 mV/s

Replacement of the glassy carbon with copper substrate as the choice of cathode gave different cyclic voltammetric behaviour, as is depicted in **Fig. 5.7**. The solid line indicates the cyclic voltammetric response of a reline system dissolved with 0.2 M NbCl₅, whilst the dashed line points to the NbCl₅-free counterpart. The scan initiated from and returned to the open circuit potential (OCP), whereby only electrochemical reductive process occurs at the copper substrate to prevent its anodic dissolution to complicate reduction current. In the case of the neat reline, it exhibited one reduction current at approximately -1.0 V (vs. Ag) before decomposing itself (from -1.1 V), which may be correlated to the reduction peak observed at -2.0 V in the case of glassy carbon, as is deemed as partial decomposition of ChCl. For the NbCl₅-dissolved reline solution, two distinct reduction currents occur, one of which occurred at -0.6 V with a peak current density of -4 mA/cm², the other which proceeded at -1.25 V for -11 mA/cm² before the cathodic limit initiating

from -1.35 V. To ascertain the underlying process for the reductive currents, potentiostatic deposition trials were performed at three voltages: -0.60, -1.25 and -1.50 V (vs. Ag wire), as is shown in **Fig. 5.8**.

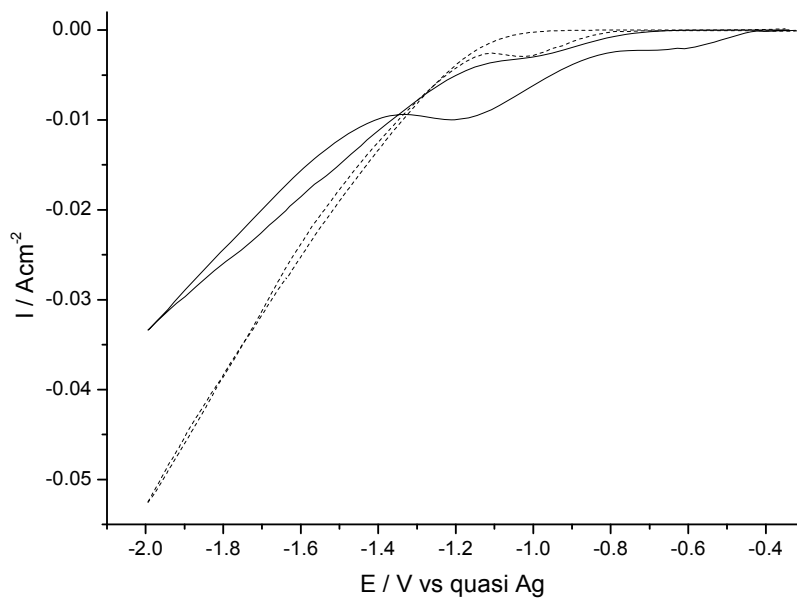


Figure 5.7 Cyclic voltammograms of a Cu substrate (Surface area: 1 cm²) immersed in reline in the presence (solid line) and absence (dashed line) of 0.2 M NbCl₅ at 125°C and a scan rate of 100 mV/s (initiating from the OCP)

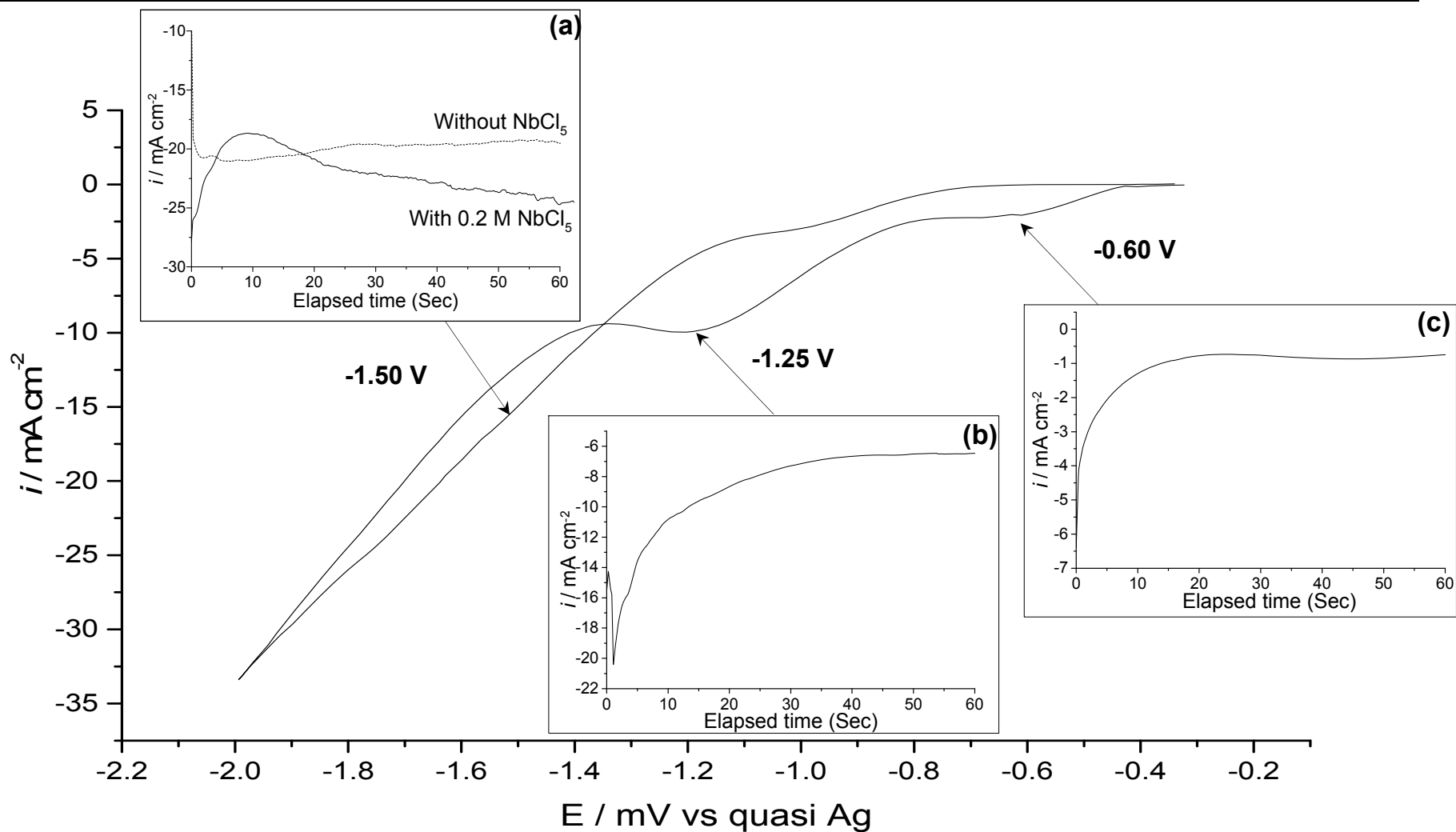


Figure 5.8 A cyclic voltammogram of a Cu substrate (Surface area: 1 cm²) immersed in reline dissolved with 0.2 M NbCl₅ at 125°C and a scan rate of 100 mV/s initiating from the OCP, the insets show the initial 60 seconds of potentiostatic trials carried out at a) -1.50 V (along with its counterpart in the absence of NbCl₅); b) -1.25 V & c) -0.60 V (vs a silver quasi reference electrode) and isothermally at 125°C.

The initial 60 s of the potentiostatic plots at the three voltages for the NbCl₅-dissolved reline at 125°C clearly show nucleation and growth of the deposits, as the initial current quickly decreased to a value and levelled off. This is in contrast to the potentiostatic curve in the neat reline system (**Fig. 5.8 (a)**), where the characteristic initial decrease of the current was absent, signifying that only decomposition of the electrolyte component occurred at -1.5 V. The representative surface morphology of the electropolished copper electrodes before and after potentiostatic deposition trials in reline dissolved with 0.2 M NbCl₅ for 60 min at 125°C is presented in **Fig. 5.9**. In all the three cases, the electrode surfaces did not exhibit significant change after electrolysis. The EDX compositional analysis also did not indicate any Nb content but only Cu, indicating no deposition of the Nb species. The deposition phenomenon inferred from the initial stage of the potentiostatic deposition trials may be attributed to the formation of in adherent and subvalent Nb species at the electrode.

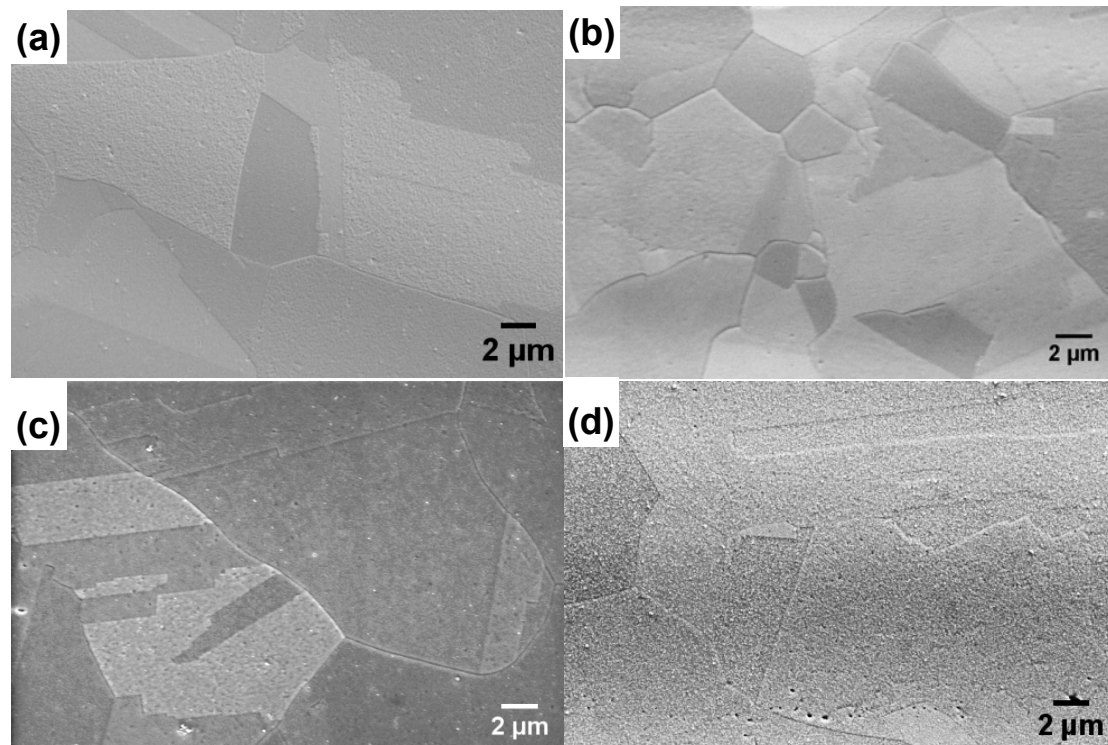


Figure 5.9 Secondary electron images showing the surface morphology of electropolished Cu: a) as-prepared and immersed in reline system dissolved with 0.2 M NbCl₅ following potentiostatic trials for 60 min b) at -0.6 V, c) at -1.25 V and d) at -1.5 V (vs. Ag wire) at 125°C

Prolonged potentiostatic and galvanostatic trials have been carried out at elevated temperatures (ranging from 80 to 120°C) in both reline and ethaline dissolved with NbCl₅, potentiostatically at a voltage of up to -10 V (vs. Nb) or galvanostatically at a current density of up to -300 mA/cm². It was demonstrated that, significant solid Nb reduction products were not obtained on the copper substrate, which is likely to be due to the formation of electrochemically less active oxygen-containing Nb species. A detailed treatment of such a reactive dissolution of NbCl₅ salt in the eutectic solvents will be given in the following chapters. To summarise, the low solubility of Nb halide salts and formation of electrochemically inactive Nb species limited the use of choline-based Type III deep eutectic solvents (e.g. reline and ethaline) for Nb electrodeposition.

5.3 Electrochemical Behaviour of Type III Deep Eutectic Solvents Containing Anodically Dissolved Niobium Metal

It has been demonstrated above that the anodic dissolution of Nb metal is achievable in Type III deep eutectic solvents such as reline and ethaline. As shown in **Figure 5.10**, typical voltammetric behaviour of reline containing anodically dissolved Nb metal exhibited only one reduction current at -1.1 V (vs. Nb wire) before cathodic decomposition at 125°C. Potentiostatic deposition at -1.1 V and even at -1.5 V (beyond the cathodic decomposition) did not see any Nb reduction products formed at the copper substrate surface. Therefore, to drive effective reduction of Nb species, one would need to apply a voltage much negative of the cathodic limit of the common Type III DESs. A complete reduction of Nb species is even complicated by the spontaneous formation of Nb oxo-complexes upon introduction of Nb source, no matter whether it is via direct dissolution of NbCl₅ salt or anodic dissolution of Nb metal.

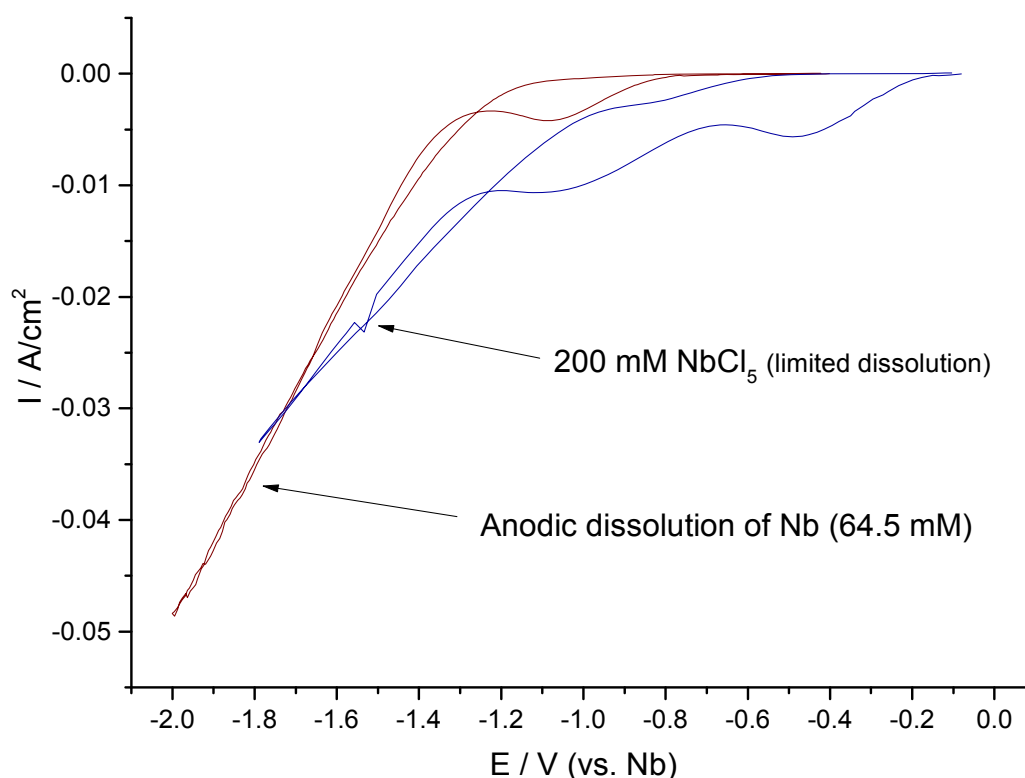


Figure 5.10 Cyclic voltammograms of an electropolished Cu substrate (surface area: 1 cm²) immersed in Reline solution containing anodically dissolved Nb (6 g/L or 64.5 mM) or 0.2 M NbCl₅ at 125°C. Scan rate of 20 mV/s initiating from the OCP

5.4 Electrochemical Behaviour of Type IV Deep Eutectic Solvents Containing Dissolved NbCl₅

Addition of NbCl₅ into either ethylene glycol or propylene glycol gives an exothermic reactive dissolution forming a Type IV eutectic solvent. This reactive dissolution permits high solubility of NbCl₅ in the solution, the details about which will be addressed in **Chapter 6**. The representative cathodic region of the cyclic voltammogram of a mixture of ethylene glycol and NbCl₅ (molar ratio: 3:1) obtained at 100°C is presented in **Fig. 5.11**. The voltammetric response appeared to be largely ohmic, whilst formation of dark-coloured, reduction products were continuous and detached from the copper electrode surface when the voltage was negative of -0.5 V (vs. Nb). The reduction products were collected afterwards and analysed as Nb oxides using EDX analysis. This suggests that the Nb reduction proceeded by the formation of

inadherent Nb oxides at potentials of up to -2.5 V. Galvanostatic deposition trials at current densities up to 300 mA/cm² for periods up to 30 min did not produce any adherent Nb species on the copper substrate surface. A replacement of the ethylene glycol with propylene glycol gave similar voltammetric response and reduction products.

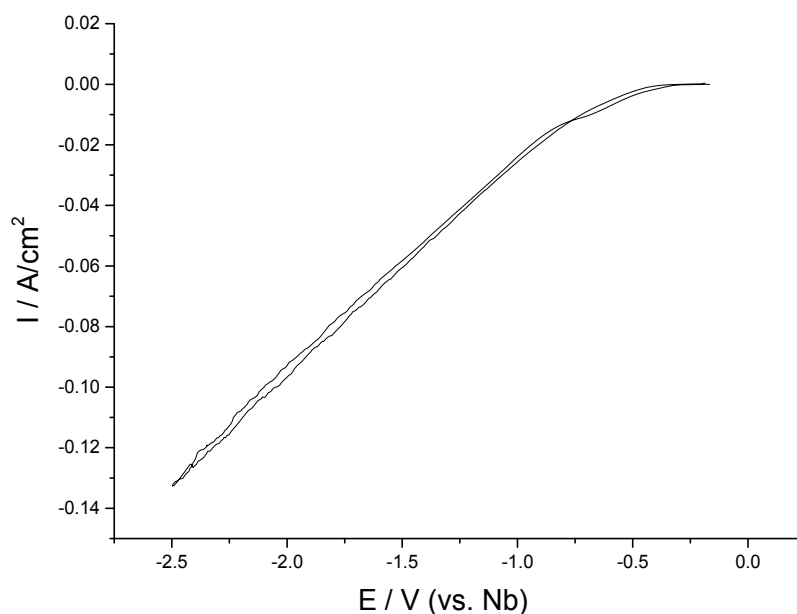


Figure 5.11 Cyclic voltammogram of an electropolished Cu substrate (surface area: 1 cm²) immersed in a mixture of 3ethylene glycol-1NbCl₅ at 100°C at a scan rate of 20 mV/s initiating from the OCP

5.5 New Paradigm for Electroplating Cell Design

5.5.1 Instability of Platinised Titanium Anode & Its Replacement

Potentiostatic trials have been carried out on an electropolished Cu electrode immersed in reline with and without dissolved 0.2 M NbCl_5 at -1.5 V vs. Ag and at 110°C for 1 hr. The morphological and compositional information of the Cu substrate surface after electrolysis is shown in **Fig. 5.12**. In the case with NbCl_5 , nano-crystalline, Pt-rich nodules were found on the Cu surface, which points to the possibility of the partial dissolution of the platinised titanium counter electrode. This is in contrast to the case without NbCl_5 addition, where no significant deposition occurred (**Figure 5.12 (a)**). The formation of Pt-rich deposits may be attributed to the dissolution of Pt from the anode as imposed by the highly oxidising NbCl_5 at high temperatures, followed by the discharge of Pt cations on the Cu surface.

Counter electrode reactions in ILs are rarely reported in the literature. Platinised Ti electrodes have been extensively used as inert CEs for aqueous systems; however, their stability at high applied current densities and high temperatures has not been testified in ILs. The present results indicate their inert chemical reactivity was compromised in strong Lewis acidic solution like reline dissolved with NbCl_5 at elevated temperatures and high applied voltages. Besides, as platinised Ti would be subjected to oxygen evolution in a DES with a certain amount of water uptake, it may be a potential source for oxygen gas which significantly affects the metal speciation in the electrolyte.

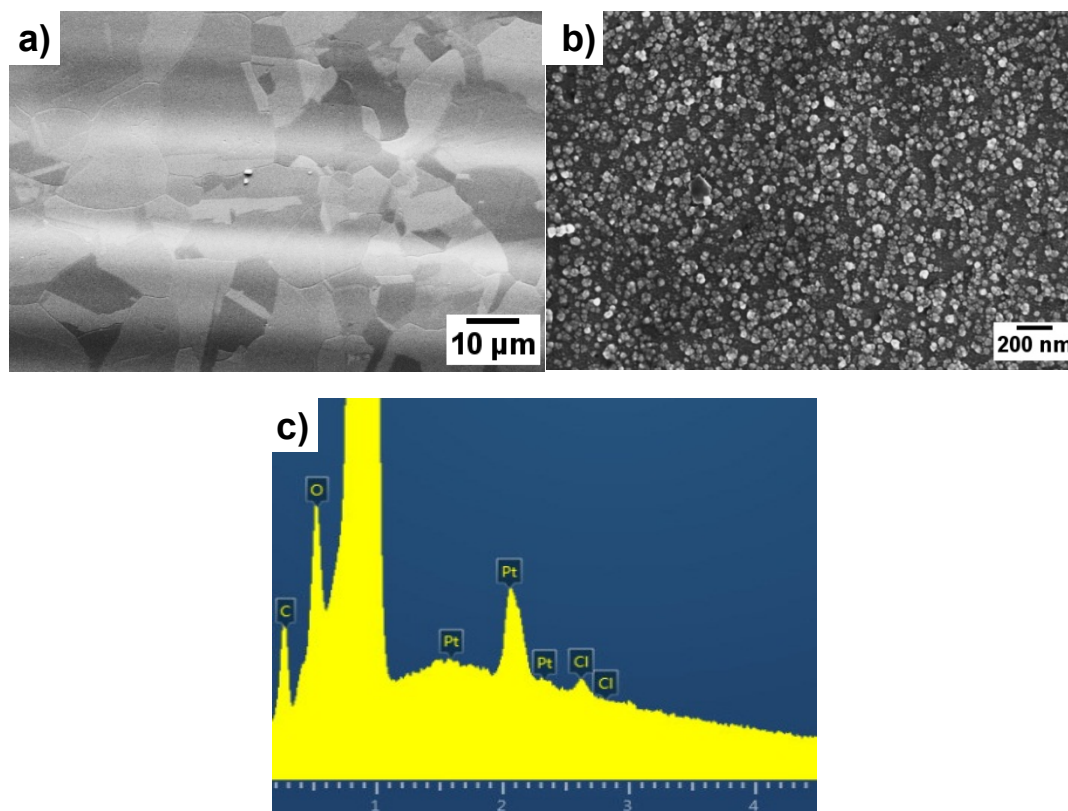


Figure 5.12 Secondary electron images and in-lens image showing the surface of electropolished Cu immersed in reline a) without and b) with 0.2 M NbCl_5 following a potentiostatic trials at -1.5 V vs. Ag at 110°C for 1 hr and corresponding enlarged X-ray spectrum c) showing co-deposited Pt content

A graphite rod has been used to replace the platinised Ti as the CE due to its excellent chemical inertness and high temperature property. Its major drawbacks, arising from its loose structure and presumably consequential poisoning of the electrolyte, might have resulted in the accelerated degradation of the IL and corrosion of the Cu substrate (also reported in [5.3]), as shown in **Fig. 5.13** and **Fig. 5.14**, respectively. Nb metal foils have, therefore, been used as anodes to prevent cross-contamination.

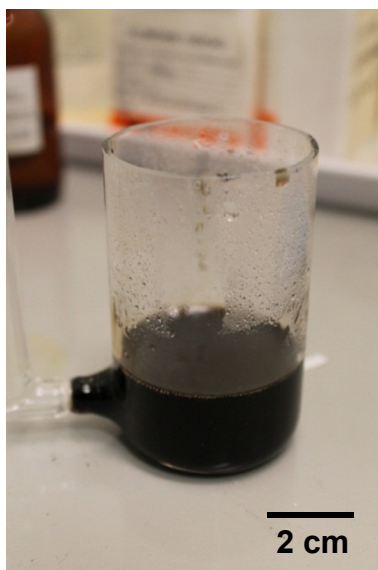


Figure 5.13 Photograph showing more viscous and dark-coloured Reline solution resulted by the 'poisoning' of loosely structured graphite CE

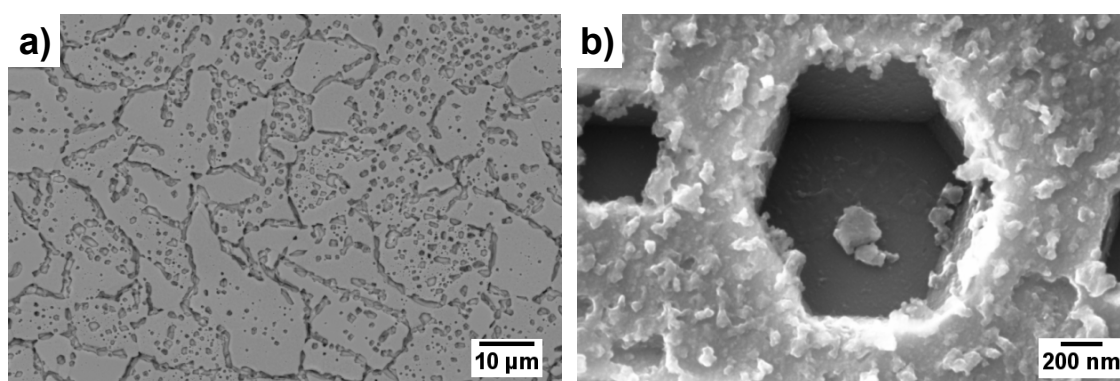


Figure 5.14 a) BSD and b) In-lens images of a Cu substrate surface following the electrolysis in Reline dissolved with 5g/L Nb dissolved at -1.8 V (vs. Nb wire) and at 200°C for 2 hrs suggesting polyhedral voiding imposed by graphite counter electrode

5.5.2 Instability of Silver Wire Reference Electrode & Its Replacement

The use of a silver wire quasi reference electrode that works through the presence of oxide compounds on the metal surface has been proven reliable in DESs [5.4]. The present study indicates that, the Ag wire was also subjected to partial dissolution when used in reline at high temperature as Ag-rich deposits were found on the Cu surface after electrolysis (**Fig. 5.15**). A Nb wire has been adopted as a stable reference electrode [5.5] to replace the Ag wire.

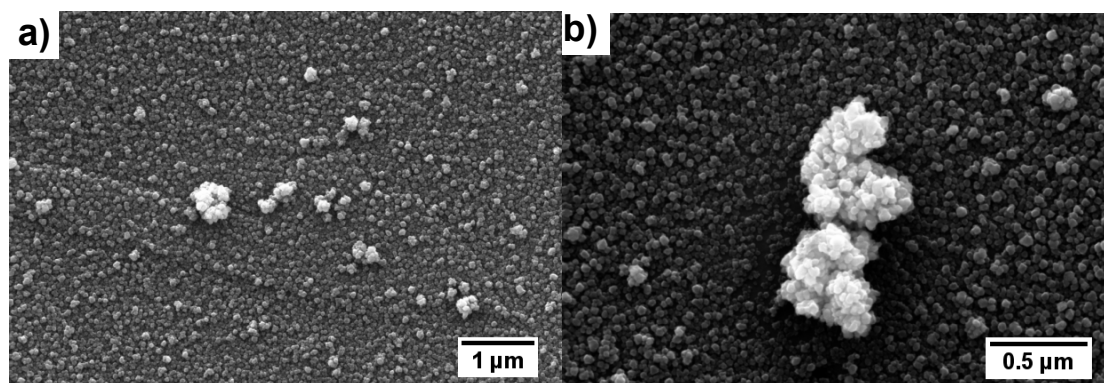


Figure 5.15 In-lens images at different magnifications showing the surface morphology of Ag-rich deposits following electrolysis in Nb dissolved in ChCl:2Urea IL at 150°C for 1 hr

5.6 Ni-Nb Co-deposition

It has become obvious that Nb reduction cannot be made to completion from a Type III or Type IV eutectic solvent using metal source of either NbCl_5 or anodically dissolved Nb. In the present study, an alternative and, perhaps more practical, approach to realising a Nb-based metal finish is to co-deposit Nb with Ni. The potential advantages are twofold, firstly, the catalytic co-deposition effect exhibited by iron group metals such as Ni may induce deposition of Nb metal at much less negative potentials; in addition, Ni, as a conventional solder diffusion barrier has the promise to provide enhanced barrier property when a refractory element like Nb is co-deposited.

Nb-Ni alloy electrodeposits have been fortuitously obtained in a reline 'solution' anodically dissolved with ca. 6 g/L (64.5 mM) Nb metal at 180°C. The typical voltammetric behaviour of the solution at this temperature is presented in **Fig. 5.16**, from which a potential of -2.2 V (vs. Nb) was selected for potentiostatic trials based on the tradeoff between sufficiently negative electrolysis potential and limited cathodic breakdown. The initial potentiostatic curve (of 15 s) is presented in **Fig. 5.17**, indicating nucleation and growth mechanisms. The surface morphology of the deposits is presented in **Figure 5.18** indicating a nano-crystalline structure and an essentially full coverage of the copper

substrate, with some nodular features discretely distributed which were faster growing spots during electrodeposition. **Figure 5.19** shows the corresponding X-ray spectrum, which suggests a high Nb metal percentage in the deposit (ca. 35 wt%), even though significant amounts of Ni (ca. 52 wt%) and O content (13 wt%) were also detected. The co-deposited Ni content may be attributed to the contamination of the electrolyte arising from high temperature corrosion of the Ni-electroplated crocodile clips (confirmed with EDX analysis), as dark green coloured dew (presumably dissolved Ni(II) ions) was observed from the clip surface and possibly flowed back to the electrolyte. The Ni content in bath is impossible to ascertain due to the accidental nature of its presence, yet may not be significantly high given that the electrolyte was not coloured dark green. Provided that the notably high Nb content in the Ni-Nb alloy deposit, it was suspected that, the co-deposition of Ni might have a catalytic effect on the deposition of Nb. Therefore, such a strategy of Ni-Nb co-deposition will be investigated further in **Chapter 6**.

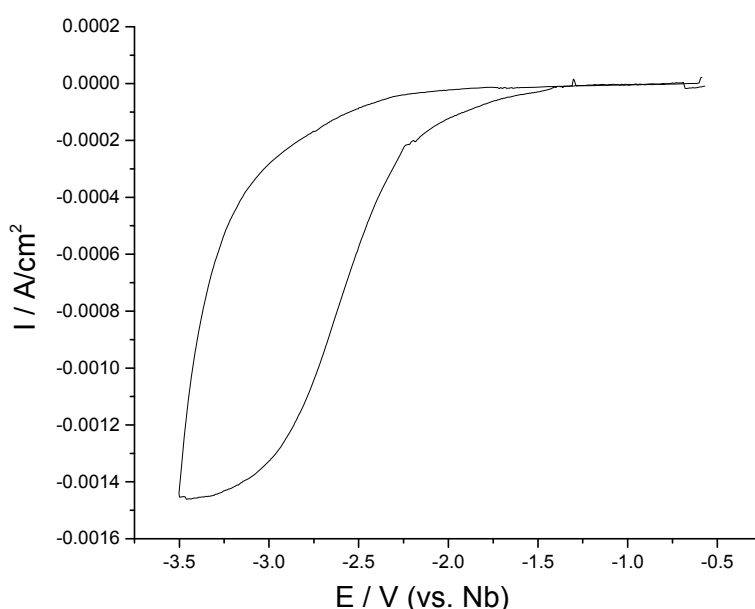


Figure 5.16 A cyclic voltammogram of an electropolished Cu substrate (surface area: 1 cm²) immersed in a reline solution anodically dissolved with 6 g/L Nb at 180°C and a scan rate of 20 mV/s initiating from the OCP

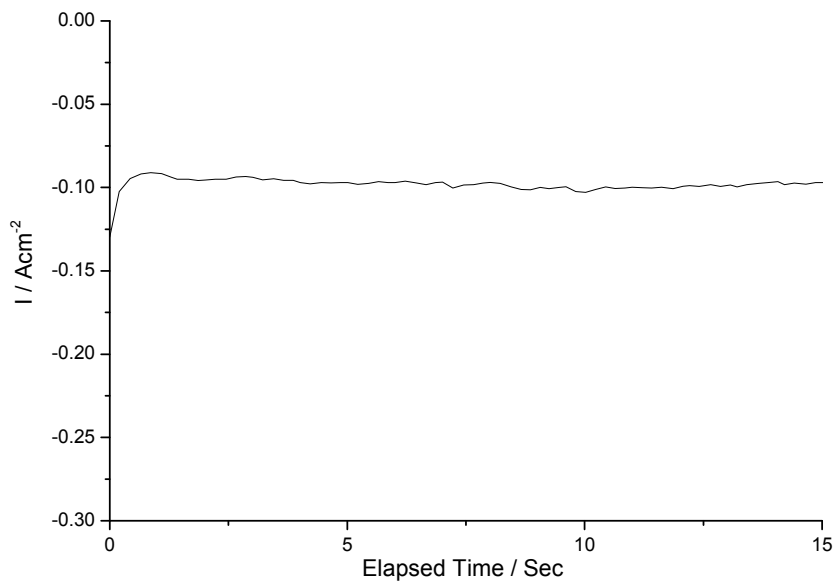


Figure 5.17 Initial 15 seconds of a potentiostatic trial carried out at -1.80 V (vs. a Nb wire reference electrode) at 110°C from the solution giving the voltammetric response shown in Figure 5.16

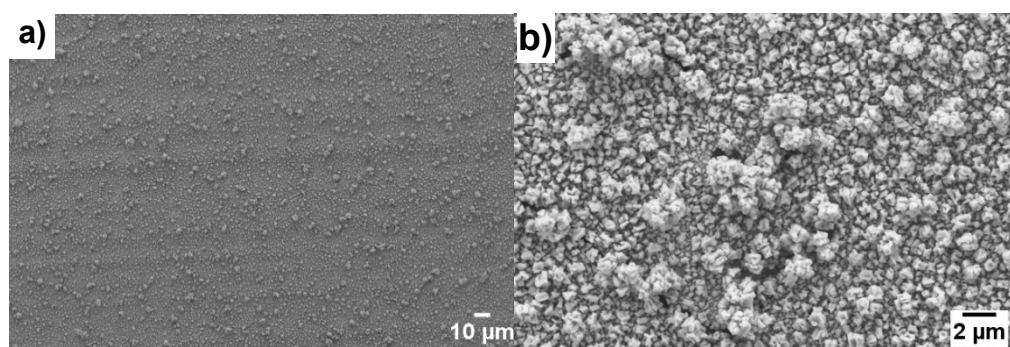


Figure 5.18 Secondary electron images showing the surface morphology of Ni-Nb deposits obtained following the electrolysis in Reline anodically dissolved with 6 g/L Nb (with an uncertain amount of Ni ions accidentally introduced) at 180°C for 1 hr

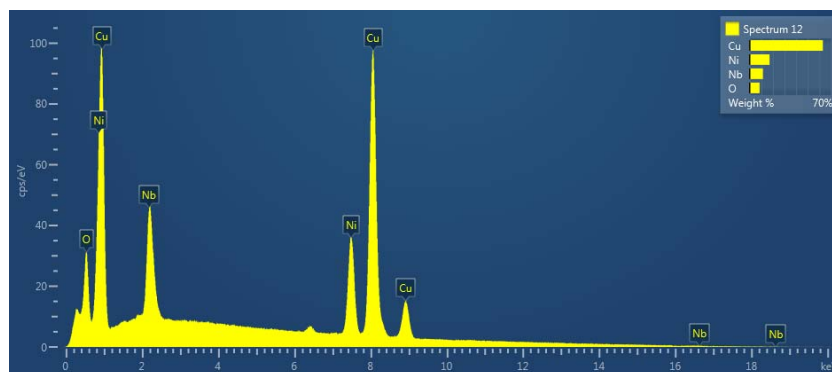


Figure 5.19 Area-scan X-ray spectrum showing the composition of Ni-Nb alloy deposit on an electropolished Cu substrate from Figure 5.18 (b)

5.7 Summary

In this chapter, the electrochemistry of Nb in common Type III deep eutectic solvents (e.g. reline and ethaline) and Type IV off-eutectic solvents such as (urea:NbCl₅ mixture and ethylene glycol:NbCl₅ mixture) has been investigated, with respect to the solubility and electrochemical behaviour of the metal precursor, electrolyte workability and electrode stability. Type III DESs such as reline and ethaline gave relatively low solubility of NbCl₅ and could not allow significant complete reduction of Nb species due to the excessive cathodic breakdown. Adherent Nb reduction products were seldom produced from these electrolytes, no matter whether NbCl₅ or anodically dissolved Nb was used as the metal precursor. Type IV off-eutectic solvents such as NbCl₅:ethylene glycol mixtures permitted high solubility of NbCl₅ and yielded in adherent Nb oxide reduction products upon electrolysis. The high temperatures (above 100°C) experienced in the use of these solutions require a paradigm change with respect to electroplating cell design, where the conventional inert anode like platinised Ti and untreated graphite electrode and reference electrode like Ag wire become dissolved, releasing foreign metal ions into electrolytes and thereby poisoning the reduction process. Nb metal has proved reliable as an anode and reference electrodes to prevent contamination. Finally, an alternative approach to producing Nb-based metal finishes, i.e. Ni-Nb co-deposition, has been briefly reported, which will be further investigated in the following chapters.

5.8 References

- [5.1] Tumanova, N., Volkov, S., Kochetova, S., Triphonova, T., & Buryak, N. (2003). *Journal of Mining and Metallurgy B: Metallurgy*, 39(1-2), p. 69.
- [5.2] Yue, D., Jing, Y., Yao, Y., Sun, J., & Jia, Y. (2012). *Electrochimica Acta.*, 65, p. 30.
- [5.3] Chirkov, D. 'Attempts for the electrodeposition of niobium from ionic liquids', (2009) Master's thesis, Universita Degli Studi Di Padova, Italia.
- [5.4] Endres, F., MacFarlane, D., & Abbott, A. (Eds.) (2008) *Electrodeposition*

from ionic liquids, Wiley-VCH.

[5.5] Baizeng, F., Xinyu, L., Xindong, W., & Shuzhen, D. (1998). *Journal of Electroanalytical Chemistry*, 441(1), p. 1.

Chapter 6

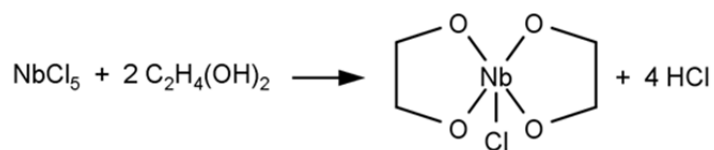
Electrodeposition of Ni-Nb from Type IV Eutectic Solvent Derivatives

In the previous chapter, the electrochemical reduction of Nb species in both Type III and Type IV eutectic solvents and their derivatives was examined. Through a series of electrolyte formulation modifications, a possible strategy for the production of effective Ni-Nb-based electrodeposits has been identified. This chapter describes the evolution of the electrodeposition process through control over bath formulation and deposition parameters. The effect of electrolyte constituent (metal salts and NaBH_4) concentrations and cathodic current density on the surface morphology, composition and thickness of the deposits is investigated.

6.1 Effect of Major Electrolyte Constituent

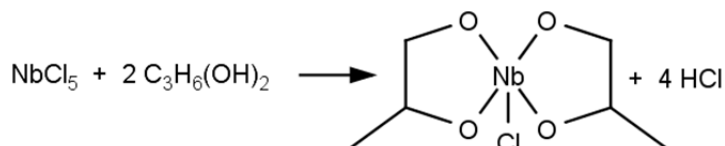
A Type IV eutectic solvent system combining NbCl_5 (metal salt) and a diol (hydrogen bond donor) was selected as the electrolyte baseline due to relatively high electrical conductivity and low viscosity. Off-eutectic compositions with reduced Nb salt contents were normally adopted as relatively low metal concentrations appeared to yield more uniform electrodeposits. Both ethylene glycol (EG) and propylene glycol (PG) have been investigated as the diol candidate. The reactive dissolution of NbCl_5 in either EG or PG forms niobium chloro-glycoxides following **Equations 6-1 & 6-2**, respectively [6.1],

With EG,



Equation 6-1

With PG,



Equation 6-2

The glycoxide ligands behaved as a strong Lewis base, competing with Cl for Nb. As a volatile side product, HCl yielded from the reactive dissolution caused slow effervescence of the solution. A certain amount of HCl is also expected to be dissolved in the glycol due to formation of intramolecular hydrogen bonding between H from HCl and the hydroxyl (–OH) group from glycols [6.2]. Also, it is noteworthy that the Nb complexes formed are likely to be polynuclear and still to contain Cl ligands. The former is, again, owing to the strong Lewis basicity of the glycoxide ligands which tend to bridge metal nuclei, whilst the latter is due to the high electropositivity of the Nb nucleus, where glycolysis can hardly progress to completion [6.3].

6.1.1 Ethylene Glycol-based Solutions

Galvanostatic deposition trials in neat $x \text{ EG}-(1-x) \text{ NbCl}_5$ solutions ($x > 0.7$, mole fraction) at 100°C saw formation of inadherent and black-coloured reduction products upon copper cathodes. This occurred at cathodic current densities exceeding 10 mA/cm^2 . The reduction products were then collected and identified as nonstoichiometric and chloride-free niobium oxides using EDX analysis. This signifies that the electrochemical reduction of Nb species was complicated by the formation of oxides, which exhibit poor adhesion to the

Cu electrode. It is noteworthy that electrolysis at 100°C tended to instigate gelation of the bath normally after 30 minutes, which may be attributed to formation of a macromolecular network of electrochemically formed niobium oxides. It was, however, found that, the bath gelation did not occur, either by heating without electrolysis, or by utilising a lower electrolysis temperature (i.e. 70°C) even after 7 hours. These observations would suggest that the gelation is dependent on both temperature and electrolysis.

Therefore in order to reduce Nb species directly onto a Cu electrode, attempts to introduce either NaBH₄ or NiCl₂ into the electrolyte were made. For NaBH₄, it was hoped that its addition could chemically pre-reduce the Nb species, thereby making their subsequent electrolytic reduction more straightforward. Conversely, NaBH₄ could partially chemically reduce the H⁺ ions generated from the glycolysis of NbCl₅ (**Equation 6-1**), so as to suppress the competing hydrogen evolution during electrolysis. The conventional approach to pH adjustment is to add base to induce neutralisation, which nevertheless is not applicable to the current non-aqueous system as it would generate water, promoting undesirable hydrolysis of the NbCl₅ salt. As was observed, the addition of NaBH₄ into the solution was accompanied by vigorous gas evolution and the emission of white fumes, indicating the possible co-release of HCl with H₂. This phenomenon can be attributed to a dissociation of the HCl solute in the glycol due to reduced proton concentration available for hydrogen bonding. Even though this approach did not seem to facilitate the production of adherent Nb reduction products at the Cu electrode, it has proven an effective way of reducing the proton concentration in the bath and hence become vital to the development of the deposition process, which will be discussed later in **Section 6.3**.

A small amount of NiCl₂ ($n(\text{Nb(V)}) : n(\text{Ni(II)}) = 20:1$ or $30:1$) was added into the electrolyte, in an attempt to facilitate Nb reduction in a way analogous to the

induced co-deposition. The formulation of the Ni-Nb electrodeposition baths is summarised in **Table 6.1**. Upon NiCl₂ additions, the electrolytic reduction products at Cu electrode became uniform and adherent by visual assessment. The representative surface morphology and composition of the electrodeposits derived from the EG-based solution (Bath 1 in **Table 6.1**) is presented in **Figure 6.1**. Three cathodic current densities were applied, 100, 300 & 400 mA/cm², with equal deposition time of 10 min, which is limited by electrolyte gelation. At 100 mA/cm², the features on the Cu electrode surface were submicron or micron in size and hemispherical in geometry. With the current density elevated to 300 mA/cm², the surface features turned into granular shapes, which coincided with a reduction in average dimensions. With a further rise in current density to 400 mA/cm², the deposit morphology became acicular, with a further decrease in the feature dimensions down to a few hundred nanometres.

Table 6.1 Formulations of Ni-Nb electrodeposition electrolytes (g/L (M))

Compounds	Ethylene glycol (EG)	Propylene glycol (PG)	NbCl ₅	NiCl ₂ ·6H ₂ O	NaBH ₄
Bath 1	1113.2 (18.00)	-	484.8 (1.80)	21.30 (0.09)	67.9 (1.80)
Bath 2	-	1036.0 (13.63)	147.2 (0.54)	4.26 (0.018)	20.6 (0.54)
Bath 3	-	1036.0 (13.63)	441.6 (1.62)	12.78 (0.054)	20.6 (0.54)
Bath 4	-	1036.0 (13.63)	441.6 (1.62)	12.78 (0.054)	61.8 (1.62)
Bath 5	-	1036.0 (13.63)	147.2 (0.54)	4.26 (0.018)	41.2 (1.08)
Bath 6	-	1036.0 (13.63)	147.2 (0.54)	4.26 (0.018)	61.8 (1.62)

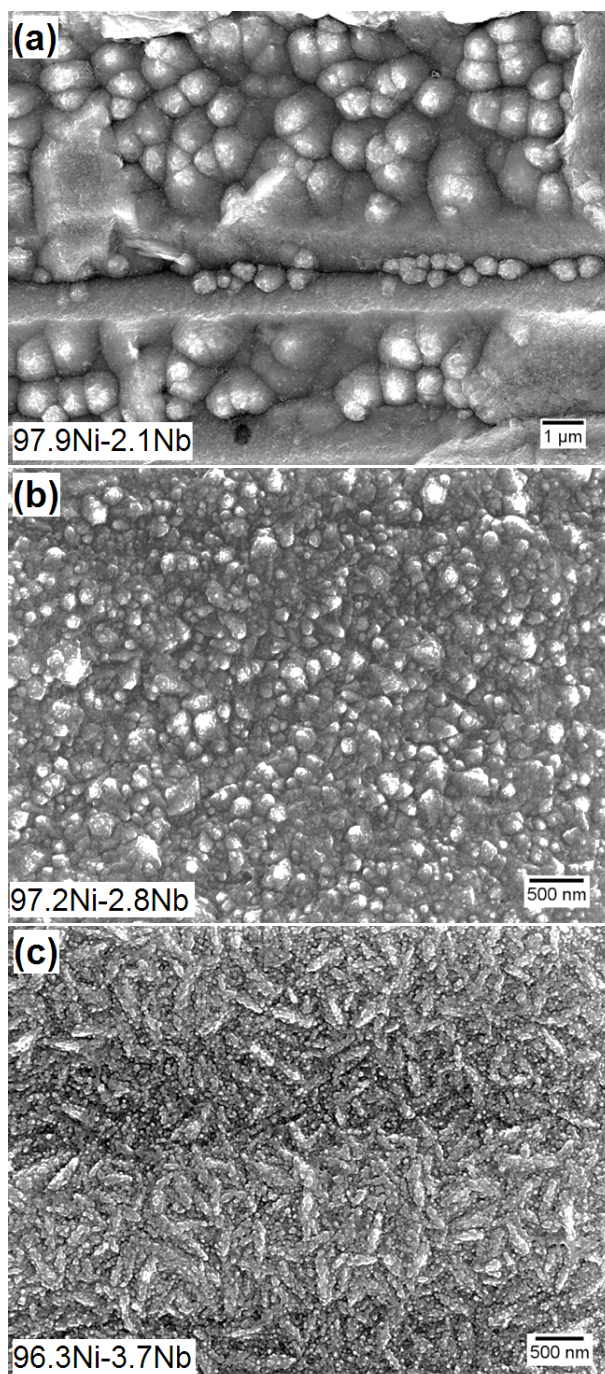


Figure 6.1 In-lens SEM images depicting the representative surface morphology of Ni-Nb coatings deposited from Bath 1 at 100°C & 60 r.p.m. for 10 min at a current density of a) 100, b) 300 and c) 400 mA/cm² with the EDX composition noted (at.%)

The reduction in the deposit feature sizes with increased current density is attributable to more frequent grain nucleation imposed by elevated cathodic overpotential. The deposit composition was measured from area scan at low magnification ($\times 250$) using EDX analysis, for averaging out the composition variations. It was found that, with increasing current density from 100 through

300 to 400 mA/cm², the relative metal percentage of Nb saw a slight increase from 2.1 through 2.8 to 3.7 at.%. The small magnitude of the increment in the co-deposited Nb content suggests that the actual partial current density for Nb deposition, albeit slightly improved with increasing current density, is limited by other cathodic processes such as Ni reduction and hydrogen evolution. The limited bath lifetime owing to gelation, however, proved inhibitive for further investigation of the EG-based system.

6.1.2 Propylene Glycol-based Solutions

The use of an analogous electrolyte formulation replacing EG with PG has proven not only capable of producing Ni-Nb electrodeposits, but importantly has *not* been susceptible to any electrolyte gelation even after 10 hours of electrolysis at 100°C. This may be due to the presence of an additional methyl side group in PG, imposing a steric hindrance effect and thereby lowering the activity for gelation.

Typical surface morphology and compositions of Ni-Nb electrodeposited from a PG-based solution (Bath 2 in **Table 6.1**), at various current densities from 30 to 400 mA/cm², are presented in **Fig. 6.2**. Each case was undertaken with equivalent charge passage of 360 C per cm². In all cases, the resultant electrodeposits were uniform and bright by visual examination. At 30 mA/cm², the deposit surface features were granular, with a maximum feature size of ca. 1 μm, and with an overall composition of 97.3Ni-2.7Nb (at.%). With a rise in the current density to 50 mA/cm², the feature size became smaller (ca. 230 nm) on average, with a much narrower size distribution. The Nb content of the deposit was increased to 4.2 at. %. With the current density elevated to 100 mA/cm² and further to 150 mA/cm², the deposit surface morphology became much finer and smoother. A magnified view of the deposit surfaces is depicted in **Fig. 6.3**, both demonstrated a slightly acicular morphology. At the edge of the specimens deposited at 150 mA/cm² (**Fig. 6.3(c)**), nodules were observed

taking a hemi-spherical shape. Such morphology variations can be ascribed to elevated current densities at the sample edge during deposition. The Nb contents of the deposits at 100 and 150 mA/cm² were 8 and 6.4 at. %, respectively. As the current density was further increased to 300 and 400 mA/cm² (**Fig. 6.2 (e-f)**), the sub-micron nodular features were retained, analogous to those acquired at 30 and 50 mA/cm². The metal percentage of Nb was correspondingly increased from 13.4 to 14.3 at.%. Therefore, it is established that, increasing current density generally leads to reduced deposit surface feature size and increased Nb content, which is in line with those observed from the EG-based counterparts.

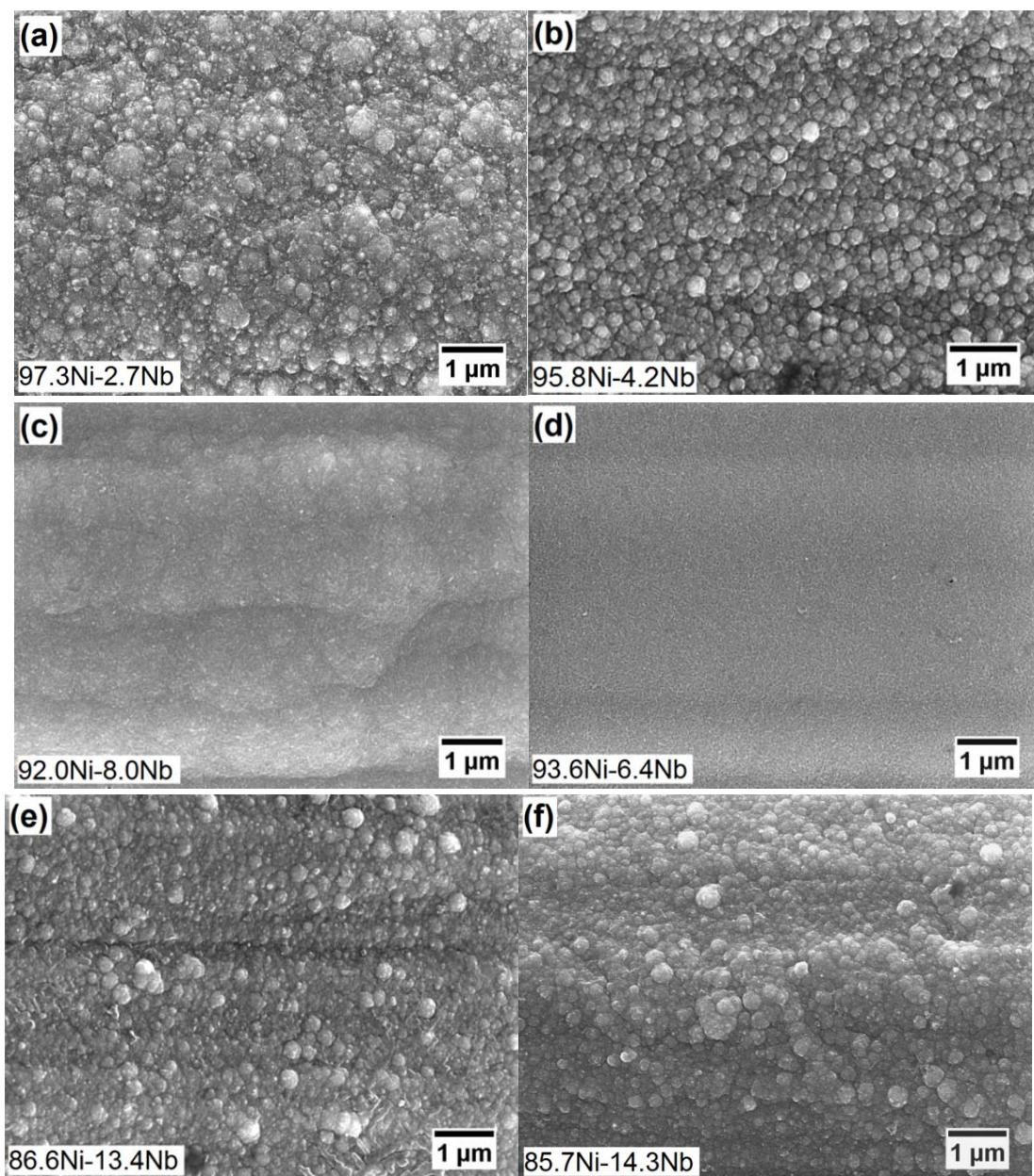


Figure 6.2 In-lens SEM images showing the representative surface morphology of Ni-Nb electrodeposited from Bath 2 at 100°C & 240 r.p.m. at a current density of a) 30, b) 50, c) 100, d) 150, e) 300 and f) 400 mA/cm² with an equivalent charge passage of 360 C per cm² with the EDX composition noted (at.%)

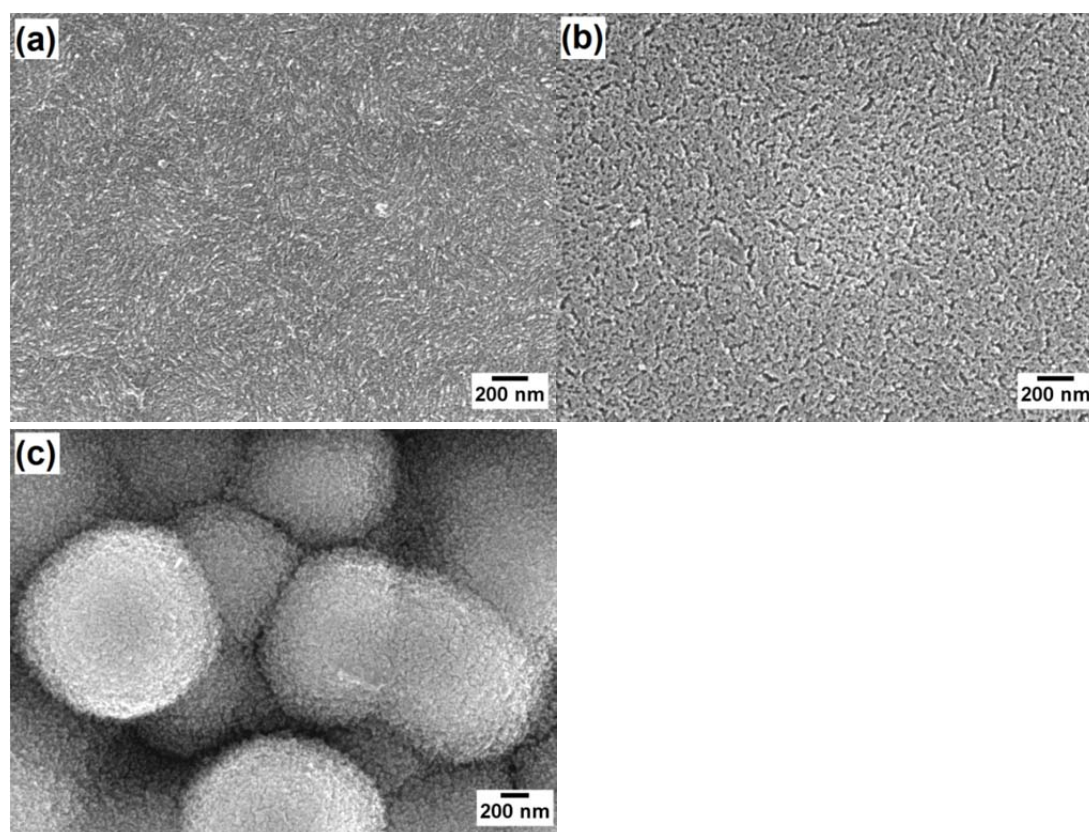


Figure 6.3 High magnification in-lens SEM images illustrating the representative surface morphology of a) the centre of the Ni-Nb coating shown in **Fig. 6.2 (c)**, and the b) centre and c) edge of the Ni-Nb coating shown in **Fig. 6.2(d)**, electrodeposited from Bath 2 at a) 100 and b-c) 150 mA/cm²

Therefore, it has been demonstrated that the introduction of small amounts of nickelous ions (Ni^{2+}) (1:30 relative to that of the Nb^{5+} ions) into the glycol-based baths is able to facilitate the co-deposition of Nb species, which otherwise would end up in the formation of in adherent reduction products. This effect may be suggested from the initial stage of electrodeposition when the copper electrode surface had not been entirely covered by electrodeposits. **Figure 6.4** depicts the morphology and elemental mapping of a copper electrode following electrolysis at 80 mA/cm² for 600 s. The deposit surface features were observed to be nodular and submicron-sized, coalescing into islands. The predominance of nodular features is attributable to the use of Cl ligands, which encourage formation of large numbers of small nuclei. On these nodular features, the concentrations of Ni and Nb were concurrently elevated, as is suggested from X-ray mapping. EDX point analyses suggested that the

region adjacent to the three-dimensional, nodular features also contained Ni and Nb, albeit at much lower contents (< 4.0 at.%). These signify that, the electrodeposition initiated with the formation of a thin and continuous layer of Ni-Nb (up to several monolayers), which was followed by nucleation and growth of individual nodules, characteristic of the Stranski-Krastanov growth process [6.4]. However, it still remains unclear in terms of whether the codeposited Nb content arises from certain mechanisms similar to induced co-deposition by Ni, or simply were in adherent Nb reduction products being incorporated in the growing Ni structure. This aspect will be treated later through observations from scanning transmission electron microscopy.

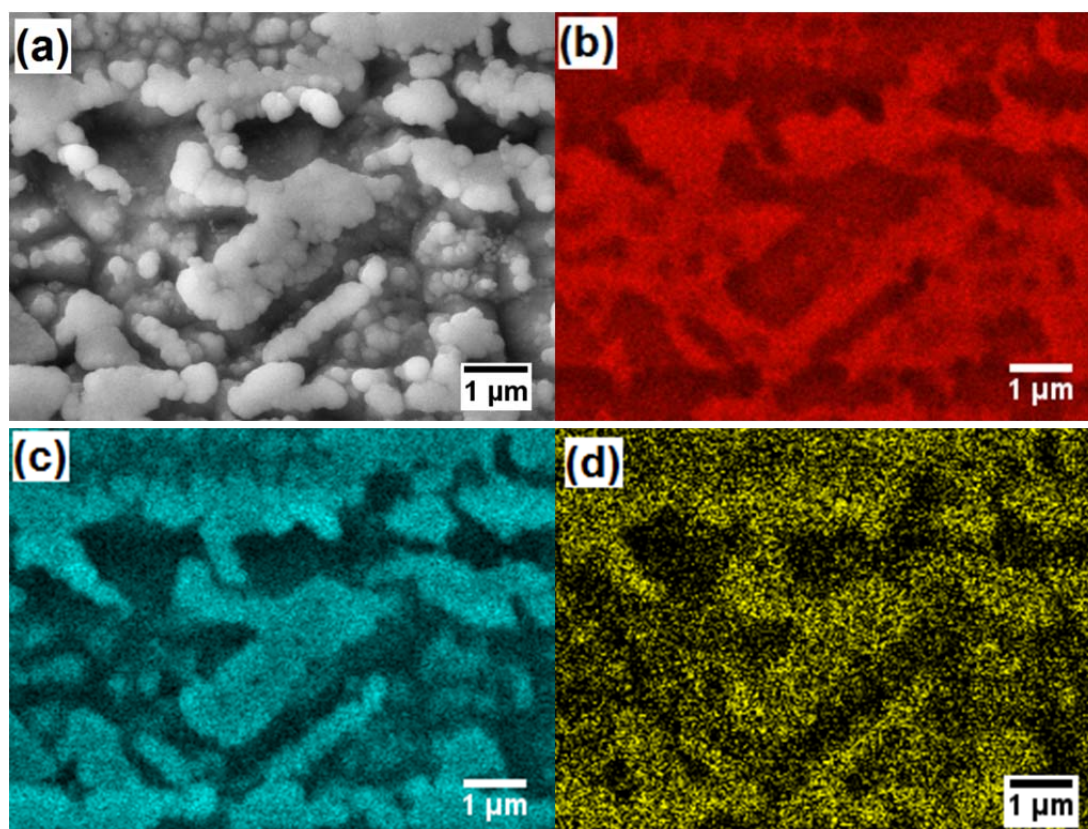


Figure 6.4 Secondary electron image a) illustrating the representative surface morphology of 94.3Ni-5.7Nb deposited from Bath 2 at 100°C & 240 r.p.m. at 80 mA/cm² for 10 min, with the corresponding X-ray maps of b) Cu K α , c) Ni K α and d) Nb L α

6.2 Threshold Deposit Thickness

The thickness of the Ni-Nb electrodeposits has been examined using metallographic cross sectioning. It was seen that the deposits from Bath 2 were generally uniform and compact, with a gradual and approximately two-fold increase from the centre to the edge of the sample. The central deposit thickness for specimens obtained at various current densities is presented in **Fig. 6.5**. A current density of 30 mA/cm² gave a thickness of ca. 2.5 μm, which decreased down to 1.1 μm with the current density increased to 50 mA/cm² with equivalent charge of 360 C/cm² passed. A layered structure in parallel with the substrate interface was evident (See **Fig. 6.5(b)**). With the current density elevated to 100 mA/cm², the deposit thickness increased back to approximately 2 μm, but again decreased to ~1.1 μm at 150 mA/cm². The discontinuity in the decreasing deposit thickness with increasing cathodic current density at 100 mA/cm² may be attributed to a simultaneous transition in the coating surface morphology from the granular to finer acicular. At greater current densities (300 & 400 mA/cm²), the deposit thicknesses were less than 500 nm, albeit the Nb content being elevated. Therefore, the highest current efficiency amongst the various current densities investigated was ca. 2% obtained at 30 mA/cm². Such poor current efficiencies may intuitively be ascribed to excessive hydrogen evolution as a dominant cathodic side reaction. However it is noteworthy that, by reducing the charge passage to a half (180 C/cm²), the Ni-Nb deposits gave comparable morphology, compositions and thickness. It is reasonable to surmise that a threshold coating thickness exists for the present Ni-Nb electrodeposition. It would be interesting to see how the deposition proceeds beyond the limiting coating thickness.

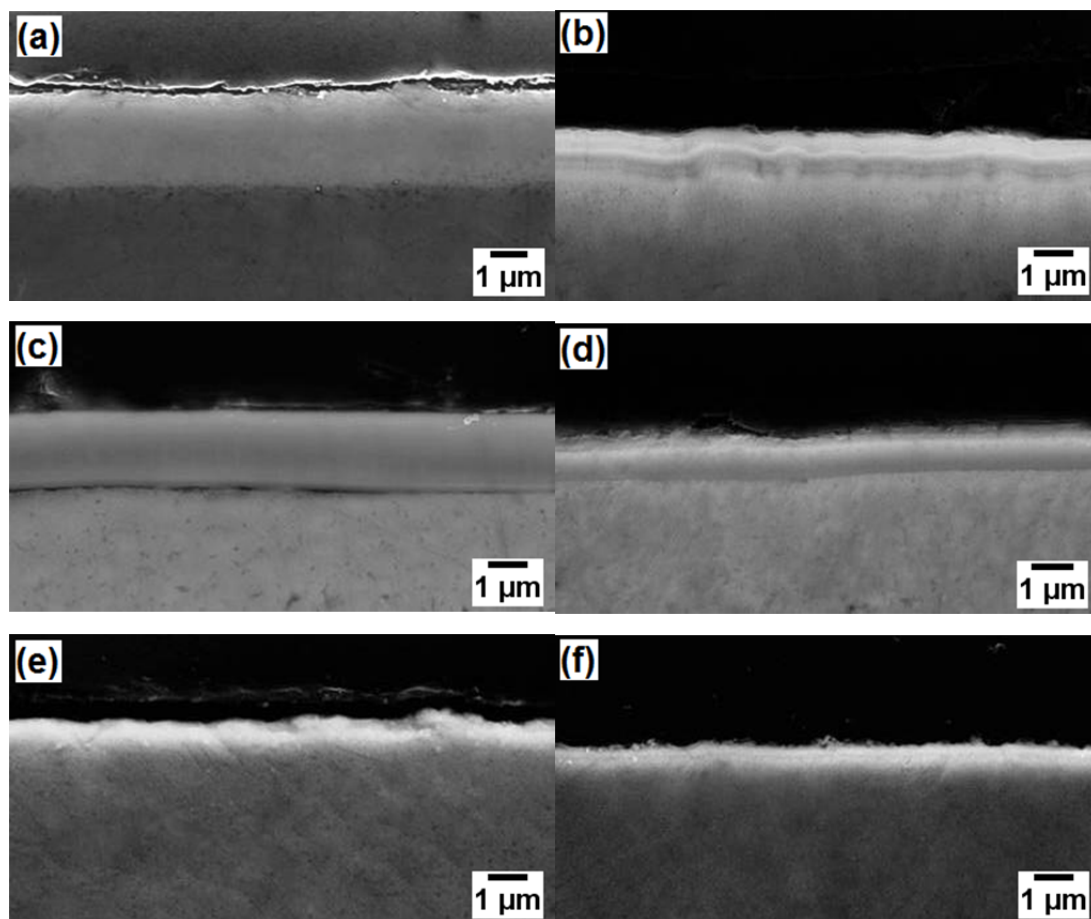


Figure 6.5 Secondary electron images presenting the central cross-section of Ni-Nb deposited from Bath 2 at 240 r.p.m. and 100°C at a) 30, b) 50, c) 100, d) 150, e) 300 and f) 400 mA/cm² with an equivalent charge of 360 C per cm² passed

It is fortunate that a number of electrodeposited specimens still retained certain features even after thorough rinsing, which may answer how the deposition evolves when a threshold deposit thickness has been reached. **Figure 6.6** illustrates the effect of deposition time on the surface morphology of the Ni-Nb coatings from a PG-based solution containing 0.045 M NiCl₂, 1.20 M NbCl₅ and 1.20 M NaBH₄. At 10 min, the Ni-Nb electrodeposit was generally uniform and nodular, with slight thickness variations, seemingly contrasted by the grain boundary of the underlying Cu substrate. This is thought to be attributed to the epitaxial growth following substrate grain orientations. With the deposition time increased to 20 min, the three-dimensional, nodular features have mostly coalesced to form more uniform and smoother surface. However, on the existing uniform deposit surface, discrete features with high aspect ratios were

distributed following irregular web geometry. At 30 min, the discrete crystals had developed into skeleton-like and hollow structures. In contrast to the underlying uniform deposits, these three-dimensional features developed in the later stage of electrodeposition can largely be rinsed off using distilled water, indicating poor adhesion to the bulk deposit.

A cross-sectional view of these deposits is presented in **Fig. 6.7**. It was found that the deposition proceeded only in a uniform and adherent fashion up to a certain thickness before 20 min. At 20 min, it had been replaced by localised crystal growth, which was then further developed into three-dimensional, inadherent and skeleton-like structures. From both X-ray mapping (e.g. Nb L α map in **Fig. 6.7 (c)**) and compositional point analysis, it was observed that the Nb content was generally elevated on the skeleton structures. It is thus speculated that, the partial current density for Nb reduction may be being elevated during the electrodeposition. It is until a certain partial current density that the uniform and adherent deposition is replaced by the formation of localised and inadherent crystal growth, despite the elevated Nb contents.

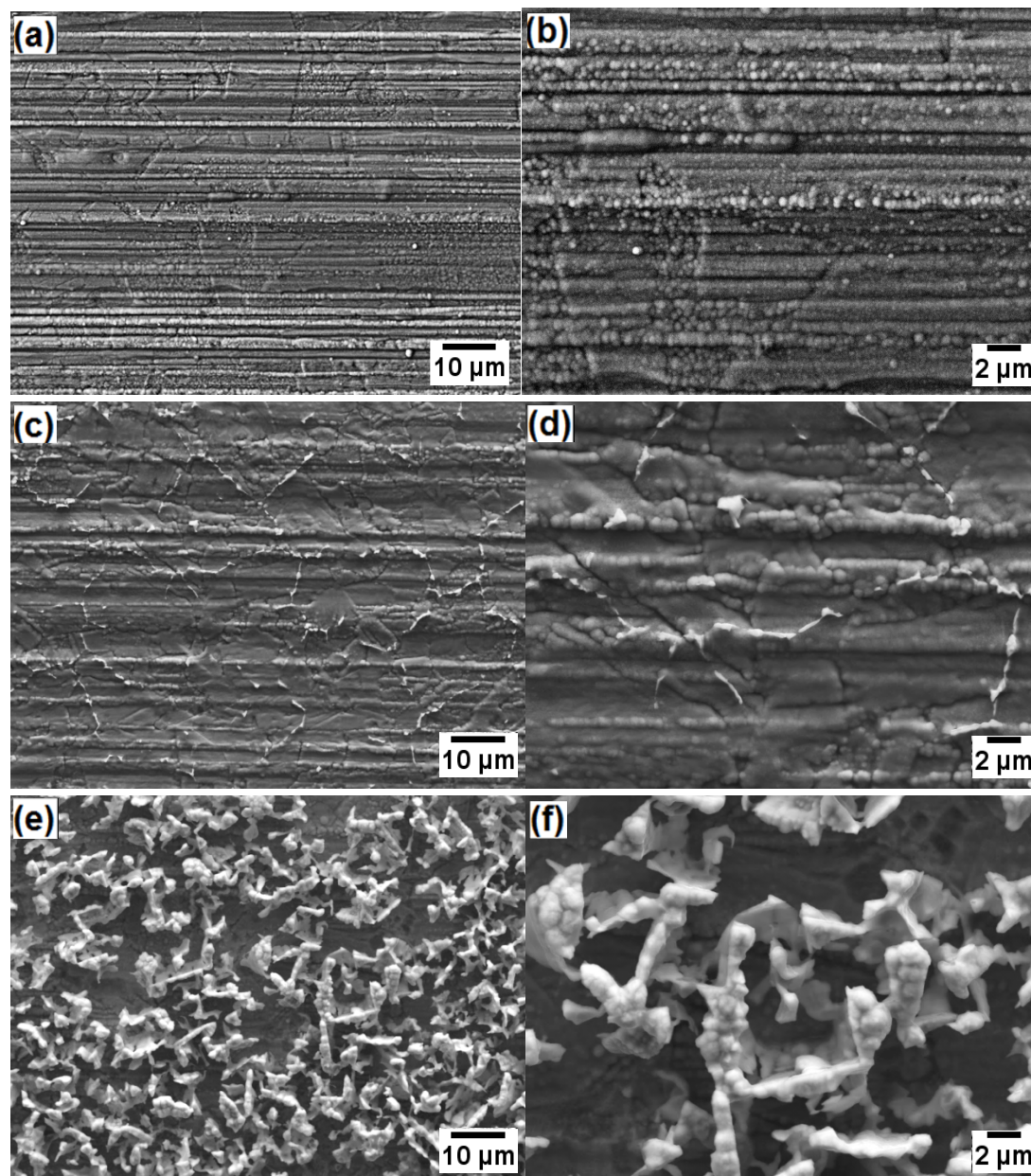


Figure 6.6 Secondary electron images illustrating the representative surface morphology of Ni-Nb deposited from a PG-based solution at 100°C and 200 mA/cm² for a-b) 10 min, c-d) 20 min and e-f) 30 min (parallel ridges probably due to rolling lines present on the underlying copper substrate)

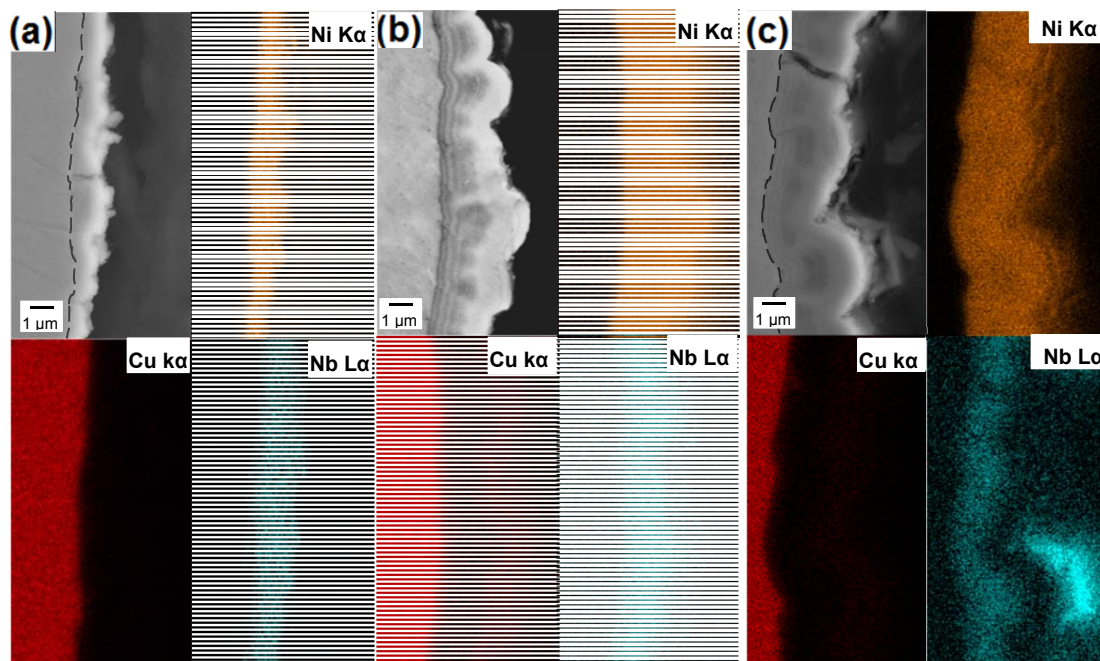


Figure 6.7 Secondary electron images and the corresponding X-ray maps illustrating the representative cross-sections of Ni-Nb deposited from a PG-based solution at 100°C and 200 mA/cm² for a) 10 min, b) 20 min and c) 30 min

6.3 Effect of Metal Ion Concentrations in Solutions

Metal ion concentration is paramount when designing an ionic electroplating system, as it affects both the kinetics and thermodynamics of metal ion reduction, and hence governs the microstructure and properties of the resultant electrodeposit [6.5]. This is especially true for the present system, as the viscosity and mass transport of the electrolyte is directly related to the concentration of the major ionic species, anionic niobium chloro-glycoxides, which arise from glycolysis of NbCl₅.

To establish a metal ion concentration range for the production of effective Ni-Nb electrodeposits, Bath 3 (See **Table 6.1**) has been developed using a PG-based bath formulation analogous to that of Bath 2, although with *tripled* Ni²⁺ and Nb⁵⁺ ion concentrations. **Figure 6.8** depicts the typical surface morphology and composition of Ni-Nb electrodeposits produced from Bath 3, whilst cross-sectional views are illustrated in **Fig. 6.9**. From both top and cross-sectional view, it was evident that the uniformity of the Ni-Nb deposits

was much less than those obtained from the low metal ion concentration counterpart bath (Bath 2). The deposition protocol was repeated with Bath 4 (**Table 6.1**) with equally tripled NaBH_4 content. The non-uniform coating morphology was retained, which rules out the possible effect of insufficient NaBH_4 content ($n(\text{NaBH}_4):n(\text{NbCl}_5) = 1:3$ for Bath 3 as compared to 1:1 for Bath 2). It is thus speculated that the localised development of Ni-Nb electrodeposits may be related to high metal ion concentration in the solution. Ionic liquids with higher metal chloride concentrations, such as those based on Type I and Type II eutectics, have been suggested to be more prone to dendritic and powdery deposition [6.5].

These data suggest that, bright and compact Ni-Nb based thin films could be electrodeposited on a Cu substrate from a non-aqueous, $\text{NiCl}_2:\text{NbCl}_5:\text{PG}$ double salt system at relatively low metal concentrations.

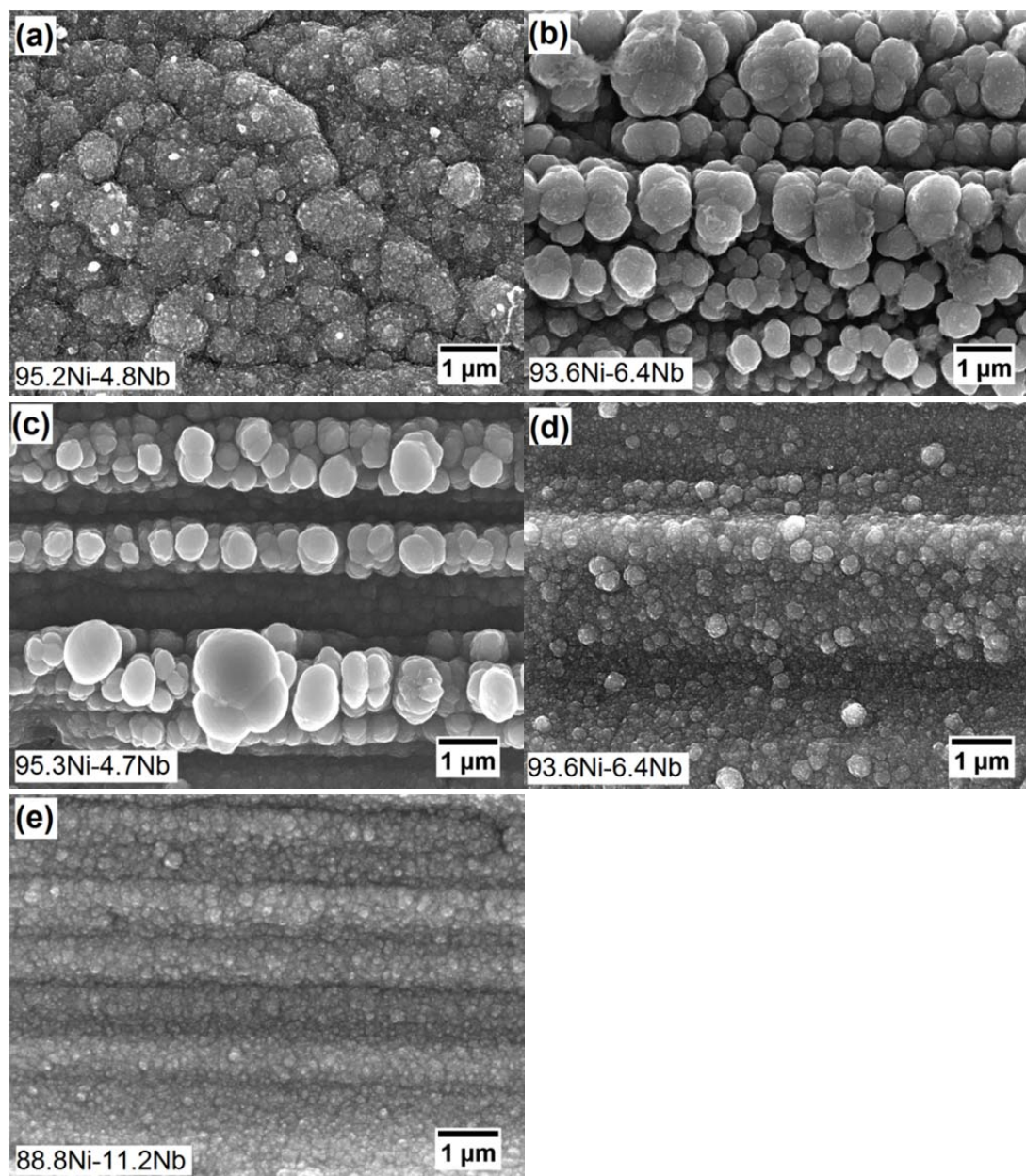


Figure 6.8 In-lens SEM images showing the typical surface morphology of Ni-Nb electrodeposited from Bath 3 at 240 r.p.m. & 100°C at a) 50, b) 100, c) 150, d) 300 and e) 400 mA/cm² with an equivalent charge passage of 360 C per cm² with the atomic composition noted (at.%)

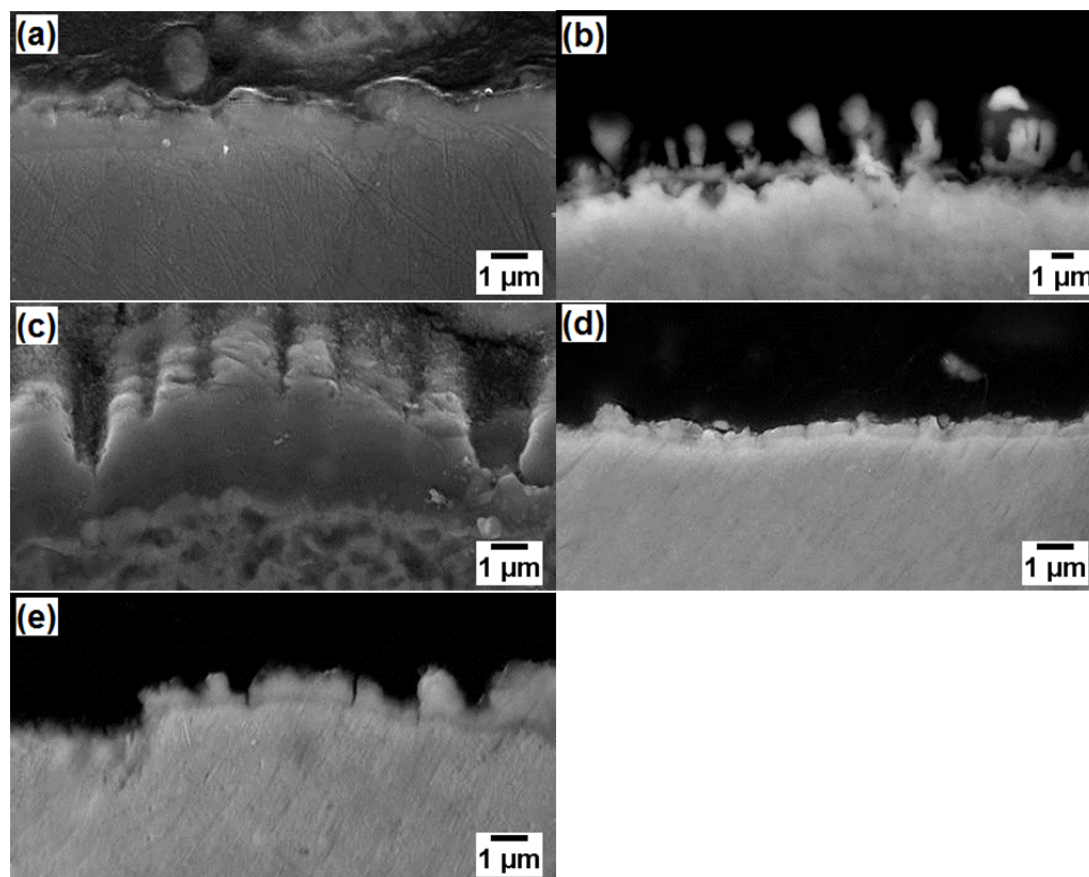


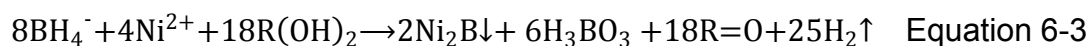
Figure 6.9 Secondary electron images illustrating the central cross-section of Ni-Nb deposited from Bath 3 at 240 r.p.m. and 100°C & at a) 50, b) 100, c) 150, d) 300 and e) 400 mA/cm² with equivalent charge passage of 360 C per cm²

6.4 Effect of Sodium Borohydride

When NaBH₄ was absent in the electrolytes, galvanostatic electrolysis generally gave slow deposition kinetics, with the resultant electrodeposits often macroscopically non-uniform. These may be ascribed to the excessive hydrogen evolution arising from high concentrations of protons in the bath. The heterogeneous formation, coalescence and detachment of hydrogen bubbles at the electrode surface not only distorts current density distribution, and also affects the local mass transport, either in an enhancing way by introducing micro- and macro-convection, or in a depressing manner to screen the electrode surface from metal deposition [6.6]. Therefore, it is reasonable to suggest that the macroscopically non-uniform development of Ni-Nb deposits was associated with the excessive hydrogen evolution.

This phenomenon has been found to become less pronounced through the electrochemical reduction process itself, where hydrogen evolution *per se* could reduce the bath acidity. Perhaps a straightforward way to suppress this competing cathodic process is through a chemical route: NaBH₄, a reducing agent, was introduced in this regard to pre-consume a portion of the hydrogen ions, without necessarily generating additional water when a base is added. However, the bath pH could not be precisely determined utilising a conventional, all-aqueous pH electrode, since the mixing of the aqueous reference-electrode-filling electrolyte and electrodeposition electrolyte through the junction induced a slow, negative drift of the pH. The present study resorted to a compromised strategy suggested from Ref. [6.7], which utilises the aqueous pH electrode, but allows a short time for the solution contact, so as to approximate the variations in the relative acidity of the electrolytes. An increase in the apparent pH from ca. -0.5 to 0.6 was recorded at 100°C upon 0.54 M NaBH₄ addition into a PG-based solution containing 0.54 M NbCl₅ (similar to Bath 2).

Also it should be noted that, NiCl₂ needs to be added after the complete reaction of NaBH₄ with the electrolyte components, otherwise Ni²⁺ ions would be chemically reduced to yield finely divided black precipitates [6.8], presumably following **Equation 6-3**:



Where R(OH)₂ represents a glycol whilst R=O denotes a carbonyl compound.

The precipitation of Ni₂B was suggested by the observation of a rapid dark coloration of the bath when NaBH₄ was added after NiCl₂. Ni₂B is an insoluble and electrochemically inactive solid, which finds no use as a metal precursor for Ni deposition.

Another advantage of NaBH₄ additions is associated with its cation. The addition of small, simple metal cations like Na⁺ into non-aqueous electrolytes has been suggested to considerably reduce the diffusion layer thickness [6.5], thereby potentially making the reduction of other metal ions like Ni²⁺ and Nb⁵⁺ easier.

Two baths have been developed to investigate the effect of NaBH₄ bath concentration on the Ni-Nb electrodeposition. Bath 2 served as a baseline where the NaBH₄ content was doubled to make Bath 5 and tripled to make Bath 6 (See **Table 6.1**). Typical surface morphology of as-deposited Ni-Nb coatings is depicted in **Fig. 6.10**, with variations in the NaBH₄ concentration and in a cathodic current density from 30 to 150 mA/cm². For both Bath 5 and Bath 6, it was generally found that an increase in the current density gives rise to a reduction in the average size of deposit surface features. This trend is consistent with the previous observations from Bath 2. At 150 mA/cm², both Baths 5 & 6 appeared to develop discrete and coral-like structures, which were absent in the case of the low metal ion concentration counterpart, Bath 2 (See **Fig 6.2(d)**). This may be ascribed to mass transfer being the rate limiting step. At large electron transfer overpotential (i.e. high cathodic current density), the consumption of Ni(II) ions in the diffusion layer for the deposition surpassed that of their replenishment. This is presumed to stimulate the discrete growth of crystal out of the diffusion layer. As the NaBH₄ bath concentration is increased, a coarsening of the coating surface features was seen. For instances, at 30 mA/cm², a triple increase in the NaBH₄ content from 0.54 M (Bath 2) to 1.62 M (Bath 6) saw an increase in the deposit feature size from submicron (**Fig. 6.10(a)**) to a few micrometres (**Fig. 6.10(e)**).

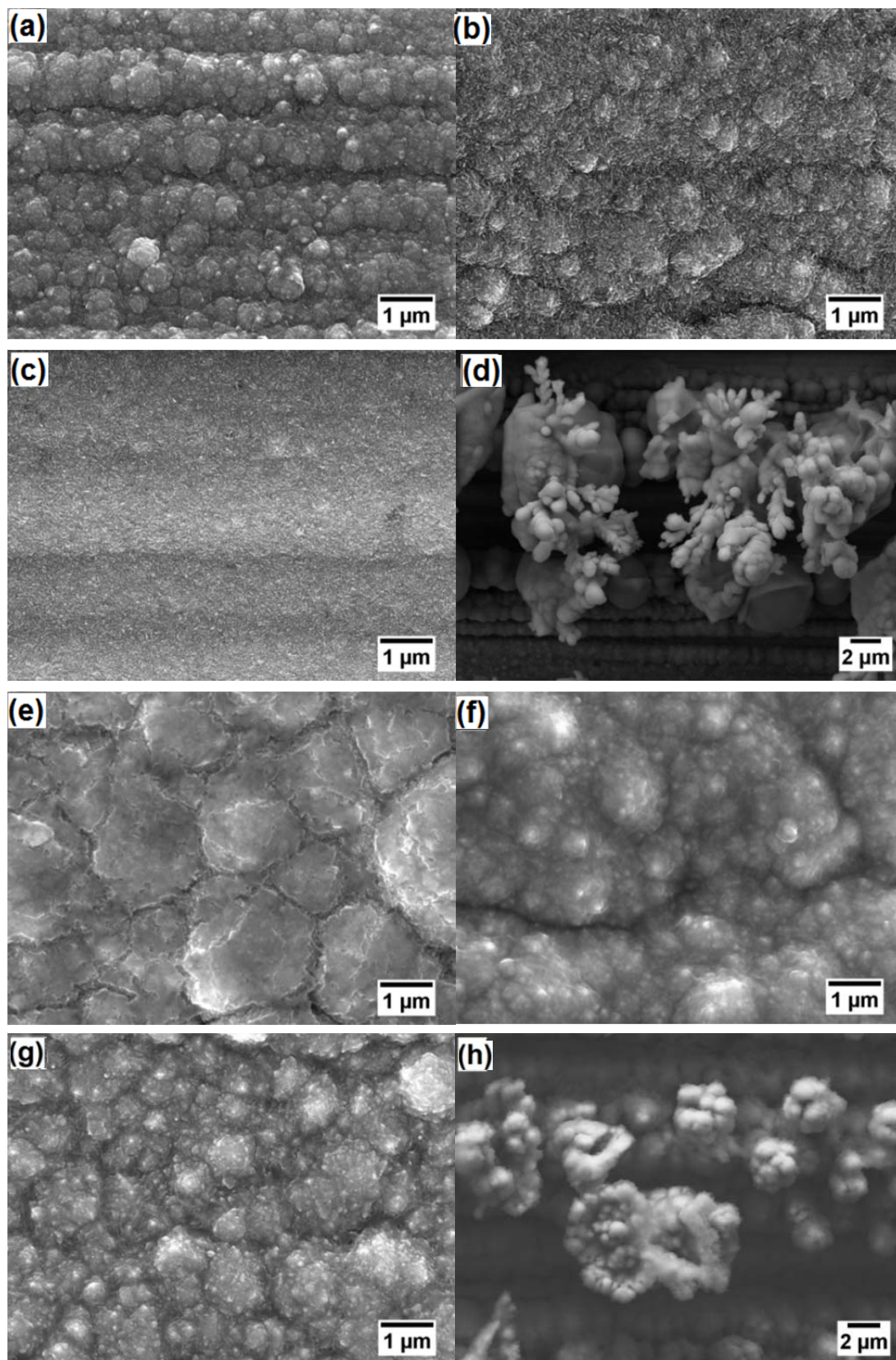


Figure 6.10 secondary electron images illustrating the representative surface morphology of Ni-Nb deposited on Cu substrate at 100°C & 240 r.p.m. from Bath 5 (a-d) and Bath 6 (e-h) at 30 (a, e), 50 (b, f), 100 (c, g) and 150 mA/cm² (d, h) with equivalent charge passage of 360 C per cm²

The codeposited Nb contents and the average central coating thicknesses are depicted in **Fig. 6.11** for Baths 2, 5 & 6. Except for the coatings obtained at 150 mA/cm² from Baths 5 and 6 which exhibited spongy surface morphology, the Ni-Nb electrodeposits were normally uniform and compact. It was generally true that the coatings with relatively small features (i.e. prepared at low NaBH₄ contents and high current densities) showed higher Nb contents (**Fig. 6.11(a)**) and low coating thickness (**Fig. 6.11(b)**). With elevating NaBH₄ bath contents from 0.54 M (Bath 2) to 1.08 M (Bath 5) and further to 1.62 M (Bath 6), the apparent pH of the electrolyte exhibited an increase from around 0.6 to 2.5 and further to 5.2 at 100 (±4)°C. This indicates the role of NaBH₄ in reducing the hydrogen ion concentration of the electrolyte. A reduction in the co-deposited Nb content at increased NaBH₄ concentration may be intuitively explained by a presumption that, the reduction in the bath acidity leads to suppressed hydrogen evolution, which increases the partial current contribution for Ni deposition, but not necessarily for Nb co-deposition. However, as NaBH₄ was further added into the solution, there was a point (ca. 2 M as compared to 0.54 M of NbCl₅) where no co-deposition of Nb would occur regardless of the cathodic current density. This implies that the protons (H⁺) may play a role in the co-deposition of Nb species, e.g. by bridging between Ni and Nb metal centres in polynuclear, multi-metallic complexes, either present in the bulk solution or electrochemically formed as electrode surface adsorbed intermediates. The formation of such metal complexes enables the possibility of homogenous co-deposition of Nb with Ni, which has been observed from the present study.

It should be noted that the central coating thickness shown in **Fig. 6.11(b)** represents the maximum achievable for each set of parameters, due to the existence of a threshold coating thickness, as has been suggested in **Section 6.2**. The average maximum thickness of the Ni-Nb electrodeposits was normally lower at increased Nb content. This suggests that the threshold

deposit thickness may be affected by the deposit composition. To be more specific, the co-deposited Nb species was largely niobium oxides, as will be primarily revealed in **Chapter 7**, may degrade the adhesion of new depositing species to the existing deposit surface. Based on this reasoning, the NaBH_4 additions effectively decrease the Nb content to be co-deposited and thereby elevating the threshold coating thickness.

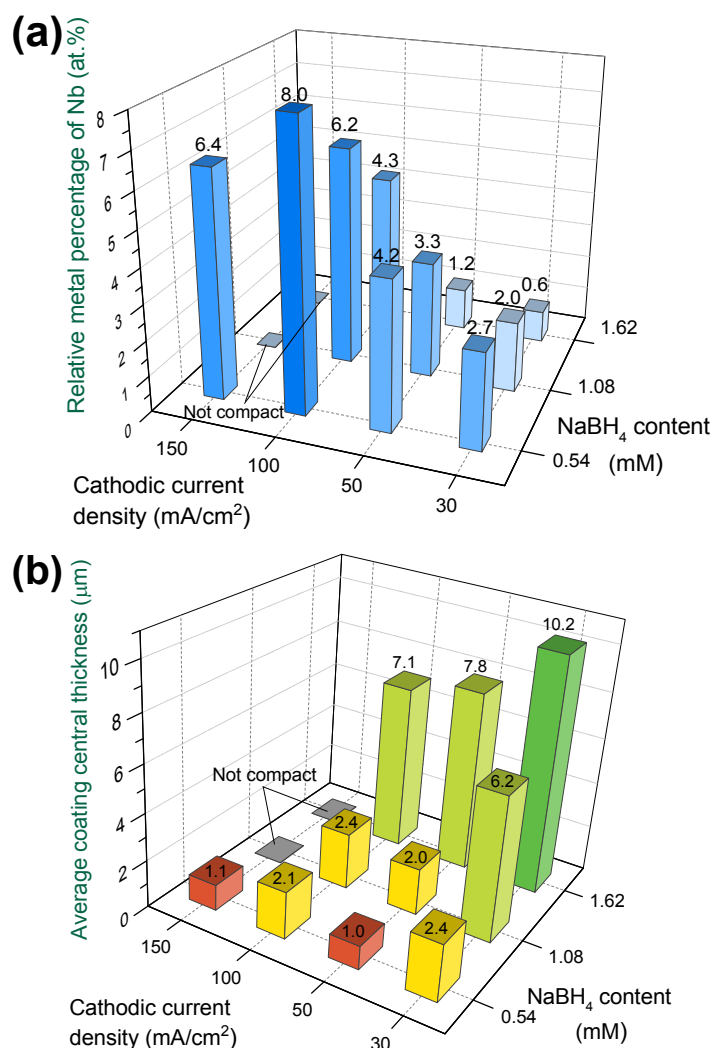


Figure 6.11 Bar charts illustrating the variations in the a) relative metal percentage of Nb (at.%) in the Ni-Nb electrodeposits and in b) average central coating thickness with cathodic current density and NaBH_4 concentrations in the electrolyte (suggested from metallographic cross sectioning)

6.5 Summary

In this chapter, a novel electrodeposition process for the preparation of Ni-Nb thin films has been developed, from a non-aqueous Type IV eutectic solvent

based on propylene glycol. The effect of electrolyte constituents, such as the type of glycol, metal ion concentration and NaBH_4 concentration, as well as the effect of cathodic current density and electrodeposition time, on the surface morphology, composition and thickness of the deposits, has been investigated. Based on the galvanostatic trials, an effective formulation and appropriate deposition parameters have been established. Macroscopic uniformity of the deposits can be achieved by introducing a reducing agent, NaBH_4 , to reduce the bath acidity and thereby suppressing the competing hydrogen evolution. Microscopic uniformity of the Ni-Nb deposits, however, requires the use of relatively low metal ion concentrations in the electrolyte, which otherwise is susceptible to produce localised and spongy deposition. A threshold deposit thickness generally exists for the Ni-Nb electrodeposits, which is presumably dependent on the co-deposited Nb content. A trade-off is also evident between large coating thickness and high Nb content for the present Ni-Nb electrodeposition system. Large deposit thickness can be pursued when high NaBH_4 content baths and small current densities are employed; whilst high Nb contents is attainable by minimising (but not eliminating) NaBH_4 concentrations in the electrolyte and maintaining relatively large current densities (yet not too high to induce spongy deposition). Based on these results, a deposition model analogous to the induced co-deposition has been proposed, wherein Nb co-deposition is allowed by the possible existence of polynuclear, Ni-Nb-based metal complexes in the electrolyte.

6.6 References

- [6.1] F. B. Speyer, *Industrial & Engineering Chemistry Product Research and Development*, **10**, 99 (1971).
- [6.2] W. Gerrard and E. D. Macklen, *J. App. Chem.*, **10** (2), 52 (1960).
- [6.3] C. Sanchez, J. Livage, M. Henry and F. Babonneau, *J. Non-crystalline Solid*, **100**, 65 (1988).
- [6.4] E. Bauer and H. Poppa, *Thin Solid Films*, **12**, 167 (1972).

[6.5] A. P. Abbott and K. J. McKenzie, *Phys. Chem. Chem. Phys.*, **8**, 4265 (2006).

[6.6] C. Gabrielli, F. Huet and R. P. Nogueira, *Electrochimica Acta*, **50** (18), 3726 (2005).

[6.7] S. P. Porras and E. Kenndler, *J. Chromatogr. A*, **1037**, 455 (2004).

[6.8] P. C. Maybury, R. W. Mitchell and M. F. Hawthorne, *J. Chem. Soc. Chem. Commun.*, **14**, 534 (1974).

Chapter 7

Characterisations of Ni-NbO_x Composite Electrodeposits

This chapter describes the results obtained from electrochemical, microstructural and spectroscopic characterisations of the Ni-NbO_x electrodeposits. A combined use of electrochemical quartz crystal microbalance (EQCM), scanning transmission electron microscopy (STEM) and X-ray photoelectron spectroscopy (XPS) was applied to understand the distribution of chemistry and composition across the coating thickness. From these results, a Ni-Nb co-deposition model is postulated.

7.1 Microstructural Characterisations of Ni-NbO_x Electrodeposits

Scanning transmission electron microscopy (STEM) bright field (BF) and high angle annular dark field (HAADF) images of a Ni-Nb coating deposited from Bath 2 at a cathodic current density of 80 mA/cm² for 60 min are depicted in **Fig. 7.1**. A banded structure with some slight variability in the layer thickness (0.1 – 0.3 μm) was evident from both BF and HAADF imaging. The layers appeared to be parallel with the interface between the deposit and substrate, suggesting the deposition proceeded layer by layer, presumably following the Frank van der Merwe growth mode [7.1] under this condition. Because the integrated intensity of the HAADF imaging exhibits a clear dependence on the mean atomic number (Z), this imaging mode is sensitive to the composition variations. The multilayer structure, therefore, indicates compositional fluctuations across the deposit thickness.

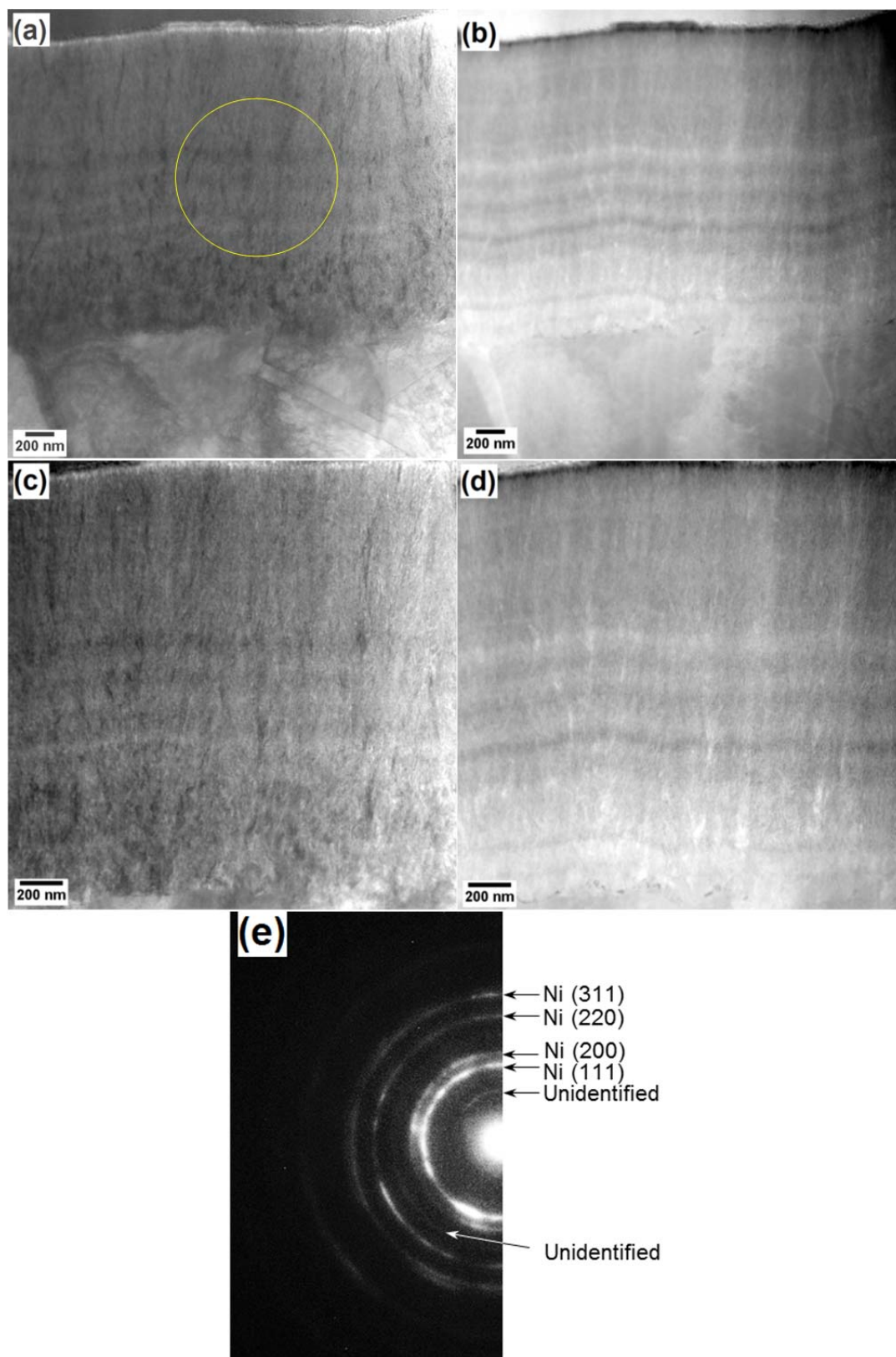


Figure 7.1 Cross sectional STEM images of a Ni-Nb coating electrodeposited from Bath 2 at 100°C & 240 r.p.m. at a current density of 80 mA/cm² for 60 min acquired at × 40,000 magnification: a) BF and b) HAADF and at × 57,000: c) BF and d) HAADF, and e) selected area diffraction pattern from the circled zone noted in a)

At higher magnifications (**Figs. 7.1 (c & d)**), it became clear that very fine microstructure had been electrodeposited. The upper region of the cross-section consisted of fibrous grain features, with a width of less than 50 nm and a length of up to several hundreds of nanometres. They were universally distributed, perpendicular, albeit not perfectly, to the deposit/substrate interface. From the bright field images (**Figs. 7.1 (a & c)**), the fibrous grains appeared to be in various intensity levels. The dark features are due to strong diffraction as the grain orientations are at, or close to the Bragg condition, whilst the lighter ones correspond to those orientations which are not strongly diffracting [7.2]. In the lower region adjacent to the interface (with a thickness of ca. 200 nm), an equiaxed grain structure was observed. This implies a change in the crystal growth mechanism during deposition, which is attributable to the grain growth competition [7.1], as is illustrated in **Fig. 7.2**. The deposition initiates with the formation of equiaxed grains with various orientations; those grain orientations of relatively low surface energy are favoured over time for grain growth, and thereby becoming elongated to form a fibrous grain morphology.

Figure 7.1 (e) depicts a typical selected area diffraction pattern (SADP) with an aperture size of approximately 1.3 μm acquired from the deposit cross-section. A ring pattern was revealed, indicative of the nanocrystalline structure. Four of the most intense rings were assigned to (111), (200), (220) and (311), which is characteristic of a face-centred cubic (FCC) structure. The corresponding lattice parameters were highly comparable to those listed in the standard powder diffraction file (PDF) for pure Ni metal, implying little lattice distortion. Therefore, even though the Nb species was universally co-deposited, it did not seem to be dissolved in the Ni lattice as a solute, which otherwise would result in lattice distortion due to the atomic size misfit between Ni (124 pm) and Nb (146 pm). Two additional rings with much lower intensity were also evident, which did not match any known niobium metal or niobium

oxide compounds (e.g. monoclinic niobium pentoxide (JCPDS 74-0298 & 37-1486) and orthorhombic niobium pentoxide (JCPDS 30-0873)). It is thus speculated to be a Ni-Nb-O-based compound, in light of the XPS chemical state analysis discussed in the following sections.

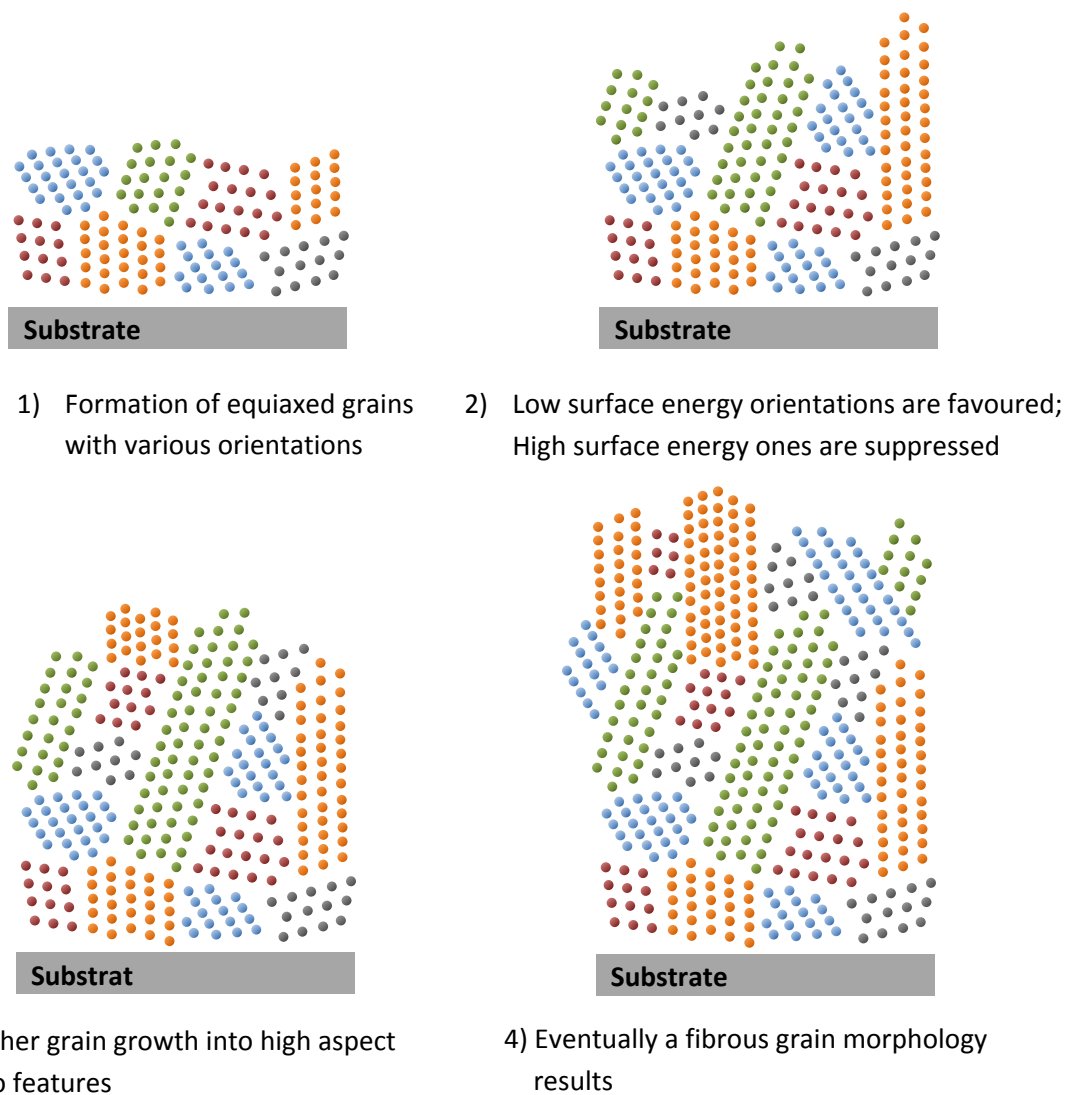


Figure 7.2 Simplified schematic diagram showing the grain structure formation mechanism of Ni-Nb electrodeposition in the present study

Figure 7.3 presents a HAADF micrograph and the associated chemistry elemental maps of the coating cross-section, along with EDX point analyses at a series of locations across the thickness. From the X-ray maps (**Figs. 7.3 (b-d)**), both Nb (L α) and O (K α) were universally distributed in the Ni (K α) phase, without any appreciable phase segregation. In the interfacial region, a

slight decrease in the atomic percentage of O and Nb was evident from both the elemental maps and EDX analyses. The aforementioned banded structure is also indicated from the X-ray maps. The brighter regions in the HAADF image (**Fig. 7.3 (a)**) suggest relatively high mean atomic number, which is intuitively *not* consistent with the X-ray mapped and EDX data that they were Ni-enriched (atomic number (z): 28), instead of being Nb-enriched with higher atomic number (41). This may be ascribed to the concurrent elevation of O content (z: 8) with Nb, which brings down the mean atomic number. An appreciable amount of O content (up to 11.5 at.%) was present in the deposit, which is due, presumably, to the co-deposition of Nb species largely as oxides. This is not surprising in light of the high affinity of Nb nuclei to O as well as the inherent availability of O-donors in the electrolyte such as glycols and water impurity. As is illustrated in **Fig. 7.3 (f)**, the atomic percentage ratio of oxygen to niobium in the upper region of the cross-section was close to 2.5, approximately fitting the stoichiometry of niobium pentoxide (Nb₂O₅). With increasing distance from the deposit surface, the atomic ratio of O to Nb saw a reduction, close to a chemical formula of Nb₂O_{3.3} in the interfacial region (e.g. Points 13 & 14). One could relate such a decreasing continuum of Nb oxidation number to the possible artificial chemical reduction induced by Ga²⁺ ion milling during the TEM sample preparation. However, assuming such a FIB-induced artefact to be uniform, a gradual change of its effect across the specimen would not occur. Therefore it is reasonable to surmise that, the Nb species was initially co-deposited as non-stoichiometric suboxides, which saw a gradual increase in their oxidation number with increasing electrodeposition time, eventually becoming approximately 5. The increase in the oxidation number of Nb compounds was also accompanied by a transition in the grain morphology from the equiaxed to fibrous. The compositional fluctuations across the deposit thickness may be explained by the alternating depletion and replenishment of Ni ions in the diffusion layer. This will be further discussed from an electrochemistry viewpoint later.

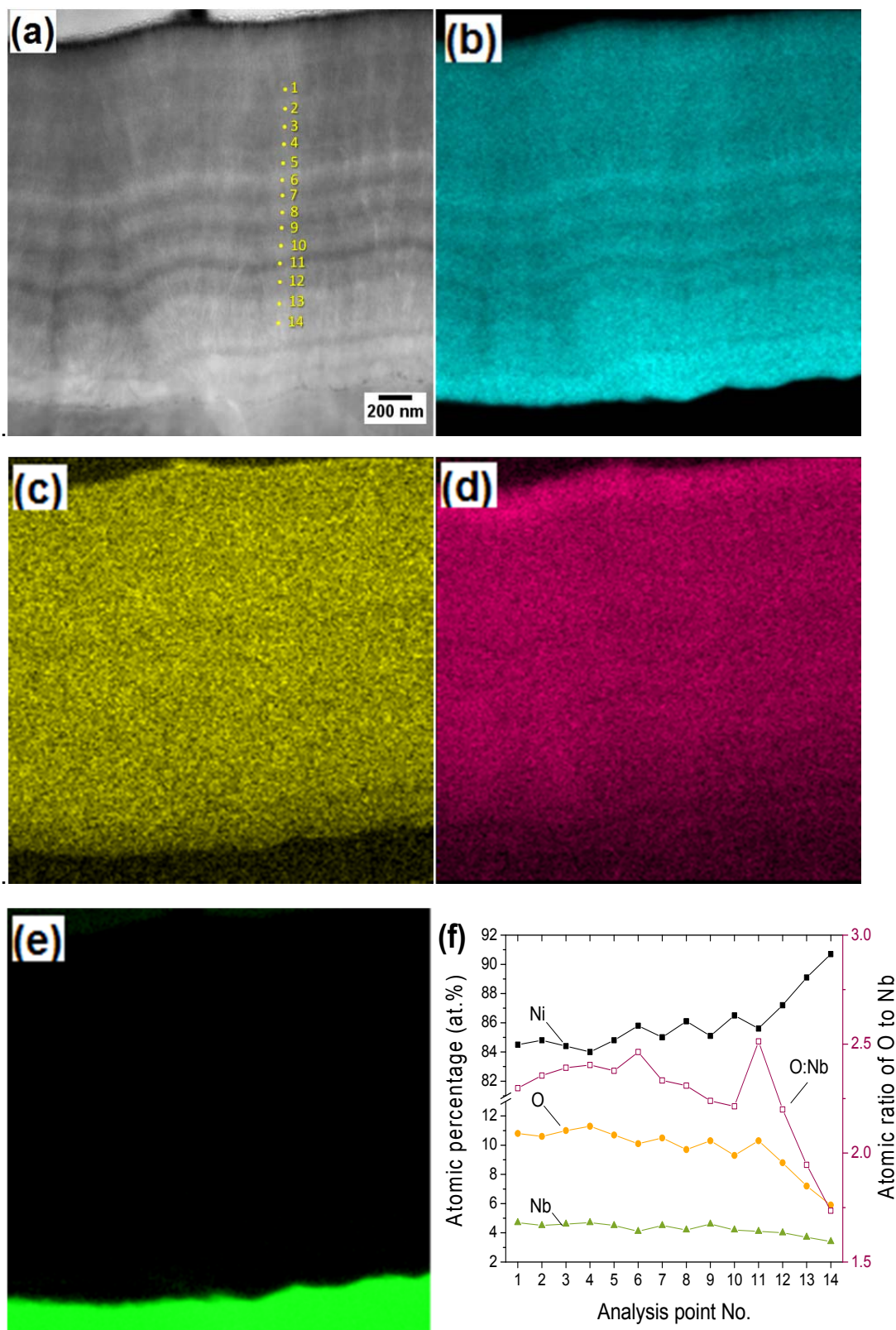


Figure 7.3 STEM cross-sectional image a) of a Ni-Nb electrodeposited from Bath 2 at 100°C & 240 r.p.m. at 80 mA/cm² for 60 min with the elemental maps of b) Ni K α , c) Nb L α , d) O K α and e) Cu K α and f) a plot presenting the EDX composition analysis results indicated in a)

7.2 Spectroscopic Characterisations of Ni-NbO_x Electrodeposits

X-ray photoelectron spectroscopy (XPS) analysis, combined with *in-situ* argon (Ar) ion sputtering, was employed to understand the in-depth composition and chemical state of Nb species in a Ni-NbO_x electrodeposit specimen. The chemical state of Nb species can be determined from its binding energy and chemical shifts in the XPS electron spectra. Both Ar monomer ion and Ar cluster ion source have been applied to perform the sputtering.

7.2.1 Depth Profiling Using Argon Monomer Ion Beam

The investigations started off by using the conventional monatomic Ar ion source. A brief etching step using an ion energy of 200 eV for 30 s was performed to eliminate the adventitious carbon (C 1s) on the specimen surface. After that, depth profiling using an ion energy of 500 eV was undertaken, at a rate of 0.27 nm/s estimated with reference to Ta₂O₅. Electron spectra were acquired after each sputtering level and quantified to give an atomic composition profile. **Figure 7.4** presents the variations of the deposit composition with sputtering time. The Nb content after the brief etch was approximately 15.0 at.%, which fell to 10.0 at.% after 60 min of sputtering. This was followed by a progressive drop from 10.0 to 2.3 at.% until the analysis terminated at 4700 s when the Cu substrate had been exposed (indicated by an evident rise of Cu content). O 1s appeared to exhibit a similar compositional depth profile to that of Nb, albeit at higher atomic percentages. The O content was initially at 45.5 at.%, which dropped significantly to 19.0 at.% after 60 s of sputtering, followed by a gradual decrease to 7.5 at.% until the deposit-substrate interface was exposed. The abrupt increase in the contents of Nb and O in the superficial region (estimated as 16.2 nm thick) indicates an elevation of the co-deposited Nb oxide content, which is thought to result in loss of deposit adherence and hence prevents the deposit thickness from further increasing. By contrast, the Ni content increased from 39.5 to 75.5 at.% after the initial 120 s sputtering, after which it elevated to a plateau at 82.0 at.%

and maintained this throughout the rest of the deposit thickness. The XPS results essentially agree with those obtained from STEM/EDX analysis, although with the absence of compositional fluctuations across the deposit thickness. This could be ascribed, first, to the large sampling area of XPS (ca. 300 μm), which, together with substrate roughness, averages out the small out-of-plane compositional changes; and secondly, to any possible ion beam sputtering induced artefacts such as atomic mixing and non-layer-by-layer material removal.

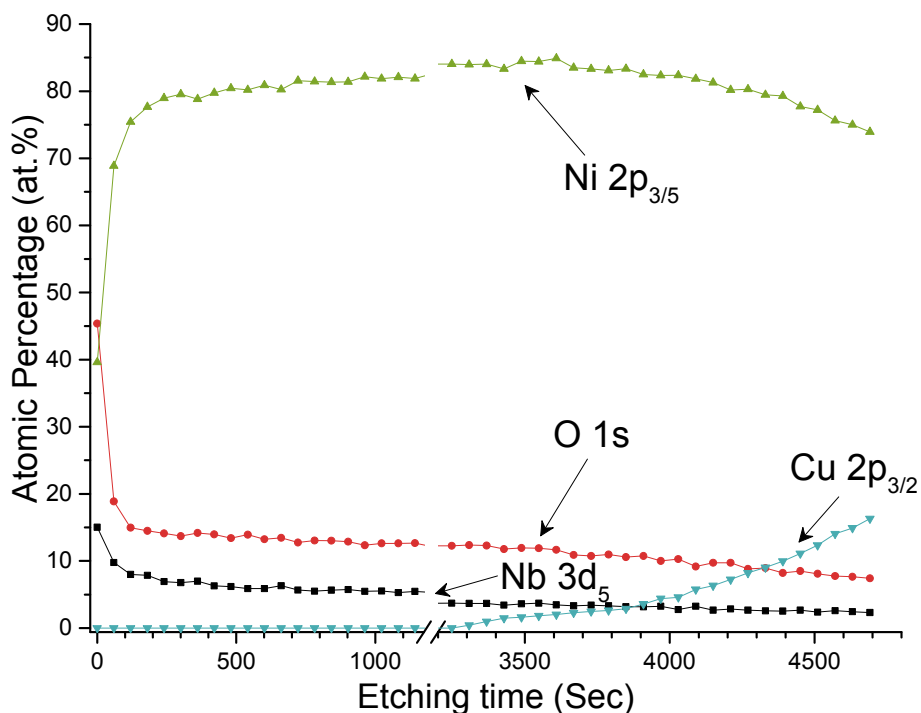


Figure 7.4 XPS Compositional depth profiling of a Ni-Nb electrodeposited from Bath 2 at 100°C & 240 r.p.m. and at a cathodic current density of 100 mA/cm² for 45 min

After the initial minimal sputter, a metallic Ni doublet peak was observed, which was maintained throughout the entire deposit thickness. **Figure 7.5** presents the 2p_{3/2} component of Ni, with an obvious satellite peak with a binding energy of approximately 6.2 eV above the main line at 852.8 eV. The presence of the satellite peak at 859.0 eV is due to energy loss associated with the transition from high spin Ni 3d to low spin Ni 4s in surface atoms [7.3]. This should be

clearly differentiated from any Ni oxide peak.

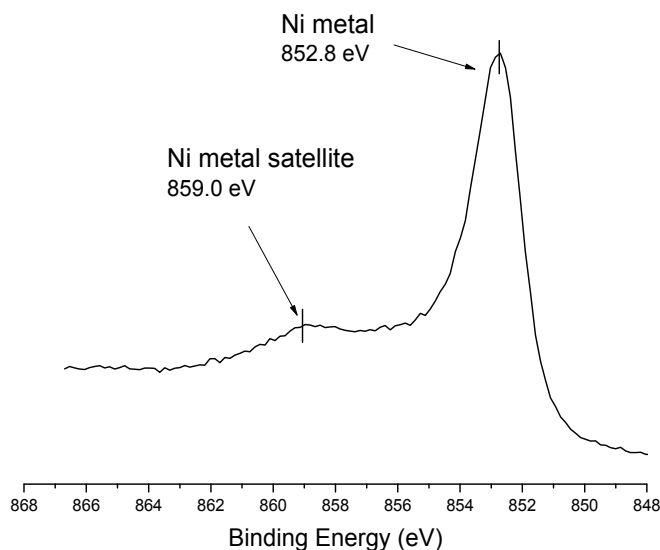


Figure 7.5 XPS Ni 2p_{3/2} narrow spectra of a Ni-Nb coating electrodeposited from Bath 2 at 100°C & 240 r.p.m. at 100 mA/cm² for 45 min after the brief sputter

In the case of Nb, the deconvoluted XPS spectra of Nb 3d acquired from the coating surface, in the bulk coating and close to the deposit/substrate interface, are presented in **Fig. 7.6**, whilst the Nb 3d spectra from both a pure Nb metal and a pure Nb₂O₅ specimen are also given for comparison (**Fig. 7.6 (d)**). On the deposit surface, the Nb₂O₅ doublet separated by 2.8 eV with the 3d_{5/2} component at 206.7 eV was observed, which is the predominant Nb species. The binding energy of the Nb₂O₅ doublet, i.e. 3d_{5/2}: 206.7 eV, is unusual, since most published works [7.4-7.6], together with the current study which examined a pure niobium pentoxide sample (**Fig. 7.6 (d)**), reported a 0.7 eV higher value at 207.4 eV. Such an appreciable reduction in binding energy suggests a change in the chemical environment of Nb atoms, more specifically, a reduction in the ligand electronegativity. It has been established that by cationic substitution of Nb₂O₅ with Li to form Li_xNb₂O₅, one could expect a seemingly analogous chemical shift of the Nb 3d towards lower binding energy of near 0.3 eV through the build-up of a Nb-Li metal bonding [7.4]. It is therefore speculated that the Nb species was co-deposited with Ni from

Ni-Nb-based, polynuclear metal glycoxide complexes. The resulting Nb compounds exhibited an oxidation number intermediate between 4 and 5.

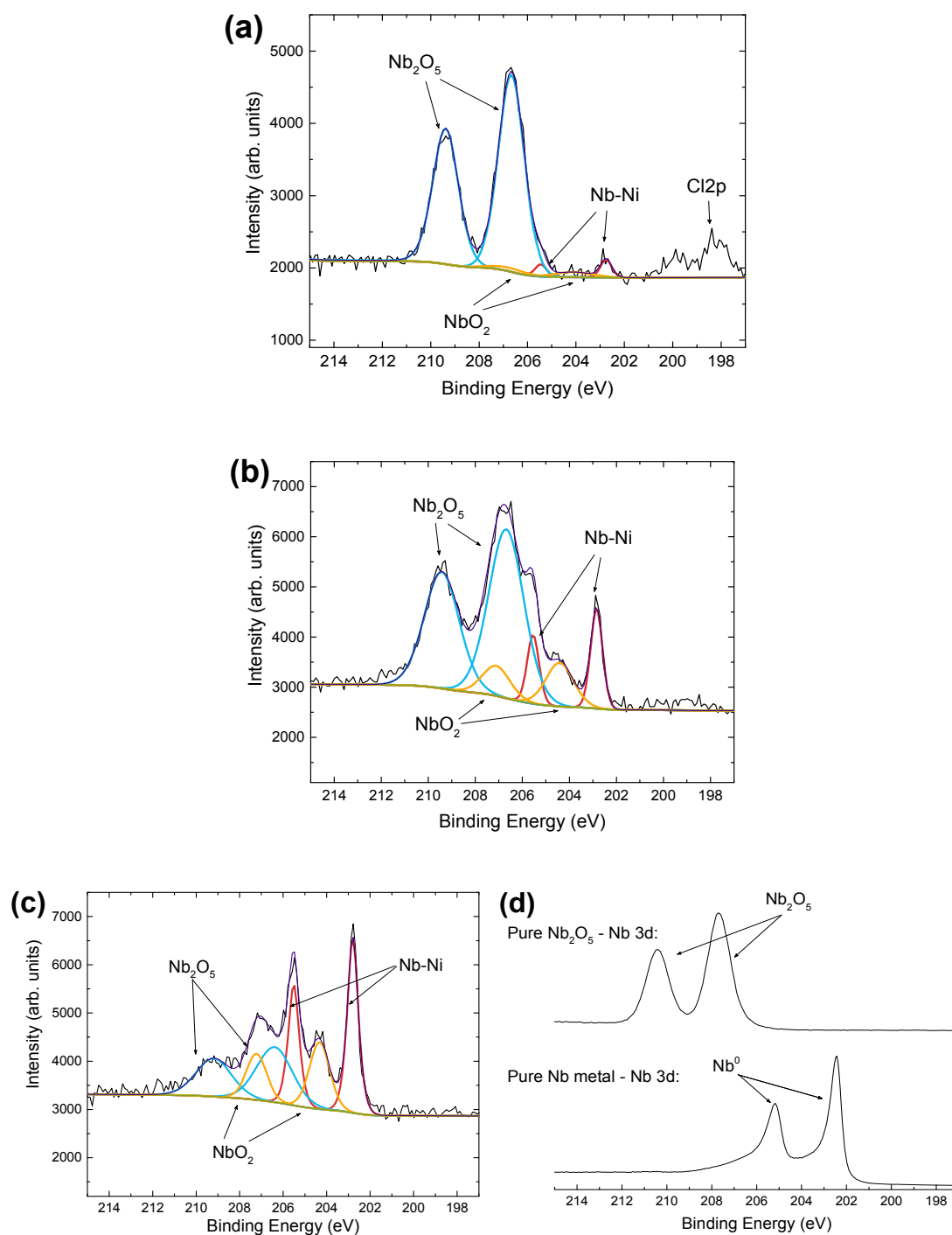


Figure 7.6 Deconvoluted XPS Nb 3d narrow spectra of a Ni-Nb coating electrodeposited from Bath 2 at 100°C & 240 r.p.m. at 100 mA/cm² as a function of Ar⁺ ion beam (500 eV) sputtering time: a) 0 s, b) 240 s and c) 3800 s and d) of both a pure Nb₂O₅ and a pure Nb metal sample (after sputtering off the surface native oxides)

Also from **Fig. 7.6 (a)**, a low intensity peak was observed at 202.8 eV, which could be assigned as the 3d_{5/2} component of a lower valance Nb compound, with its other component (3d_{3/2}) forming a shoulder of the 3d_{5/2} component of Nb₂O₅ doublet at 205.4 eV. Another weak and ill-shaped doublet with the main line at 198.4 eV was assigned to Cl 2p, attributable to the contamination of electrolyte residue on the coating surface. The adventitious Cl disappeared after the first sputter level (30 s), indicating the absence of Cl content in the bulk deposit. After 240 s of sputtering (**Fig. 7.6 (b)**), the spectra saw an apparent rise of the aforementioned low valance Nb doublet at 202.8 eV. This doublet exhibits a binding energy 0.4 eV higher than that of Nb⁰ (3d_{5/2} at 202.4 eV) but still 0.3-0.7 eV lower than that is observed for NbO (3d_{5/2} at 203.1-203.5 eV [7.7]). Moreover, this binding energy is close to that of the Nb metal observed from Ni-Nb alloys [7.8], combined with a narrow and sharp geometry characteristic of a metal peak, points to the possible presence of Nb metal bonded with Ni in the deposit. Even though the SADP data (**Fig. 7.1 (e)**) has provided the evidence that Nb was not substitutively dissolved in the Ni matrix, the co-deposition of Nb may still occur in the formation of Ni-Nb-based complexes (intermediates) during electrolysis. In this regard, there might be at least two chemical states of Ni, with the majority deposited in the elemental state and the remaining bonded to Nb. However, the monatomic ion sputtering source failed to detect any chemical shift of Ni presumably due to the well-known artificial chemical reduction of Ni compounds by the ion monomer sputtering [7.9].

Also from **Fig. 7.6 (b)**, an intermediate doublet also became evident, which was positioned at 204.5 eV (3d_{5/2}) and with a spin orbital splitting of 2.8 eV. This doublet was clearly assigned to NbO₂ (IV). After 3800 s of sputtering where the deposit/substrate interface had been exposed (**Fig. 7.6 (c)**), the Nb 3d spectra saw a further rise of the lower valent Nb doublets (i.e. NbO₂ and Nb metal bonded with Ni). These results suggest a continuum of niobium oxides

towards lower mean oxidation numbers with increasing sputtering time, which provides a definite indication that niobium was primarily co-deposited with nickel metal as oxides.

Figure 7.7 represents the relative atomic percentage of three chemical states derived from the deconvoluted Nb 3d spectra. It was found that, with increasing etching time, there was a progressive decrease in the atomic proportion of Nb₂O₅, which occurred along with the rise of the two lower valance chemical states. The percentages of the three chemical states became nearly comparable after an etching time of 2500 s, which corresponds to an estimated depth of 400 nm. Simply attributing such a progressive evolution of niobium oxides to re-oxidation after electrodeposition would hardly hold, because a depth of around 400 nm far surpasses the native oxide thickness for Nb metal upon ambient storage, which was suggested to be less than 10 nm from the pure Nb metal control sample assessed in this study. A more likely explanation is the artificial chemical reduction of Nb compounds by continual Ar⁺ ion monomer beam etching.

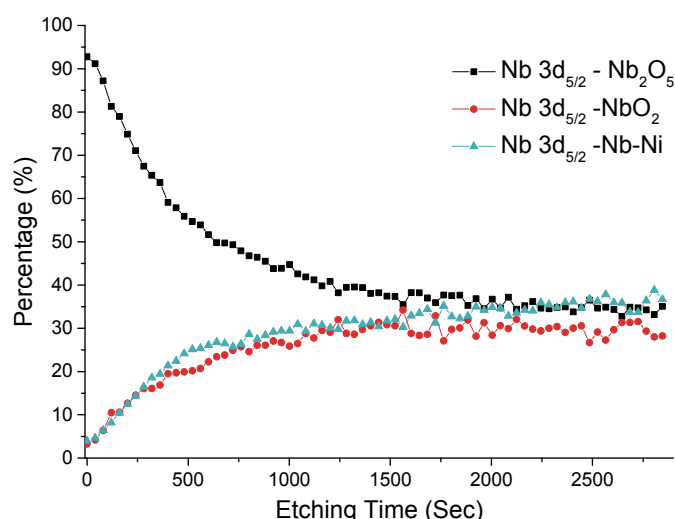


Figure 7.7 Relative atomic percentage depth profiling of three niobium chemical states as a function of Ar⁺ ion monomer beam sputtering time based on deconvoluted XPS spectra of a Ni-Nb deposited sample from Bath 2 at 100°C & 240 r.p.m. at 100 mA/cm² for 45 min

To ascertain the possible ion monomer sputtering artefact, a pure Nb₂O₅ powder specimen has been studied. **Figure 7.8** depicts the Nb 3d narrow spectra obtained from the Nb₂O₅ control sample as a function of etching time at two ion energies of 200 and 500 eV, respectively. The artificial chemical reduction initiated fairly quickly, merely after 30 s of etching at the two ion energies. This consequently leads to a reconsideration of the aforementioned chemical state depth profiling data. However, the EDX analysis from STEM still suggests the possible presence of niobium suboxides in the region close to the interface. Therefore, to preclude the ion monomer induced effect, an Ar⁺ cluster ion sputter source has also been employed.

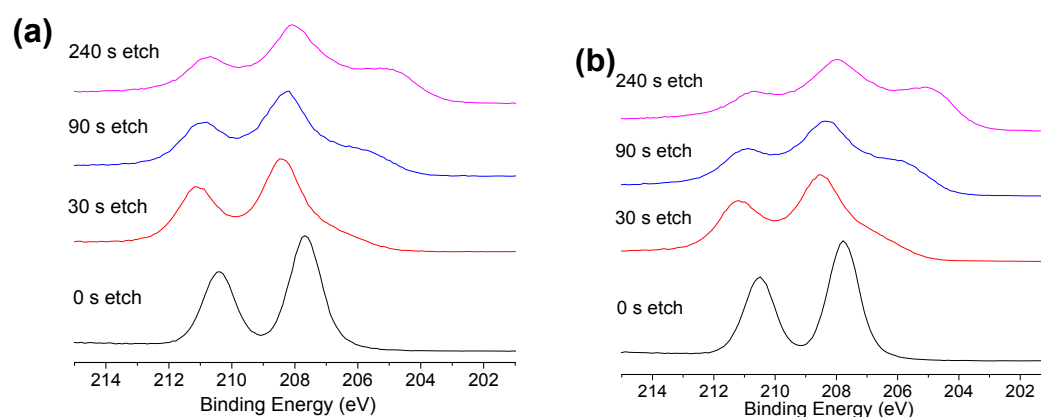


Figure 7.8 XPS Nb 3d narrow spectra of a pure Nb₂O₅ powder specimen as a function of Ar⁺ ion monomer beam etching time using an ion energy of either a) 200 eV or b) 500 eV

7.2.2 Depth Profiling Using Argon Gas Cluster Ion Beam

Argon (Ar) gas cluster ion beam (GCIB) sources produce ionised Ar clusters, with a size distribution between ca. 500 to 5000 atoms. This is in contrast to its monatomic ion source counterpart as the former exhibits much reduced kinetics energy per unit and thereby greatly reducing the damage to the sampling surface [7.10]. This advantage has been exploited to ascertain the in-depth chemical states of Ni-NbO_x electrodeposits, whilst preserving the chemistry from sputtering artefacts. The depth profiling and XPS analysis

parameters for the use of the two sputtering sources are collated in **Table 7.1**.

Parameters	Monomer Ion Beam	GCIB
Ion Energy	500 eV	4,000 eV (small cluster mode ⁶)
Estimated sputtering rate ⁷	ca. 0.26 nm/s	ca. 0.016 nm/s
Raster size	1.5 × 2 mm	1 × 2 mm
X-ray spot size	300 μm	300 μm

Table 7.1 A summary of XPS depth profiling and XPS analysis parameters for Ar monomer ion beam and GCIB sources

Figure 7.9 depicts the deconvoluted Ni 2p_{3/2} narrow spectra acquired after various GCIB sputtering time. A Shirley background was employed across the 2p_{3/2} portion of the spectra. Based on the published approach [7.11], the higher binding energy end of the background was adjusted with a slight offset for the purpose of improving the peak fitting.

⁶ Small cluster mode: Application of a semi-log size distribution centred around 1000 atoms per cluster

⁷ Estimated sputtering rate: with reference to Ta₂O₅

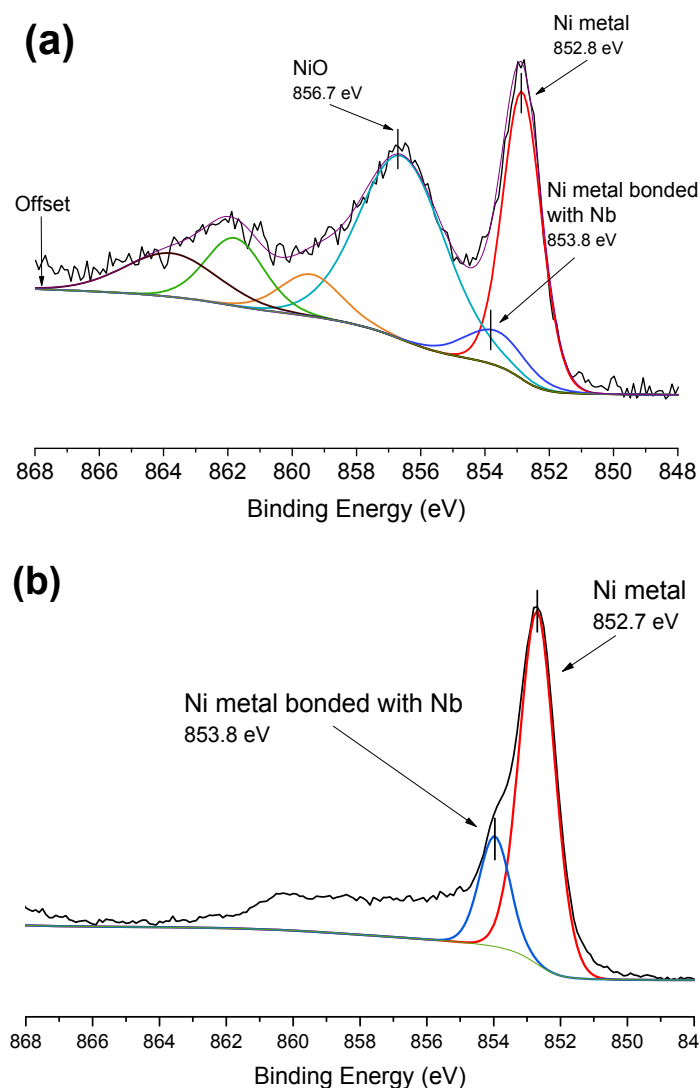


Figure 7.9 XPS Ni 2p_{3/2} narrow spectra of a Ni-Nb coating electrodeposited from Bath 2 at 100°C & 240 r.p.m. at 100 mA/cm² (and ambient stored for 30 days) as a function of Ar⁺ GCIB beam sputtering time: a) 60 s and b) 900 s

After 60 s of cluster ion sputtering (**Fig. 7.9(a)**), the Ni 2p spectra still saw two major chemical states, i.e. Ni metal with the main line centred around 852.8 eV and the other peak positioned at 856.7 eV attributable to NiO. The presence of NiO is due to oxidation of the electrodeposited sample during ambient ageing (in this case, approximately 30 days). This signifies the low susceptibility of NiO to artificial chemical reduction when subject to cluster ion beam sputtering. A few satellite peaks were also assigned at higher binding energies. Here an additional weak peak centred around 853.8 eV was allocated. The NiO peak intensity decreased with increasing sputtering time, which diminished after

near 600 s. Beyond 600 s, the Ni 2p spectra retained a distinct Ni metal pattern although a low intensity peak at 853.8 eV was evident forming a shoulder at the higher binding energy side of the Ni metal peak (See **Fig. 7.9 (b)**). This shoulder peak may be assigned to Ni metal bonded with Nb as mentioned above.

In the case of Nb, **Figure 7.10** illustrates the deconvoluted Nb 3d narrow spectra obtained after various GCIB sputtering time up to 4920 s (where the sputtering was terminated). It was found that the Nb₂O₅ doublet at 206.7 eV maintained as the predominant Nb species, with a low intensity doublet at 202.8 eV (3d_{5/2}) which may be attributed to the Nb metal. The Nb 3d spectra almost remained almost the same with increasing sputtering time up to 4920 s, indicative of few ion beam sputtering artefacts. The positions of all the doublet components were consistent with the data from monomer ion beam sputtering.

A pure Nb₂O₅ powder specimen has been sputtered using the GCIB source for comparison. **Figure 7.11** presents the XPS Nb 3d spectra acquired after various sputtering time up to 900 s. It was evident that no artificial chemical reduction of Nb oxides occurred when subject to GCIB sputtering at an ion energy of 4000 eV up to 900 s. Therefore, the GCIB source has proved reliable for the depth profiling of Nb pentoxide based specimens.

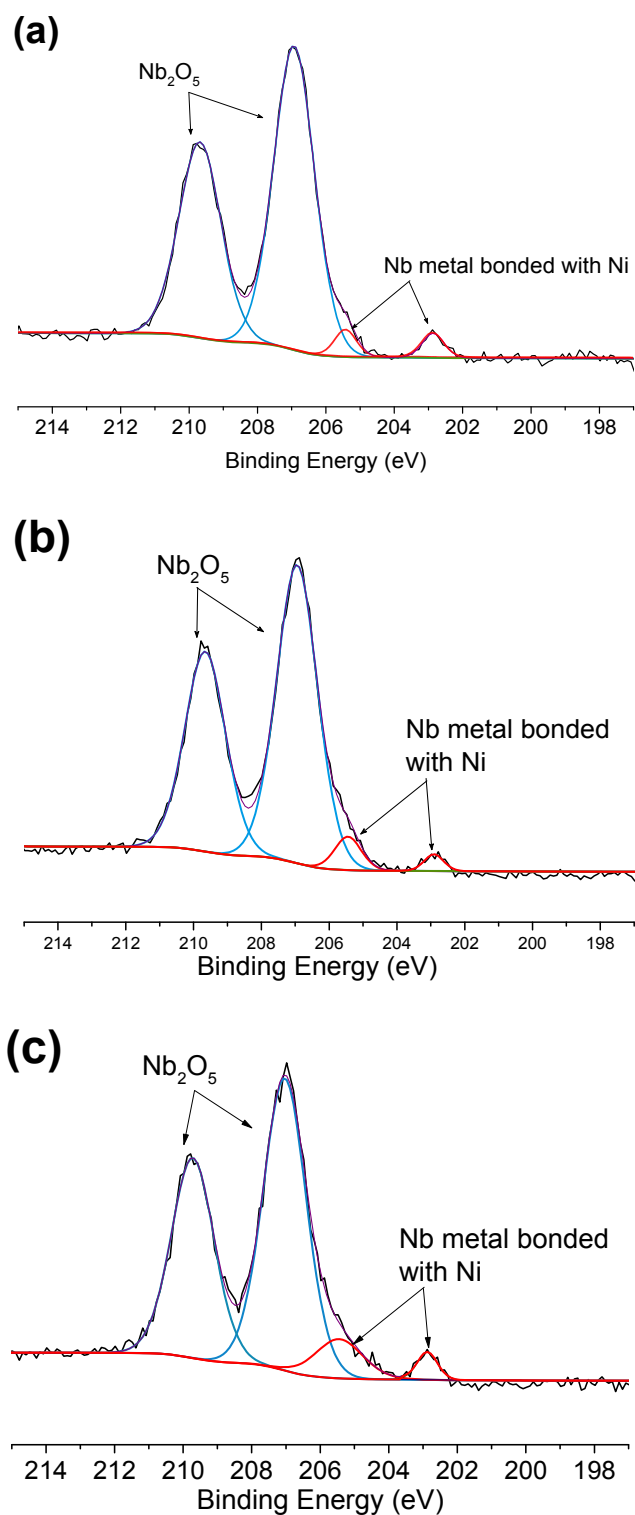


Figure 7.10 XPS Nb 3d narrow spectra of a Ni-Nb coating electrodeposited from Bath 2 at 100°C & 240 r.p.m. at 100 mA/cm² (and ambient stored for 30 days) as a function of Ar⁺ GCIB beam sputtering time: a) 60 s, b) 900 s and c) 4920 s

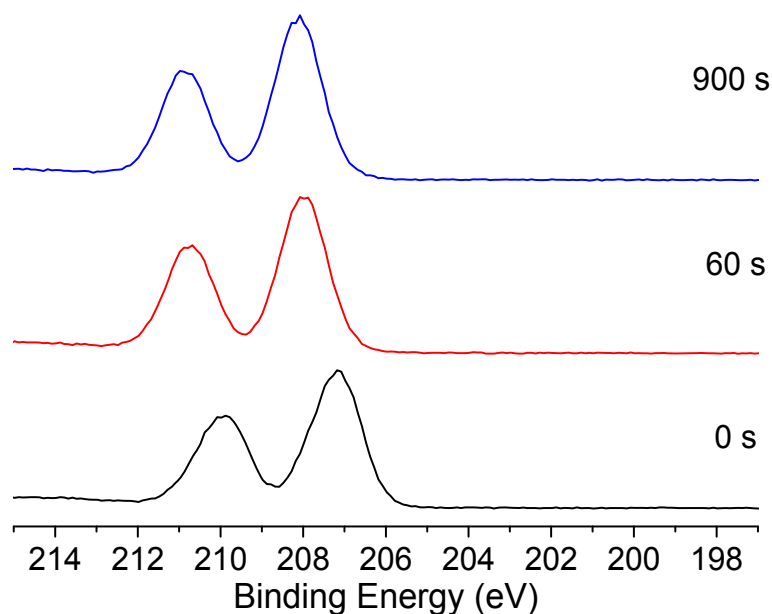


Figure 7.11 XPS Nb 3d narrow spectra of a pure Nb₂O₅ control sample as a function of Ar⁺ GCIB beam sputtering time

To summarise, even though the GCIB data did not point to a progressive evolution of the Nb species towards lower oxidation number, it still can be deduced that:

- 1) Nb was largely deposited as Nb₂O₅, which is likely to be co-deposited with Ni metal, in light of a chemical shift of the Nb₂O₅ doublet;
- 2) Ni was largely deposited as metal, but a small percentage of it was co-deposited with Nb species forming Ni-Nb metal bond. This is suggested from the observation of two low binding energy chemical states of Ni in its 2p spectra;
- 3) The electrochemical reduction routes of Nb were complex. A small portion of Nb species had been reduced to a lower valence (presumably Nb metal), whilst the remaining co-deposited as pentoxides.

7.3 Microbalance Study of Ni-Nb Electrodeposition

The galvanostatic deposition trials were conducted in conjunction with an electrochemical quartz crystal microbalance, so as to *in-situ* monitor the deposition kinetics as well as to understand the relationship between reduction potentials and deposition rates. A Pt coated quartz crystal was utilised as the cathode and immersed in Bath 2. The mass change of the cathode was derived from the recorded oscillation frequency change and is plotted against electrodeposition time in **Fig. 7.12**. As electrolysis initiated, the reduction potential rapidly elevated to -5.2 V (vs. Nb wire) and fluctuated throughout the deposition until the microbalance became overloaded at 1650 s. The potential fluctuations largely ranged between -4.6 V and -6.5V. It seemed to follow a certain pattern: the potential progressively became more negative until a point when it suddenly dropped back to the initial value. The period for potential fluctuations also varied, ranging from tens of seconds to ca. 200 seconds. The potential fluctuations can be attributed to the alternating depletion and replenishment of Ni ions (the predominant depositing species) in the diffusion layer. This is also consistent with the compositional fluctuations from STEM EDX analysis results. In terms of electrode mass, an increasing mass trend was evident, albeit with slight fluctuations presumably due to the interaction with hydrogen bubbles. The increase in the mass appeared to become more rapid, which is thought to be related to an elevation in the partial current density for Nb reduction during deposition. Two subsections of the microbalance plot are presented in **Fig. 7.13**. A recovery of the deposition rate was observed where a sudden change in the reduction potentials occurred. This implies the regular replenishment of Ni ions into the diffusion layer, which brings down the concentration overpotential. Unfortunately the deposition data beyond 1650 s cannot be acquired due to the overloading of the microbalance. Nevertheless a stoppage of the deposition is expected when a certain thickness is achieved. The existence of the limiting coating thickness is due to loss of the deposit adherence described in the previous chapter.

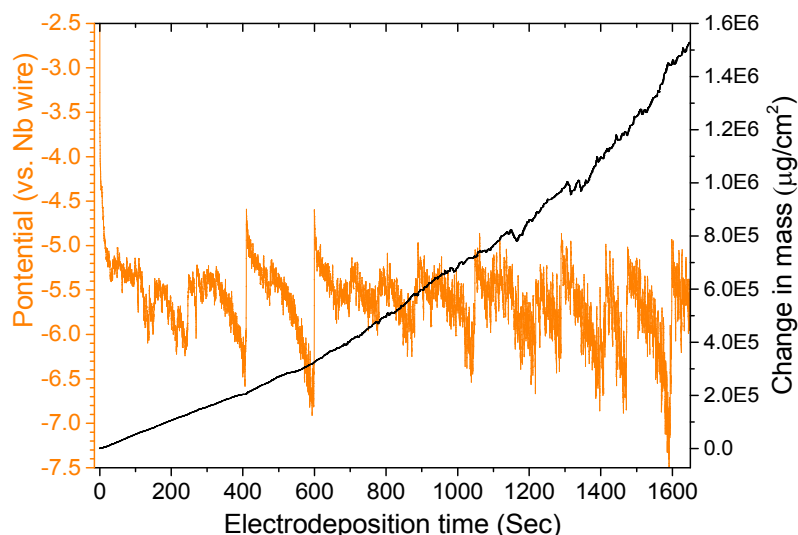


Figure 7.12 Galvanostatic and EQCM plots showing the variations in the deposition potential (vs. Nb wire) and mass on the cathode with time for Ni-Nb electrodeposition from Bath 2 at 100°C & 240 r.p.m. at 100 mA/cm²

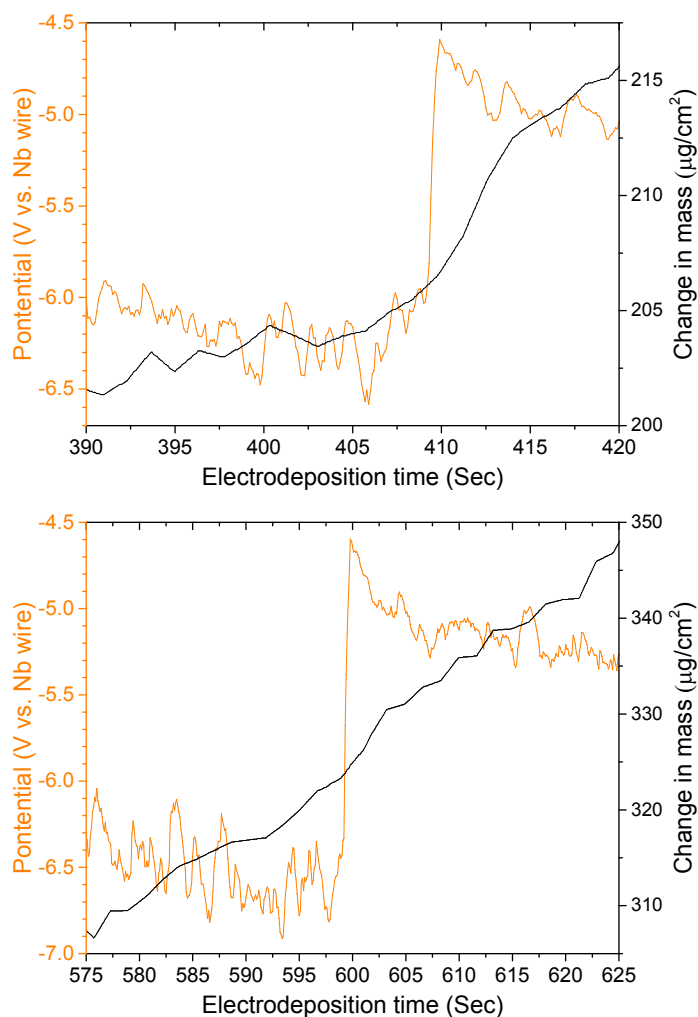


Figure 7.13 Two sections of EQCM plots showing the variations in the deposition potential (vs. Nb wire) and mass on the cathode with time for Ni-Nb electrodeposition from Bath 2 at 100°C & 240 r.p.m. at 100 mA/cm²

7.4 Mechanism for Ni-Nb Electrodeposition

In light of the microstructural, spectroscopic and electrochemical analysis data shown previously, a mechanism for Ni-Nb electrodeposition in the present study can be put forward.

At least three parallel electrochemical reduction routes existed for the current system:

1) Deposition of Ni metal through reduction of Ni (II) ionic species (e.g. Ni glycoxides) as is illustrated in **Fig. 7.14**;

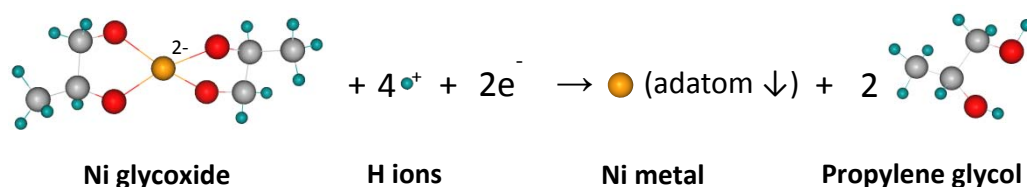


Figure 7.14 A schematic diagram showing the Ni deposition mechanism in the present study

2) Electrolytic formation and subsequent deposition of ultrafine Ni-Nb-O clusters from heteronuclear ionic complexes exemplified in **Fig. 7.15**. Glycoxide ligands are strong Lewis bases, which tend to bridge metals. A Ni-Nb glycoxide solution is likely to permit formation of heteronuclear, Ni-Nb-based ionic complexes chelated by the glycoxide ligand. This, in turn, raises the availability of electrolytically formed Nb-Ni-O species at the electrode, the adsorption of which would not necessitate long range migration from the bulk electrolyte as encountered in conventional composite electrodeposition paradigm. This consequently leads to an unusually uniform and repeatable dispersion of the NbO_x nanoclusters within the Ni matrix. The identification of two chemical states of Ni, as well as the appreciable chemical shift of Nb₂O₅, corroborates with such a hypothesis.

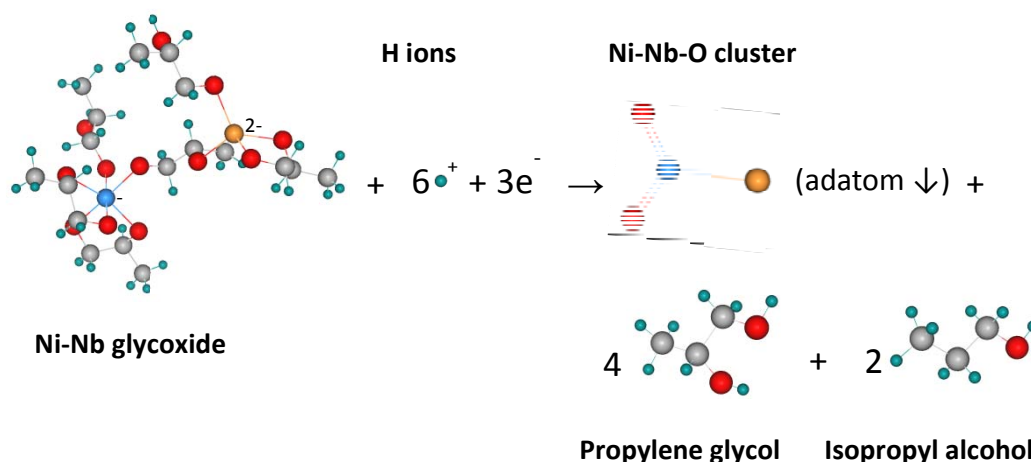


Figure 7.15 A schematic diagram showing one possible co-deposition mechanism for NbO_x in the present study

3) Hydrogen evolution from protons (H⁺) forming hydrogen bubbles at the cathode.

As the electrodeposition proceeds (e.g. from Position A in **Fig. 7.16**), the diffusion layer became gradually depleted in the Ni (II) ions (i.e. the predominant depositing species). This, in turn, steadily increases the concentration overpotential (via Position B in **Fig. 7.16**). When the cathodic overpotential arrives at a critical value (Position C), the Ni reduction was interrupted, whilst the partial current density for the reductions of Nb ionic species and protons (H⁺) become elevated. This leads to higher NbO_x content to be co-deposited and increased hydrogen evolution. The various diffusion mechanisms involving bath agitation (macro agitation), hydrogen evolution (micro agitation) and concentration gradient would then replenish the Ni ions back into the diffusion layer and also reduce the local pH [7.12]. This, in turn, brings down the overpotential, probably back to its initial value (Position C), causing a recovery of the Ni deposition rate and hence more Ni content deposited. Nevertheless, as all the three aforementioned reduction routes consume hydrogen ions, the electrodeposition is inevitably accompanied by a

reduction in bath acidity. This progressively increases the minimum pH in the diffusion layer for each ion replenishment cycle and causes an ever-decreasing Ni content in the coating with increasing electroplating time. To summarise, it is due to the alternating depletion and replenishment of Ni ions in the diffusion layer that gives rise to compositional fluctuations across the deposit thickness.

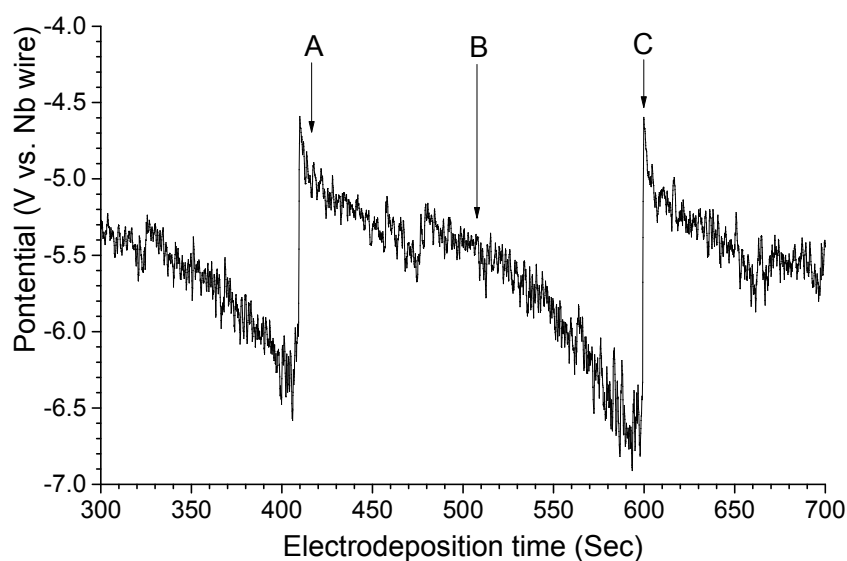


Figure 7.16 A subsection of galvanostatic plot showing the variations in the deposition potential (vs. Nb wire) with time for Ni-Nb electrodeposition from Bath 2 at 100°C & 240 r.p.m. at 100 mA/cm²

7.5 Summary

In this chapter, STEM characterisations have disclosed the ultra-fine microstructural details of the nanocrystalline Ni-NbO_x electrodeposits, where an unusually uniform yet repeatable dispersion of NbO_x clusters was observed within the Ni matrix. A reduction in the Ni content was recognised with increasing distance to the substrate-deposit interface, together with slight compositional fluctuations. Electron diffraction data suggested the absence of Nb species within the Ni lattices, indicating that no bulk alloy was formed. XPS data reported an unusual chemical shift of Nb species towards lower binding energy by ca. 0.7 eV, combined with the identification of two chemical states of

Ni, suggests a possibility of Ni-Nb metal bonding. Both Ar⁺ monomer ion beam and Ar⁺ gas cluster ion beam (GCIB) have been used of XPS depth profiling. The former proved susceptible of inducing artificial chemical reduction of Ni oxides and Nb oxides, whereas the latter appeared to be reliable against such ion sputtering artefacts. The XPS analysis using GCIB source revealed the majority of Nb species in the coatings were pentoxide (Nb₂O₅) bonded with Ni, whilst the remaining, which accounts only for a small portion though, may be Nb metal. This signifies that reduction routes of Nb were complex and did not proceed completely. The deposition kinetics of the Ni-Nb system were studied using an electrochemical quartz crystal microbalance (EQCM). An ever-increasing rate of deposition was observed for galvanostatic deposition trials using a cathodic current density of 100 mA/cm². Finally a Ni-Nb co-deposition mechanism has been put forward, where at least three parallel electrochemical reduction routes have been surmised: 1) Reduction of Ni glycoxide ions into Ni metal; 2) Co-deposition of Ni-Nb-O-based nano-clusters from heteronuclear Ni-Nb-based glycoxide complexes; and 3) hydrogen evolution as a cathodic side reaction.

7.6 References

- [7.1] R. Winand, in *Modern Electroplating*, 5th ed., M. Schlesinger and M. Paunovic, Editors, p. 285, John Wiley & Sons, Hoboken (2010).
- [7.2] P. J. Goodhew, J. Humphreys and R. Beanland, in *Electron Microscopy and Analysis*, 3rd ed., p. 82, CRC Press (2000).
- [7.3] A. P. Grosvenor, M. C. Biesinger, R. St.C. Smart and N. S. McIntyre, *Surf. Sci.*, **600**, 1771 (2006).
- [7.4] N. Özer, D. G. Chen and C. M. Lampert, *Thin Solid Films*, **277**, 162 (1996).
- [7.5] M. Z. Atashbar, H. T. Sun, B. Gong, W. Wlodarski and R. Lamb, *Thin Solid Films*, **326**, 238 (1998).
- [7.6] K. Sugiyama, G. Anan, T. Shimada, T. Ohkoshi and, T. Ushikubo, *Surf.*

Coat. Technol., **112**, 76 (1999).

[7.7] K. Kowalski, A. Bernasik, W. Singer, X. Singer and J. Camra,. In *Proc. of the 11th Workshop on RF Superconductivity*, Travemünde, Germany, 610 (2003).

[7.8] D. L. Cocke, R. Campbell, K. Balke, M. Owens and R. B. Wright, *Appl. Surf. Sci.*, **40**, 227 (1989).

[7.9] T. Choudhury, S. O. Saied, J. L. Sullivan and A. M. Abbot, *J. Phys. D: Appl. Phys.*, **22**, 1185 (1989).

[7.10] A. J. Barlow, J. F. Portoles and P. J. Cumpson, *J. App. Phys.*, **116**, 054908 (2014).

[7.11] M. C. Biesinger, B. P. Payne, L. W. M. Lau, A. Gerson and R. St.C. Smart, *Sur. Interface Anal.*, **41**, 324 (2009).

[7.12] R. Weil and K. Sheppard, *Mater. Charact.*, **28**, 103 (1992).

Chapter 8

Diffusion Barrier Characterisations of Ni-NbO_x For Liquid In-Sn Solders

This chapter presents the results acquired from the diffusion barrier performance assessment of the Ni-NbO_x electrodeposited specimens, which include the measurements of the thin film electrical conductivity and solderability, as well as the solder diffusion tests. STEM microstructural characterisations of the reacted diffusion barrier samples are also reported.

8.1 Electrical Conductivity Measurements of Ni-NbO_x Electrodeposits

The introduction of Nb oxide compounds into the Ni metal finish may raise concerns over the possible degradation of the electrical conduction property. To explore this issue, the sheet resistance of pure Ni and Ni-Nb plated thin film specimens was assessed and plotted in **Fig. 8.1**. A 7 μm thick pure Ni coating was electrodeposited from Bath 2 at a cathodic current density of 12 mA/cm². The XPS compositional analysis has indicated that the Nb species was not co-deposited at this current density. The pure Ni specimen exhibited an approximately 0.5 mΩ increase in the sheet resistance, as compared with that of the bare copper substrate (24.5 mΩ). The Ni-NbO_x deposited samples with Nb contents ranging from 0.6 to 6.0 at.% represented increases of up to 9.2% (2.3 mΩ) in the sheet resistance, compared with the pure Ni counterpart. Such magnitudes of reduction in the electrical conductivity can be tolerated in terms of solder diffusion barrier application as electrical conduction performance is largely not compromised. The STEM compositional analysis reported in Chapter 7 (**Fig. 7.3**) suggests that the NbO_x compounds were fairly uniformly

distributed in the Ni matrix. Therefore, the electrical conductivity of the composite coatings is likely to be furnished by the Ni component, even though the universal existence of NbO_x clusters somewhat decreases the electrical conductivity.

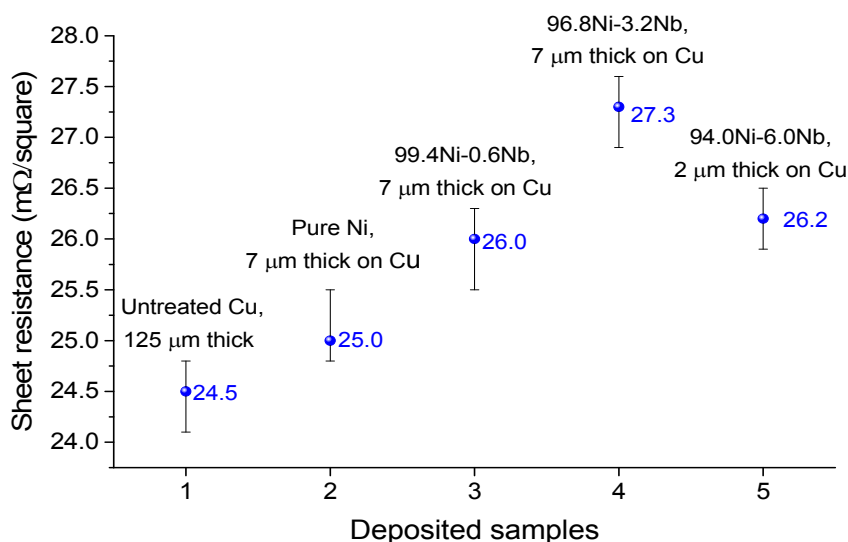


Figure 8.1 Graph presenting the average sheet resistance of untreated Cu sheet and Ni-based, deposited specimens measured using the four point probe method

8.2 Solderability Assessment

Another issue arising from the co-deposition of NbO_x clusters has been its impact on solderability. Nickel itself is a poorly solderable metal [8.1], the wettability of which with In-Sn solders employed in this study could be further even exacerbated by the universal presence of NbO_x compounds. To examine this, the contact angle, where the liquid solder/air interface meets the substrate surface, was measured, to provide an indication on the effect of substrate materials on the In-Sn solder wettability. Due to the generally poor solderability of Ni-based metal finishes, the eutectic 52In-48Sn solder paste (Indalloy 1E, Indium Corporation, USA) was applied together with an activation flux (NC-SMQ80, Indium Corporation, USA) to aid wetting. **Table 8.1** depicts the photographs of a range of Ni-NbO_x electrodeposited samples after soldering with eutectic In-Sn solders. It was observed that samples with Nb contents between 4.2 and 7.0 at.% generally demonstrated relatively large contact

angles ($> 75^\circ$), indicative of poor solderability even in the presence of a Ni-compatible flux. Contact angle values increased from ca. 78 to 115° , signifying diminishing solder wettability. This can be attributed to the increased Nb oxide contents being unsolderable [8.2]. Attempts have been made to sputter an ultrathin layer of gold on the Ni-Nb electrodeposit surface prior to soldering to promote solder wetting; however, the Au layer was quickly dissolved into the molten solder during the subsequent liquid solder diffusion test, rendering the induced wetting ineffective.

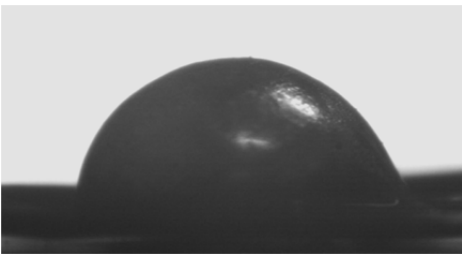
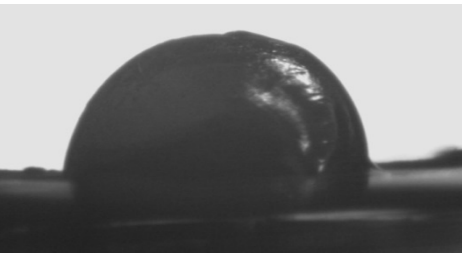
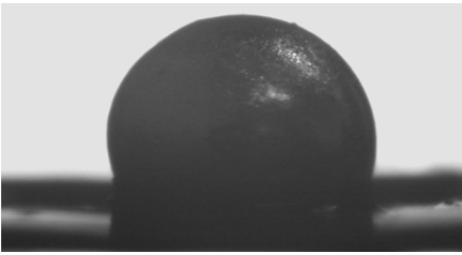
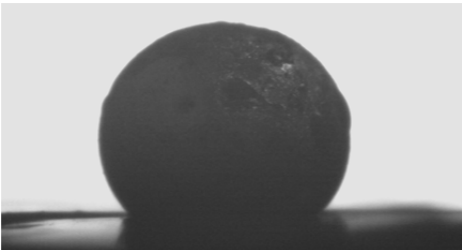
Samples	Images	Contact Angle
95.8Ni-4.2Nb		$78 (\pm 1.5)^\circ$
94.4Ni-5.6Nb		$81 (\pm 3.0)^\circ$
93.3Ni-6.7Nb		$109 (\pm 1.0)^\circ$
93.0Ni-7.0Nb		$115 (\pm 2.0)^\circ$

Table 8.1 A summary of contact angle measurements of soldered Ni-Nb electrodeposited specimens

8.3 Liquid Solder Diffusion Test

Ni-NbO_x electrodeposited specimens with varied Nb contents of up to 6.0 at.% were employed for the liquid solder diffusion test with eutectic 52In-48Sn solder at 200°C for periods of up to 14 days. Because of the trade-off between large coating thickness and high Nb content, it becomes unrealistic to compare samples with different Nb contents at a similar and sufficiently thick deposit thickness. Therefore, two groups of coatings with thicknesses of 7 and 2 μm were examined, the results of which are presented in **Table 8.2**. The failure of the diffusion barrier layer was defined as when the solder *begins* to penetrate through the barrier layer into the copper substrate. It appears that the coating thickness had the most significant influence over the barrier efficacy of the Ni-based coatings, as both the 2 μm thick pure Ni and 94.0Ni-6.0NbO_x metallisations failed within 3 hours. However, the 7 μm thick pure Ni showed a prolonged lifetime up to 48 hours and the similarly thick Ni-NbO_x metallisations survived for even longer times (up to 192 hours). With increased Nb content from 0 through 0.6 to 3.2 at.%, the lifetime of the barrier metallisations was extended from 48 through 72 to 192 hours. This suggests that the co-deposited Nb content played a significant role in prolonging the barrier lifetime and such an improvement increased with increasing Nb content in the coatings. The reason that the barrier layer with the highest Nb loading (94.0Ni-6.0NbO_x) failed within 3 hours, is largely ascribed to the low thickness, as well as to the cracks penetrating the deposit thickness arising from interaction with the liquid solder. The cracking of the high Nb content barrier layers will be discussed on **Page 143**.

Coating Thickness	Coating Composition (metal atomic percentage)	Lifetime
2 μm	Pure Ni	< 3 hrs
	94.0Ni-6.0Nb	< 3 hrs
7 μm	Pure Ni	< 48 hrs
	99.4Ni-0.6Nb	< 72 hrs
	96.8Ni-3.2Nb	< 192 hrs

Table 8.2 Summary of the barrier lifetimes of pure Ni and Ni-NbO_x layers in contact with molten 52In-48Sn solder at 200°C

Figure 8.2 presents representative interfacial microstructures and the IMCs formed between the 52In-48Sn solder and the Ni-based barrier metallisations after high temperature ageing at 200°C. Two types of IMCs were found to develop concurrently, those growing at the solder side into the molten solder, as well as those evolving at the Ni-based barrier side. In the In-Sn solders, micron-sized, dark-coloured and polygonal features were universally distributed, which were silicon carbide debris trapped during grinding due to the soft nature of the Sn-In solder. For the 7 μm thick, pure Ni and 99.4Ni-0.6NbO_x (**Figs. 8.2 (a) & (b)**), the IMCs developed at the solder side were generally well-faceted, some of which had spalled and migrated from the interface between the barrier layer and solder into the bulk of the liquid solder after 72 hours at 200°C. EDX point analyses suggest that these IMCs contained nickel, indium and tin, slightly fluctuating about an approximate atomic composition at Sn₂Ni₁In₁. The fluctuation is attributable to the excessive mutual solubility between indium and tin [8.3]. Little niobium content was observed within these IMC structures, signifying that Nb played a passive role in their formation. For the 96.8Ni-3.2NbO_x, the Ni-In-Sn IMC structures growing into the solder were still attached to the solder/IMC interface yielding a relatively continuous and compact layer, without having spalled into the solder

even after 216 hours when the barrier metallisation had been completely consumed (**Fig. 8.2 (c)**). A diffusion barrier metallisation with a continuous IMC layer on top is thought to be more effective in counteracting the inter-diffusion of those IMC forming species such as Ni, In and Sn, as compared to one with IMCs continually growing and spalling away into the liquid solder [8.4]. Nevertheless, the 94.0Ni-6.0NbO_x layer (**Fig. 8.2 (d)**) did not demonstrate similar IMC characteristics and presented discrete and spalled Ni-In-Sn IMCs with a faceted geometry. This may be ascribed to its insufficient deposit thickness (i.e. 2 μm).

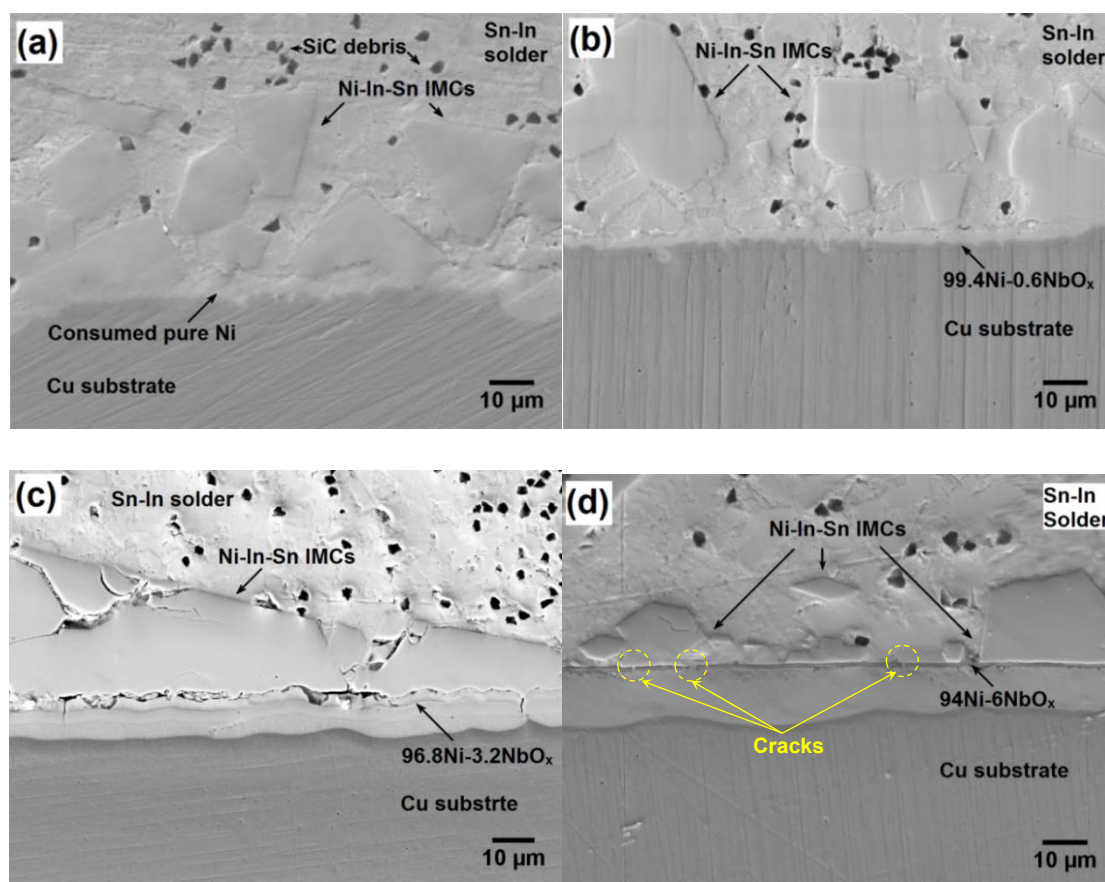


Figure 8.2 SEM images showing the representative interfacial microstructure of pure Ni and Ni-NbO_x deposited samples after reaction with molten 52In-48Sn: a) 7 μm thick, pure Ni for 72 hours and b) 7 μm thick, 99.4Ni-0.6Nb for 72 hours, c) 7 μm thick, 96.8Ni-3.2Nb for 216 hours and d) 2 μm thick, 94.0Ni-6.0Nb for 9 hours

It is noteworthy that the 94.0Ni-6.0NbO_x (with the highest Nb content) exhibited cracking, as is revealed from the cross-sectional (**Fig. 8.2 (d)**) and top view (**Fig. 8.3**). **Figure 8.3** depicts the exposed morphology of a 2 μm thick, 94.0Ni-6.0NbO_x deposit that had reacted with liquid 52In-48Sn solder at 200 °C for 5 hours after chemical dissolving the solder utilising an etching solution containing 35 g/L o-nitrophenol and 50 g/L NaOH. A network of cracks was evident penetrating through the barrier layer thickness, which seemed to furnish a straightforward pathway for liquid solder ingress into the underlying copper substrate. This is thought to give rise to localised Cu-In-Sn IMC formation (in an atomic composition of 56Cu-20In-24Sn, corresponding to the Cu₆(In, Sn)₅) through the cracks, which rendered the barrier ineffective and caused premature failure. It should be noted that, the unsoldered region of the 94.0Ni-6.0NbO_x sample did not exhibit any cracks. This implies that the cracking might have initiated upon interaction with the molten solder. The origin of the cracking in high NbO_x content samples is, therefore, presumably attributable to the high oxygen content present in the deposit instigating additional strain upon interaction with the molten solder.

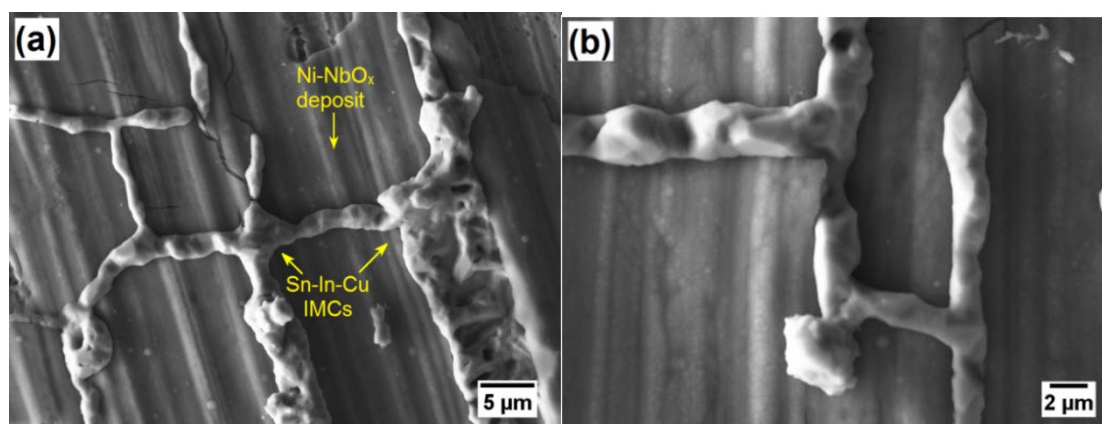


Figure 8.3 SEM images showing the representative surface morphology of a 2 μm thick 94.0Ni-6.0NbO_x deposited sample that reacted with molten Sn-In solder at 200°C for 5 hours after chemical stripping away the solder

It becomes evident that the additions of the NbO_x content up to 3.2 at.% into the Ni coating, combined with a layer thickness of at least 7 μm, could enhance the barrier efficacy. In order to understand the specific role of Nb as the barrier enhancer, EDX point analysis has been carried out across the interface on the soldered, Ni-NbO_x deposited samples at various NbO_x contents. As illustrated in **Fig. 8.4**, five zones were identified across the interface of the 99.4Ni-0.6NbO_x specimen after ageing at 200°C for 72 hrs, which are: I) copper substrate, II) un-consumed Ni-NbO_x coating, III) consumed barrier layer with elevated Nb content (approximately 1.0 at.% Nb), IV) consumed barrier layer depleted in Nb (up to 0.2 at.% Nb) and V) IMCs developing at the solder side (assuming that the IV/V interface indicates the position of the original interface between the barrier layer and solder). From the consumed barrier region (Zones III & IV), the enrichment of Nb was seen in the reaction front between molten solder and the barrier layer, which implies that the Nb species had migrated with Sn and In (i.e. solid state diffusion) during the Sn-Ni-In IMC formation. It is thought that, the enhancing effect of Nb on the barrier behaviour of the Ni-based layer arises, at least partially, from such a re-distribution and hence concentration of Nb at the reaction front. Also in **Fig. 8.4 (b)**, the reacted region (including Zones III, IV & V) presented fairly constant compositions, at around 46Sn-29In-25Ni for Zones III & IV and at around 47Sn-31In-22Ni for Zone V. The compositional variations are likely to be due to mutual solubility between In and Sn.

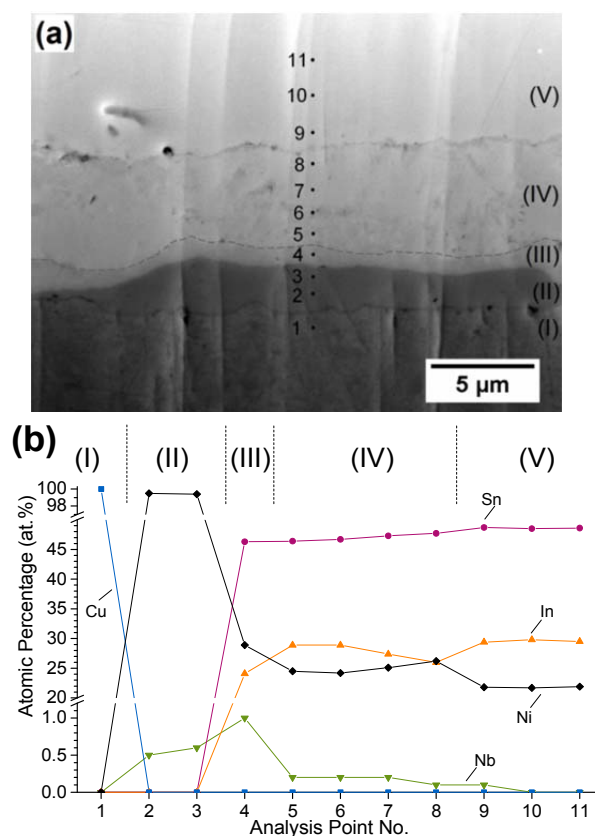


Figure 8.4 a) SEM image showing the representative interfacial microstructure of a 99.4Ni-0.6Nb deposited samples after reaction with molten Sn-In solder at 200°C for 72 hours and b) a plot showing the EDX point analysis results indicated in a), (I) to (V) represent zones observed across the interfaces

With the codeposited Nb content elevated to 3.2 at.%, the 7 μm thick Ni-NbO_x deposited sample saw an extension of the barrier lifetime from 72 to 192 hrs. **Figure 8.5** depicts the interfacial microstructure of a 7 μm thick, 96.8Ni-3.2NbO_x sample after reaction with molten Sn-In solder at 200°C for 192 hrs. Again, five zones were identified across the interfaces, which are: I) un-consumed copper substrate, II) un-consumed Ni-NbO_x metallisation, III) consumed barrier layer with slightly elevated Nb content (ca. 4.5 at.% Nb), IV) consumed barrier layer with elevated Nb content (ca. 10 at.% Nb) and V) IMCs forming at the solder side. Once more, the enrichment of Nb in the consumed barrier coating (i.e. Zones III & IV) was evident, which was, nonetheless, not necessarily accompanied by the presence of a Nb depleted region, as observed from the 99.4Ni-0.6NbO_x sample. This may suggest there is thickness reduction of the diffusion metallisation, as Ni, the major component

of the barrier layer, diffuses into the solder to form IMCs. This assumption is corroborated by the observations from the 94.0Ni-6.0NbO_x deposit sample presented later. Although the Nb content in the reaction front (i.e. Zone III) is elevated (~4.5 at.%) when compared with that in the remaining barrier layer (~3.2 at.%), it was observed that Zone IV contained the highest Nb content (~10 at.%) of all the zones. In Zone IV, the atomic percentage of indium was also elevated (~45 at.%), as compared to that of the adjacent zones (down to ~22 at.% In in both Zones III & V). The atomic ratio of In to Nb was ca. 45:10 in this region. Such concurrent enrichments of niobium and indium in Zone IV were also reflected in the X-ray maps of the corresponding regions, as illustrated in **Fig. 8.6**. These results imply that indium had a relatively high affinity to form IMC compounds with the Nb species present in the barrier layer than that of Sn. Nevertheless, the Nb atoms did not seem to migrate significantly with the reaction front, which eventually resulted in the Zone III with Nb contents intermediate between that of Zone II and Zone IV.

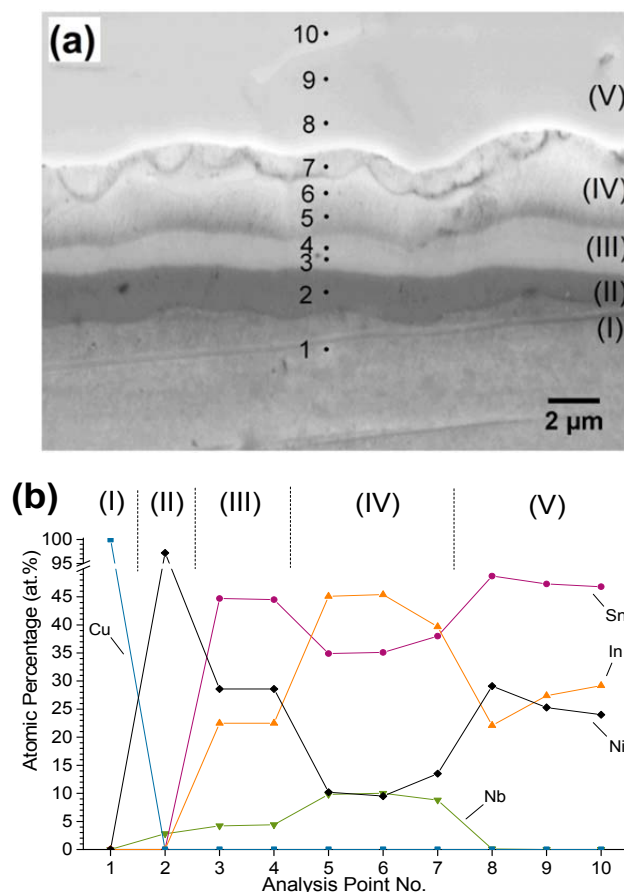


Figure 8.5 a) SEM image showing the interfacial microstructure of a 96.8Ni-3.2Nb deposited samples after reaction with molten Sn-In solder at 200°C for 192 hours and b) a plot showing the EDX point analysis results indicated in a), (I) to (V) represent zones observed across the interfaces

From previous chapters it has been confirmed that the composition of the as-deposited Ni-NbO_x metallisation was almost constant across the thickness, albeit with slight compositional fluctuations. Therefore, the present multi-layer interfacial structure is likely to be an intermediate stage during the redistribution of the Nb species, as the diffusion rate of the O-bonded and presumably In-associated Nb may be slower than that of Sn. Besides, the IMCs formed at the solder side (Zone V) exhibited a composition comparable to that of the Zone V from the 99.4Ni-0.6NbO_x sample, which is also similar to that observed from the interface of a pure Ni layer. This suggests that Nb does not necessarily alter the composition of the Sn-Ni-In IMCs growing at the solder side. Nb is more likely to counteract the consumption of the Ni-based

layer, presumably by slowing down the inter-diffusion of Sn, In and Ni atoms across the interfaces.

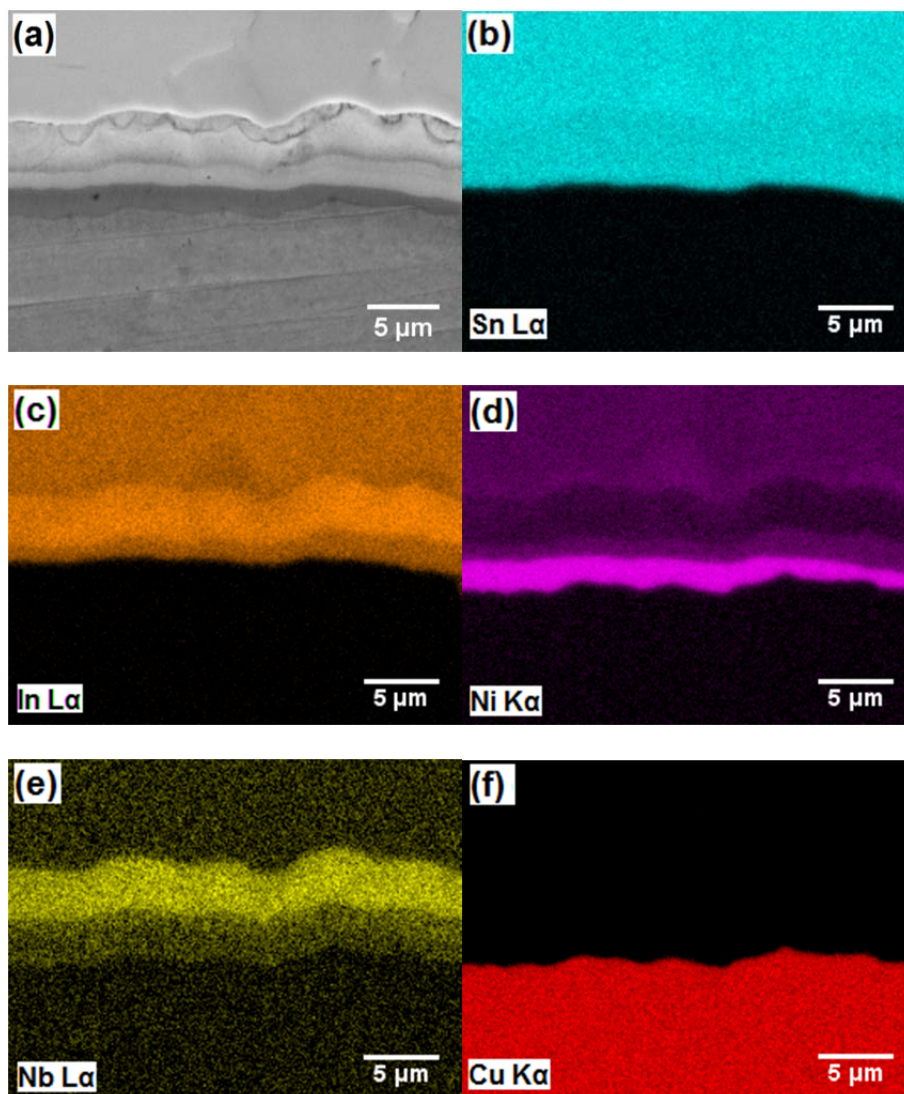


Figure 8.6 a) SEM image showing the interfacial microstructure of a 96.8Ni-3.2Nb deposited samples after reaction with molten Sn-In solder at 200°C for 192 hours and the corresponding X-ray maps showing b) Sn L α , c) In L α , d) Ni K α , e), Nb L α , and f) Cu K α

With the codeposited Nb content further increased to 6.0 at.%, the Ni-NbO_x layer suffered from a limited thickness (~2 μm) and hence did not display any enhanced barrier property (i.e. failed within 3 hours at 200°C). **Figure 8.7** depicts the interfacial microstructure of a 2 μm thick, 94.0Ni-6.0NbO_x deposited sample after reaction with molten eutectic 52In-48Sn solder at

200°C for 9 hrs, when the Ni-based barrier had been completely penetrated. Three zones can be identified across the interface, which are: I) reacted copper substrate, II) consumed Ni-NbO_x layer and III) IMCs growing at the solder side. The IMCs in both Zones I and III contained Cu as the effect of the barrier layer had completely diminished, which can be attributed to the aforementioned cracking of the barrier upon interaction with the liquid solder. However, it is noteworthy that, the thickness of the barrier layer (Zone II) saw an appreciable reduction from 2 μm to ~700 nm after reaction with the molten In-Sn solder, which was accompanied by a rise of the Nb content from 6 to 11 at.%. This is because, following inter-diffusion the barrier layer no longer existed in its original form but rather as a reaction product, where the increased Nb content may simply result from the barrier layer being pushed ahead on the molten reaction front. In addition, the In content in Zone II was evidently elevated (45 at.%), as compared to that of the adjacent zones (up to 17 at.%), with the atomic ratio of In to Nb at ca. 45:11, which is comparable to that from the 96.8Ni-3.2NbO_x counterpart. This signifies that, the reaction of the Ni-NbO_x with molten Sn-In solder forms a layer enriched in Nb and In, with relatively fixed composition (atomic ratio of In to Nb of around 45:10). Such a layer is believed to provide enhanced barrier efficacy presumably by retarding the inter-diffusion of intermetallic forming species (Ni, Sn and In).

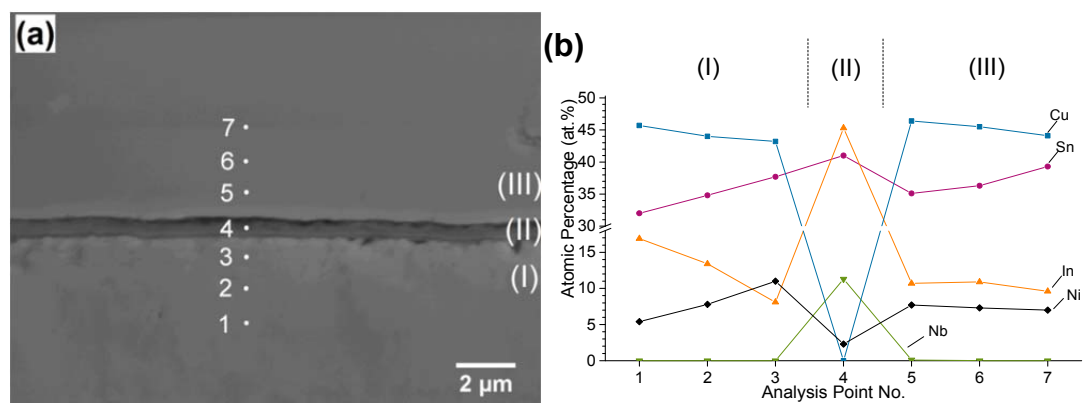


Figure 8.7 a) SEM image showing the interfacial microstructure of a 94.0Ni-6.0Nb deposited samples after reaction with molten Sn-In solder at 200°C for 9 hours and b) a plot showing the EDX point analysis results indicated in a), (I) to (III) represent zones observed across the interfaces

8.4 STEM Characterisations of Reacted, In-Sn/Ni-NbO_x Diffusion Couples

STEM microstructural, compositional and crystallographic characterisations of the reacted, In-Sn/Ni-NbO_x deposited samples were undertaken to acquire a high resolution insight into the role of NbO_x as the Ni barrier enhancer. A thin film TEM sample was prepared from 96.8Ni-3.2NbO_x deposited specimen after reaction with liquid 52In-48Sn solder at 200°C for 192 hours. The bright field image is presented in **Fig. 8.8**, together with a line scan EDX analysis across the interfaces. Five zones could be identified, which are consistent with the SEM cross-sectional observations. Despite slight compositional gradients, the atomic composition in each zone was largely constant, as presented in **Table 8.3**. The IMCs growing into the molten solder (i.e. Zone 1) contained approximately 22Ni-50Sn-28In in atomic percentage; little Nb content was detected in this region, indicating a passive role of Nb species in the formation of such type of IMCs. Such a composition also falls in the common range of the IMCs from Ni-based metallisations [8.3, 8.5] when reacting with eutectic 52In-48Sn solder at 200°C, which is recognised as binary Ni₂₈In₇₂ phase with excessive ternary Sn solubility, taking in the form of Ni₂₈(In_{0.3}, Sn_{0.7})₇₂. The bright field TEM image of Zone I is depicted in **Fig. 8.9**, which indicates micron-sized IMCs with various orientations. Some dislocations were evident

from Grain C in **Fig. 8.9 (b)**, which is not surprising as structural defects normally occur during IMC formation. The reacted Ni-NbO_x barrier layer contained two zones (Zones II & III) with distinct compositions. Zone II exhibited a rough atomic composition as 12Ni-28Sn-53In-7Nb, the Nb content of which was much higher than that in the original composite barrier layer (i.e. 3.2 at.% Nb). **Figure 8.10** presents the representative morphology of the Zone II, together with a typical selected area diffraction pattern (SADP) of the region. It can be seen that this reacted barrier region consisted of nanocrystalline, equiaxed grain features, without retaining the fibrous crystal morphology evident throughout the deposit in the original barrier sample.

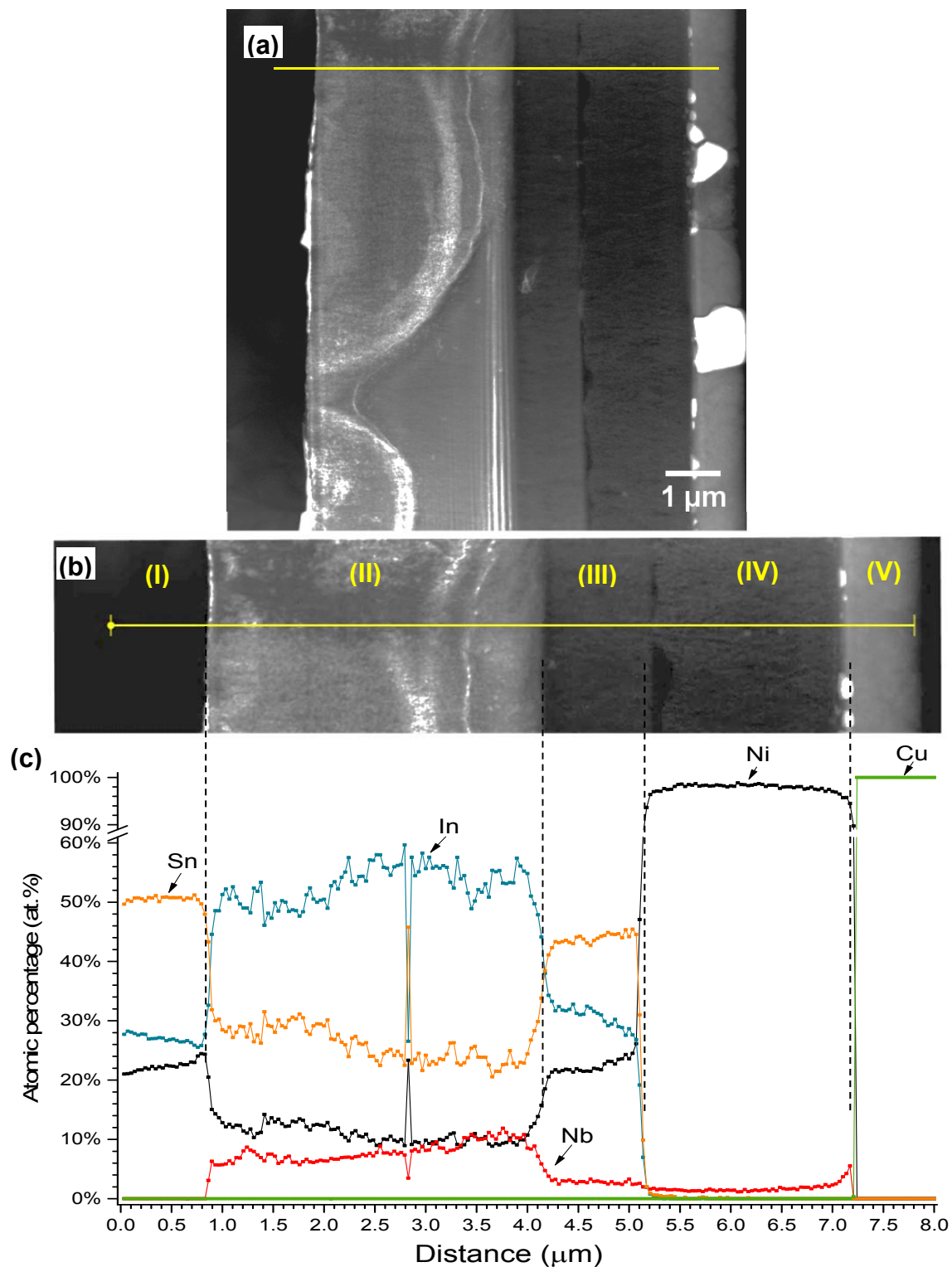


Figure 8.8 a) STEM bright field image showing the interfacial microstructure of a 96.8Ni-3.2Nb deposited sample after reaction with molten Sn-In solder at 200°C for 192 hours, b) a magnified image of a) showing the EDX line scan and c) a plot showing the EDX line scan analysis results indicated in b), (I) to (V) represent zones observed across the interfaces

Zone Number	Zone Name	Approximate atomic composition
(I)	IMCs growing into the solder	22Ni-50Sn-28In
(II)	IMCs forming at the barrier side with relatively high Nb contents	12Ni-28Sn-53In-7Nb
(III)	IMCs forming at the barrier side with relatively low Nb contents	22Ni-43Sn-30In-5Nb
(IV)	Unreacted barrier	97Ni-3Nb
(V)	Unreacted copper substrate	100Cu

Table 8.3 Atomic compositions of the five zones identified across the interfaces from 96.8Ni-3.2NbO_x deposited sample after reaction with liquid In-Sn solder at 200°C for 192 hours

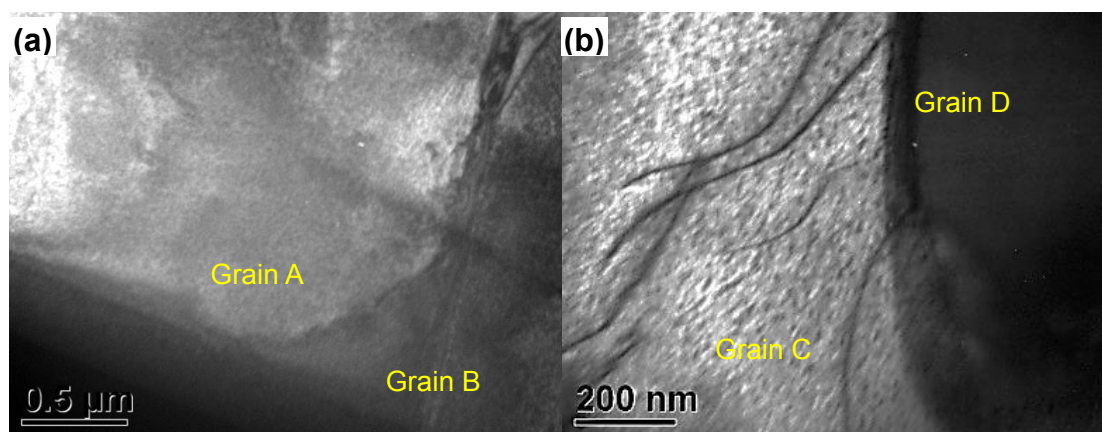


Figure 8.9 TEM bright field image of the IMCs growing into the solder from 96.8Ni-3.2NbO_x deposited sample after reaction with liquid In-Sn solder at 200°C for 192 hours

Wave-like bands, appearing lighter in the bright field image, can also be observed in **Fig. 8.10**, which may imply the ingress of solder into the Ni-based barrier layer. From the corresponding X-ray map for Nb (Nb L α), the Nb content outside the segment defined by the arc-like features appeared to be relatively high (up to 11 at.%) in the Zone II, which was ca. 4 at.% higher than that within the segment (7 at.%) in Zone II, ca. 6.5 at.% higher than that in

Zone III (4.5 at.%) and ca. 8 at.% higher than that in the unreacted barrier layer (Zone IV). Such variations in the Nb concentration are reflected in **Fig. 8.11 (b)**. These results imply that, Nb species tended to migrate with the reaction front during the liquid state solder reaction causing Nb enrichment; however, such a redistribution of Nb is significantly reduced when certain barrier layer thickness has been reacted.

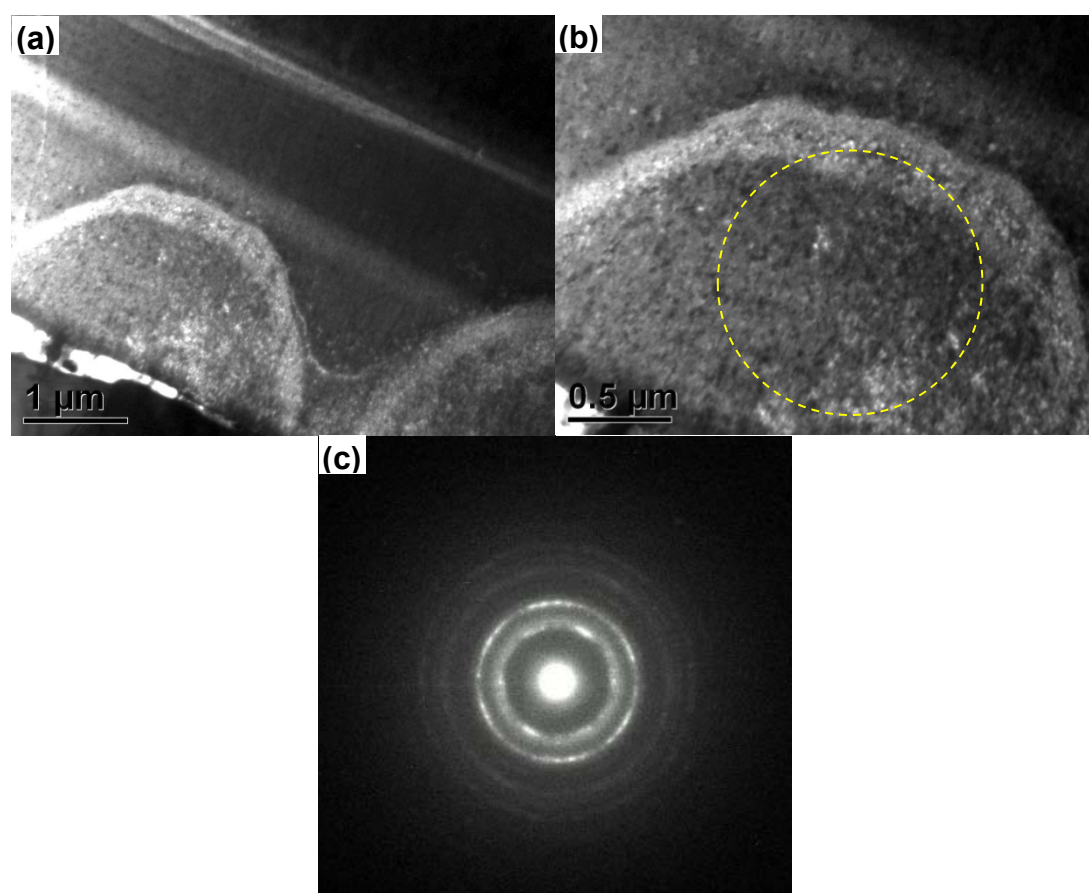


Figure 8.10 a-b) STEM bright field images of the consumed barrier layer (upper region, Zone II) from 96.8Ni-3.2NbO_x deposited sample after reaction with liquid In-Sn solder at 200°C for 192 hours and c) the selected area electron diffraction pattern taken from the circled area in b)

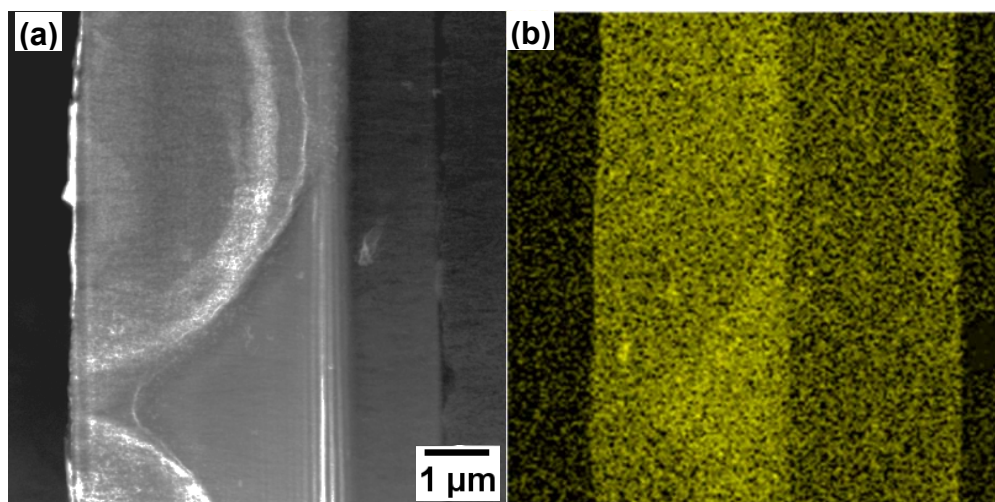


Figure 8.11 a) STEM bright field image of the barrier layer region from 96.8Ni-3.2NbO_x deposited sample after reaction with liquid In-Sn solder at 200°C for 192 hours and b) the corresponding elemental map of Nb L α

The SADP (**Fig. 8.10 (c)**) implies a nanocrystalline Ni₂₈In₇₂ phase with lattice distortion, with the first five strong rings indexed as (310), (330), (521), (611) and (721). However, simply assigning the composition only to Ni₂₈In₇₂-based structure may not fulfil stoichiometry at 12Ni-28Sn-53In-7Nb due to the insufficient Ni content. Therefore, it is reasonable to speculate that Zone II contained more than one compound. The additional indium and/or tin may be associated with the Nb compounds.

Figure 8.12 presents the morphology of the lower region (i.e. the reaction front, or Zone III) of the reacted barrier after reaction with In-Sn solder at 200°C for 192 hours, along with a representative SADP. The fibrous, nanocrystalline grain morphology was evident, which is in contrast to Zone II where the fibrous grain characteristic had been lost. Zone III exhibited a nanocrystalline Ni₂₈(In_{0.4}, Sn_{0.6})₇₂ structure with slight lattice distortion, which is akin to the IMCs at the solder side (Zone I), albeit at different compositions (Zone I: Ni₂₈(In_{0.3}, Sn_{0.7})₇₂).

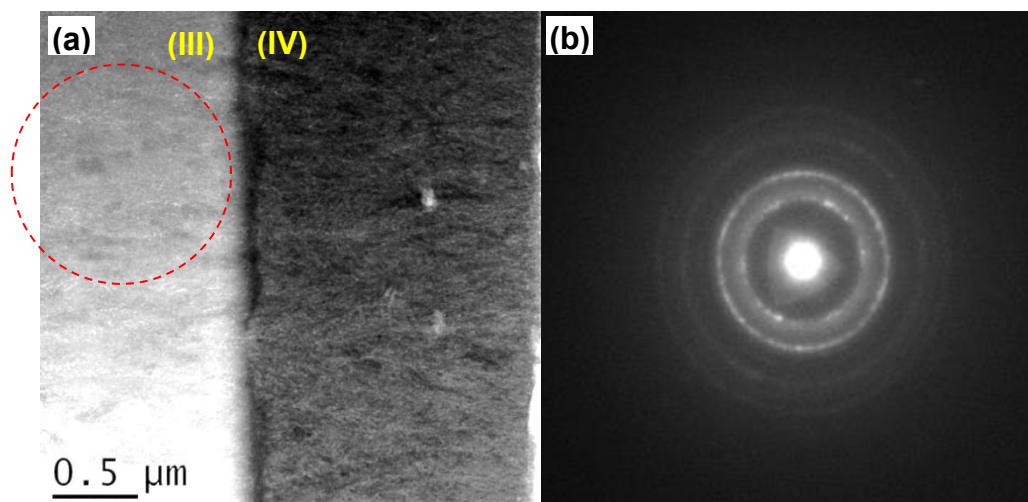


Figure 8.12 a) STEM bright field image of the consumed barrier layer (lower region, Zone III) from 96.8Ni-3.2NbO_x deposited sample after reaction with liquid In-Sn solder at 200°C for 192 hours and b) the selected area electron diffraction pattern taken from the circled area in a)

The crystallographic and compositional information regarding each reacted zone is tabulated in **Table 8.4**. A similar pure Ni sample [8.6] has been reported to exhibit similarly polycrystalline Ni₂₈(In, Sn)₇₂ IMCs growing into the liquid solder as well as at the barrier side, without necessarily demonstrating an interphase similar to the Zone II observed in the present Ni-NbO_x sample. During solder reaction with the Ni-NbO_x layer (**Figure 8.13**), the interdiffusion of In, Sn and Ni proceeds across the solder/barrier interface. Ni₂₈(In,Sn)₇₂ forms at the solder side whilst the barrier layer is reacted to form IMCs with similar crystallographic structure but at different compositions. The barrier layer shrinks as the IMCs progressively develop, accumulating the less reactive, NbO_x-based clusters in the consumed barrier layer. These NbO_x-based nanoclusters also seemed to sequester indium as the latter element content was stoichiometrically too high to form any known Ni₂₈In₇₂ compound.

It is thought that the presence of this Nb-enriched interphase (Blue-coloured region in **Figure 8.13**) tends to retard the consumption of the Ni-Nb-based barrier metallisation, by slowing down the interdiffusion between those IMC forming species such as Ni, In and Sn, whereby the barrier lifetime is extended compared to that of the pure Ni counterpart.

Zone Name	Atomic Composition	Crystal Structure
(I) IMCs growing into the solder	22Ni-50Sn-28In	Polycrystalline Ni ₂₈ (In _{0.3} , Sn _{0.7}) ₇₂
(II) IMCs forming at the barrier side – upper zone	12Ni-28Sn-53In-7Nb	Nanocrystalline, Ni ₂₈ (In _x , Sn _(1-x)) ₇₂ with NbO _x -based nanoclusters universally distributed
(III) IMCs forming at the barrier side – lower zone (reaction front)	22Ni-43Sn-30In-5Nb	Nanocrystalline Ni ₂₈ (In _{0.4} , Sn _{0.6}) ₇₂

Table 8.4 Atomic compositions and crystal structure of the three reacted zones identified across the interfaces from 96.8Ni-3.2NbO_x deposited sample after reaction with liquid In-Sn solder at 200°C for 192 hours

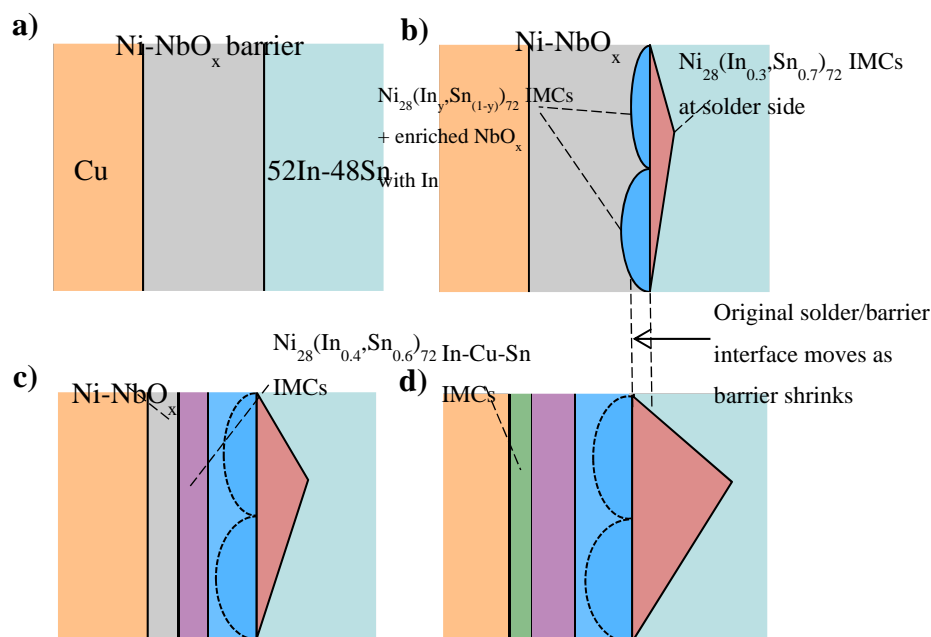


Figure 8.13 Schematic diagrams of the microstructure evolution of Ni-NbO_x barrier layer after interaction with liquid 52In-48Sn solder at 200°C

8.5 Summary

In this chapter, the electrical conductivity, solderability and barrier efficacy of the Ni-NbO_x electrodeposited samples have been evaluated. The introduction of NbO_x species into the Ni metallisation at up to 6 at.% slightly reduces the electrical conductivity and significantly degrades the solderability (even in the presence of a Ni-compatible solder flux). It becomes evident that the additions of the NbO_x content up to 3.2 at.% into the Ni coating, combined with a layer thickness of at least 7 μm, could enhance the barrier efficacy from 2 days to 8 days at 200°C. STEM microstructural, compositional and crystallographic analysis has been conducted on a 96.8Ni-3.2NbO_x sample after reaction with eutectic 52In-48Sn solder at 200°C for 192 hours to understand the role of NbO_x as the Ni barrier enhancer. It was found that the IMCs forming at the solder side presented a micron-sized grain structure of Ni₂₈(In_{0.3}, Sn_{0.7})₇₂ and the consumed barrier layer consisted of two zones: nanocrystalline Sn-rich, Ni₂₈(In_{0.4}, Sn_{0.6})₇₂ at the reaction front and nanocrystalline, In-rich and

Nb-enriched Ni₂₈(In, Sn)₇₂ with additional In content associated with Nb species. The latter is believed to act as a barrier interphase, which slows down the consumption of the Ni-based layer by retarding the interdiffusion of those IMC forming species.

8.6 References

- [8.1] Metals Handbook, ed., ASM Handbook Committee (American Society for Metals, Metals Park, 1983), 9th ed., Vol. 6, p. 1085.
- [8.2] P. T. Vianco, *Circuit World*, **25** (1), 6 (1998).
- [8.3] C. Y. Huang and S. W. Chen, *J. Electron. Mater.*, **31**, 152 (2002).
- [8.4] J. F. Li, S. H. Mannan and M. P. Clode, *Scripta Materialia*, **54** (10), 1773 (2006).
- [8.5] S. k. Seo, M. G. Cho, H. M. Lee and W. K. Choi, *J. Electron. Mater.*, **35**, 11 (2006).
- [8.6] C. J. Chen and K. L. Lin, *IEEE Trans. Comp. Pack. Manuf. Technol.*, **20B**, 211 (1997).

Chapter 9

Conclusions and Future Work

9.1 Conclusions

The experimental investigations conducted in the present study have produced Ni-NbO_x metal coatings using an electrodeposition approach, which has proved promising as a novel diffusion barrier for liquid In-Sn/Cu solder interconnections. The following conclusions can be drawn from these studies:

1. The electrochemistry of Nb in common Type III deep eutectic solvents (e.g. reline and ethaline) and Type IV off-eutectic solvents such as (urea:NbCl₅ mixture and ethylene glycol:NbCl₅ mixture) has been investigated, with respect to the solubility and electrochemical behaviour of the metal precursor, electrolyte workability and electrode stability. Type III DESs such as reline and ethaline gave relatively low solubility of NbCl₅ and could not allow significant complete reduction of Nb species due to the excessive cathodic breakdown. Adherent Nb reduction products were seldom produced from these electrolytes, no matter whether NbCl₅ or anodically dissolved Nb was used as the metal precursor. Type IV off-eutectic solvents such as NbCl₅:ethelene glycol mixtures permitted high solubility of NbCl₅ and yielded inadherent Nb oxide reduction products upon electrolysis. The high temperatures (above 100°C) experienced in the use of these solutions require a paradigm change with respect to electroplating cell design, where the conventional inert anode like platinised Ti and untreated graphite electrode and reference electrode like Ag wire become dissolved, releasing foreign metal ions into electrolytes and thereby poisoning the reduction process. Nb metal has proved reliable as an anode and reference electrodes to prevent contamination.

2. A novel electrodeposition process for the preparation of Ni-Nb thin films has been developed, from a non-aqueous Type IV off-eutectic solvent based on propylene glycol. The effect of electrolyte constituents, such as the type of glycol, metal ion concentration and NaBH_4 concentration, as well as the effect of cathodic current density and electrodeposition time, on the surface morphology, composition and thickness of the deposits, has been investigated. Based on the galvanostatic trials, an effective formulation and appropriate deposition parameters have been established. Macroscopic uniformity of the deposits can be achieved by introducing a reducing agent, NaBH_4 , to reduce the bath acidity and thereby suppressing the competing hydrogen evolution. Microscopic uniformity of the Ni-Nb deposits, however, requires the use of relatively low metal ion concentrations in the electrolyte, which otherwise is susceptible to produce localised and spongy deposition. A threshold deposit thickness generally exists for the Ni-Nb electrodeposits, which is presumably dependent on the co-deposited Nb content. A trade-off is also evident between large coating thickness and high Nb content for the present Ni-Nb electrodeposition system. Large deposit thickness can be pursued when high NaBH_4 content baths and small current densities are employed; whilst high Nb contents is attainable by minimising (but not eliminating) NaBH_4 concentrations in the electrolyte and maintaining relatively large current densities (yet not too high to induce spongy deposition). Based on these results, a deposition model analogous to the induced co-deposition has been proposed, wherein Nb co-deposition is allowed by the possible existence of polynuclear, Ni-Nb-based metal complexes in the electrolyte.

3. STEM characterisations have disclosed the ultra-fine microstructural details of the nanocrystalline Ni-NbO_x electrodeposits, where an unusually uniform yet repeatable dispersion of NbO_x clusters was observed within the Ni matrix. A reduction in the Ni content was recognised with increasing distance to the substrate-deposit interface, together with slight compositional fluctuations.

Electron diffraction data suggested the absence of Nb species within the Ni lattices, indicating that no bulk alloy was formed. XPS data reported an unusual chemical shift of Nb species towards lower binding energy by ca. 0.7 eV, combined with the identification of two chemical states of Ni, suggests a possibility of Ni-Nb metal bonding. Both Ar⁺ monomer ion beam and Ar⁺ gas cluster ion beam (GCIB) have been used for XPS depth profiling. The former proved susceptible to inducing artificial chemical reduction of Ni oxides and Nb oxides, whereas the latter appeared to be reliable against such ion sputtering artefacts. The XPS analysis using GCIB source revealed the majority of Nb species in the coatings were pentoxide (Nb₂O₅) bonded with Ni, whilst the remaining, which accounts only for a small portion though, may be Nb metal. This signifies that reduction routes of Nb were complex and did not proceed completely. The deposition kinetics of the Ni-Nb system were studied using an electrochemical quartz crystal microbalance (EQCM). An ever-increasing rate of deposition was observed for galvanostatic deposition trials using a cathodic current density of 100 mA/cm². Finally a Ni-Nb co-deposition mechanism has been put forward, where at least three parallel electrochemical reduction routes have been surmised: 1) Reduction of Ni glycooxide ions into Ni metal; 2) Co-deposition of Ni-Nb-O-based nano-clusters from heteronuclear Ni-Nb-based glycooxide complexes; and 3) hydrogen evolution as a cathodic side reaction.

4. The electrical conductivity, solderability and barrier efficacy of the Ni-NbO_x electrodeposited samples have been evaluated. The introduction of NbO_x species into the Ni metallisation at up to 6 at.% slightly reduces the electrical conductivity and significantly degrades the solderability (even in the presence of a Ni-compatible solder flux). It becomes evident that the additions of the NbO_x content up to 3.2 at.% into the Ni coating, combined with a layer thickness of at least 7 μm, could enhance the barrier efficacy from 2 days to 8 days at 200°C. STEM microstructural, compositional and crystallographic

analysis has been conducted on a 96.8Ni-3.2NbO_x sample after reaction with eutectic 52In-48Sn solder at 200°C for 192 hours to understand the role of NbO_x as the Ni barrier enhancer. It was found that the IMCs forming at the solder side presented a micron-sized grain structure of Ni₂₈(In_{0.3}, Sn_{0.7})₇₂ and the consumed barrier layer consisted of two zones: nanocrystalline Sn-rich, Ni₂₈(In_{0.4}, Sn_{0.6})₇₂ at the reaction front and nanocrystalline, In-rich and Nb-enriched Ni₂₈(In, Sn)₇₂ with additional In content associated with Nb species. The latter is believed to act as a barrier interphase, which slows down the consumption of the Ni-based layer by retarding the interdiffusion of those IMC forming species.

9.2 Recommendations for Future Work

1. Bath acidity of the electrolytes has been found to have a profound influence over co-deposition of Nb species. Low acidity of the electrolyte greatly reduces the Nb content in the electrodeposits, whereas too acidic the electrolyte is susceptible to excessive hydrogen evolution, greatly decreasing the cathodic current efficiency. The present study has shown that NaBH₄ is effective as a bath acidity modifier. Future work can improve its efficacy or examine the possibility of other hydrogen reducing agents like hydrated sodium hypophosphite (NaPO₂H₂·H₂O);

2. It has been recognised that the Ni-NbO_x electrodeposits produced in the present study have a limiting thickness, beyond which Ni-Nb co-deposition becomes in adherent. This is presumably due to steady elevation of co-deposited Nb sub-oxide content during the galvanostatic deposition, leading to ever-decreased deposit adhesion. Future investigations can focus on elevating the maximum coating thickness, without heavily compromising the co-deposited Nb content. Such improvement may be achieved by reducing the mean oxidation number of Nb species in the coatings (i.e. to further

electrochemically reduce the Nb species in the electrolytes). This would also be advantageous for increasing the solderability of the resulting coatings and for enhancing their diffusion barrier efficacy;

3. It would be favourable to produce the Ni-Nb-based electrodeposits at relatively low current densities (or deposition potentials), which could prolong the electrolyte lifetime and also yield electrodeposited microstructure with much larger mean grain size. Large-grained structures have a low density of grain boundary, which is preferable against grain boundary diffusion during solder reaction;

4. It would be of both academic and technical interests to increase the co-deposited Nb content in the coatings, which ultimately could produce pure Nb metal coatings with any Ni or O to be co-deposited. To pursue this, room temperature ionic liquids like BMP TFSA could be investigated in conjunction with the use of inert atmosphere;

5. The integration possibility of the present deposition processes with other electronics microfabrication steps like photoresist patterning should be investigated.

Appendix I – List of Publications

- 1) J. Wang, M. A. Ashworth, and G. D. Wilcox, *Proc. 6th Int. Symp. On Tin Whiskers*, Loughborough, UK, Nov. 2012, CALCE, University of Maryland and Loughborough University (Oral presentation).
- 2) J. Wang, M. A. Ashworth, and G. D. Wilcox, '**An Investigation into the Role of Lead as a Suppressant for Tin Whisker Growth in Electronics**', *IEEE Trans. Comp. Pack. Manuf. Technol.*, **4**(4), p. 727 (2014).
- 3) J. Wang, G. D. Wilcox, R. J. Mortimer, C. Liu, and M. A. Ashworth, '**Electrodeposition and Characterisation of Nanocrystalline Ni-NbO_x Composite Coatings from Glycol-based Electrolytes for High Temperature Electronics Packaging**', *J. Electrochem. Soc.*, **161**(9), p. D395 (2014).
- 4) J. Wang, G. D. Wilcox, R. J. Mortimer, C. Liu, and M. A. Ashworth, '**Electrodeposition and Characterisation of Novel Ni-NbO_x Coatings as a Diffusion Barrier for Liquid Solder Interconnects - Part II: Diffusion Barrier Performance**', in *Electronic Materials and Processing, The Electrochemical Society Proceedings Series, 226th ECS Meeting, Cancun, Mexico, Oct. 5th – 9th, 2014*. (paper & oral presentation)
- 5) J. Wang, G. D. Wilcox, R. J. Mortimer, C. Liu, and M. A. Ashworth, '**Diffusion Barrier Characteristics of Ni-NbO_x Composite Electrodeposits for Liquid In-Sn Solder Interconnects**', *J. Electrochem. Soc.*, **162**(4), p. D147 (2015).